INFORMATION TO USERS

This manuscript has been reproduced from the microfilm master. UMI films the text directly from the original or copy submitted. Thus, some thesis and dissertation copies are in typewriter face, while others may be from any type of computer printer.

The quality of this reproduction is dependent upon the quality of the copy submitted. Broken or indistinct print, colored or poor quality illustrations and photographs, print bleedthrough, substandard margins, and improper alignment can adversely affect reproduction.

In the unlikely event that the author did not send UMI a complete manuscript and there are missing pages, these will be noted. Also, if unauthorized copyright material had to be removed, a note will indicate the deletion.

Oversize materials (e.g., maps, drawings, charts) are reproduced by sectioning the original, beginning at the upper left-hand corner and continuing from left to right in equal sections with small overlaps. Each original is also photographed in one exposure and is included in reduced form at the back of the book.

Photographs included in the original manuscript have been reproduced xerographically in this copy. Higher quality 6" x 9" black and white photographic prints are available for any photographs or illustrations appearing in this copy for an additional charge. Contact UMI directly to order.

UMI

RADIATION TRANSPORT IN THE ATMOSPHERE-SEA ICE-OCEAN SYSTEM

A

THESIS

Presented to the Faculty

of the University of Alaska Fairbanks

in Partial Fulfillment of the Requirements

for the Degree of

DOCTOR OF PHILOSOPHY

By

Zhonghai Jin, B.S., M.S.

Fairbanks, Alaska

May 1995

UMI Number: 9605717

UMI

**300 North Zeeb Road
Ann Arbor, MI 48103**

Radiation Transport In The Atmosphere-Sea Ice-Ocean System
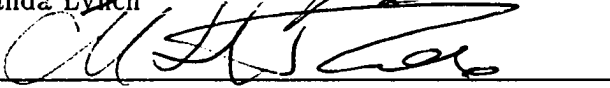
by

Zhonghai Jin

RECOMMENDED:

_____
Dr. Amanda Lynch

_____
Dr. Manfred H. Rees
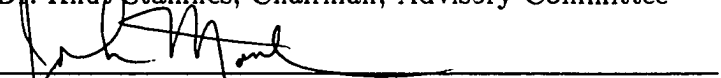
_____
Dr. Glenn E. Shaw

_____
Dr. Si-Chee Tsay

_____
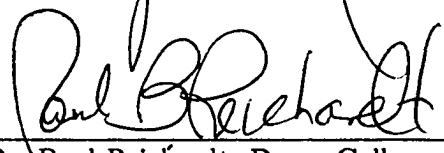Dr. Wilford F. Weeks

_____
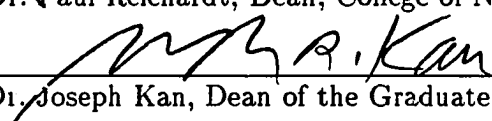Dr. Knut Stamnes, Chairman, Advisory Committee

_____
Dr. John Morack, Head, Physics Department

APPROVED:

_____
Dr. Paul Reichardt, Dean, College of Natural Sciences

_____
Dr. Joseph Kan, Dean of the Graduate School

_____
Date   April 27, 1995

Abstract

A comprehensive radiative transfer model for the coupled atmosphere-sea ice-ocean system has been developed. The theoretical work required for constructing such a coupled model is described first. This work extends the discrete ordinate method, which has been proven to be effective in studies of radiative transfer in the atmosphere, to solve the radiative transfer problem pertaining to a system consisting of two strata with different indices of refraction, such as the atmosphere-ocean system and the atmosphere-sea ice-ocean system. The relevant changes (as compared to the standard problem with constant index of refraction throughout the medium) in formulation and solution of the radiative transfer equation, including the proper application of interface and boundary conditions, are presented.

This solution is then applied to the atmosphere-sea ice-ocean system to study the solar energy balance in this coupled system. The input parameters required by the model are observable physical properties (e.g., the profiles of temperature and gas concentrations in the atmosphere, and the profiles of temperature, density, and salinity in the ice). The atmosphere, sea ice and ocean are each divided into a sufficient number of layers in the vertical to adequately resolve changes in their optical properties. This model rigorously accounts for the multiple scattering and absorption by atmospheric molecules, clouds, snow and sea water, as well as inclusions in the sea ice, such as brine pockets and air bubbles. The effects of various factors on the solar energy distribution in the entire system have been studied quantitatively. These factors include the ice salinity and density variations, cloud microphysics, as well as variations in melt ponds and snow cover on the ice surface.

Finally, the coupled radiative transfer model is used to study the impacts of clouds, snow and ice algae on the light transport in sea ice and in the ocean, as

iii

well as to simulate spectral irradiance and extinction measurements in sea ice.

Contents

List of Figures

List of Tables

Acknowledgments

I would like to give my sincere thanks to my advisor, Knut Stamnes, for his constant support, encouragement and excellent advising through my entire graduate studies; to Dr. Willy Weeks for teaching me what the sea ice is and for helping me on the sea ice modeling; to Dr. Si-Chee Tsay for stimulating discussions and cooperations; to Dr. Martin Jeffries for insights on my thesis work and constructive comments. I would also like to thank all my other committee members (Glenn Show, Manfred Rees, Brenton Watkins, Sue A. Bowling and Amanda Lynch) for their comments, suggestions and criticisms on my thesis. Thanks to Timothy Quakenbush for providing me his measurement data; to Dave Covey and David Bailey for their helps on computer problems. Thanks also to fellows in our group for their cooperation. Finally, I would like to extend my heartfelt gratitude toward my wife, Qingyu Chen, for her years of support and the sacrifice of her education opportunity to accompany me in Alaska.

Chapter 1

Introduction

Solar radiation exhibits much greater seasonal change in the polar regions than at temperate and tropical latitudes, ranging from no insolation during winter to an overall maximum during summer. Due to the co-existence of highly-reflecting sea ice and snow, and low-reflecting open oceans and melt ponds on the ice surface, as well as their constant variation in coverage, the net solar radiation at the surface also experiences great spatial and temporal variations. The surface albedo of sea ice is strongly correlated with the solar radiation because the melting processes are related to the absorption of solar energy. The wide spatial and seasonal variation in surface conditions enhances the variation in solar energy distribution in the polar atmosphere-sea ice-ocean system both temporally and spatially. Sea ice plays an important role for the radiative transfer in this system because it modifies the air-sea energy exchange by increasing the surface albedo and insulating the relatively warm ocean from the cold winter atmosphere. Since sea ice has a significantly higher surface albedo than open water, relatively minor changes in climate could produce large changes in the areal extent of the ice cover and could significantly affect the large-scale transfer of energy between the atmosphere and ocean. In some circumstances this might result in a positive feedback process that would

1

amplify the original change. On the other hand, the radiative forcing by clouds affects the extent, thickness and evolution of the sea ice. The atmosphere, sea ice and ocean interact both directly and indirectly with each other via radiation. The atmospheric structure, clouds, the sea ice state and the sea water below the ice determine the solar radiative energy distribution throughout the system as well as the radiative energy absorbed in the ice and transmitted into the ocean. Radiation absorbed within the sea ice can change the internal structure of the ice and consequently its optical properties. These changes result in an alteration of the radiative energy transmitted into the ocean and reflected back to the atmosphere, which, in turn, affects the stratification and circulation of the atmosphere and the ocean. These radiative interactions can also affect the sensible, latent, and conductive energy exchanges between the subsystems due to the variations in the temperature and state of each layer. Because of the unique and important role played by sea ice in climate, we are thus obliged to devote considerable attention to it in modeling the radiative transfer in the polar system.

Most climate models have included some aspects of the thermodynamics of sea ice. Modern sea ice thermodynamic models, which are aimed at predicting the ice and snow thickness evolution, are based on the surface energy balance including the radiation energy. Results from such thermodynamic models clearly indicate that the equilibrium sea ice thickness is very sensitive to the amount of solar radiation impinging on the upper ice surface and its absorption in the interior of the ice [*Maykut* and *Untersteiner*, 1971; *Semtner*, 1976; *Ebert* and *Curry*, 1993]. Adopting the three layer model of Semtner (1976), Shine and Henderson-Sellers (1985) investigated the sensitivity of the model to changes in surface albedo parameterization. They found that the increase in surface albedo with cloud cover can cause a doubling of ice thickness and that solar radiation codes in models must include the effect of cloud to ground multiple reflection, otherwise the surface net

flux will be significantly underestimated with serious effects on ice thickness and extent. Therefore, accurate determination of the surface radiation fluxes over the Arctic ocean is of particular importance and a radiation scheme is required that consistently and accurately predicts the radiative forcing, including the surface albedo and the absorption in the interior of the ice.

Lacking an extensive understanding of the optical properties of sea ice and a properly coupled radiative transfer model for the atmosphere-sea ice-ocean system, a consistent study of the radiative transfer in the polar atmosphere, snow, sea ice and ocean system has not yet been undertaken. However, numerous investigations of the radiation environment in individual subsystems have been done separately both in experiment and in theory. A brief review of these works will be given below.

The arctic atmosphere is characterized by persistent and prevalent low-level stratiform clouds and wide spread and removal-resistant arctic haze. Due to the low solar elevation, radiative transfer in the polar atmosphere experiences long optical paths through absorbing trace gases. Measurements of the absorption of solar radiation and the optical depths of arctic haze were conducted during the Arctic Gas and Aerosols Sampling Projects in 1983 (AGASP I) and 1986 (AGASP II) [Valero *et al.*, 1984; 1988]. The influence of the haze on the radiation environment has also been investigated by several individuals [Shaw and Stamnes, 1980; Valero *et al.*, 1983; 1988, Tsay *et al.*, 1989; Shaw *et al.*, 1993].

The annual cycle of mean monthly fractional cloud cover in the central Arctic shows a summertime maximum as high as 90% and a minimum of 40% to 50% during winter (Huschke, 1969). The microphysical and radiative properties of summertime arctic clouds were measured during the June 1980 Arctic Stratus Experiment and described by both Herman and Curry [1984] and Tsay and Jayaweera [1984]. Modeling radiation in clouds has also been studied. For example, Wiscombe

(1975) presented a computational scheme for solar radiation under arctic summer stratus conditions, but the dependence of the radiative properties of these clouds on their microphysics was not considered. To examine the dependence of cloud radiative properties on cloud microstructure Tsay et al. [1983] compared the reflectivities and transmissivities of the arctic stratus clouds in the visible spectrum based on three different uniform models of the drop size distribution with those obtained by using the observed nonuniform distributions. Their results showed that the nonuniform nature of the cloud drop size distributions must be taken into account in model calculations aimed at predicting the radiative properties of such clouds. By using the solar radiation model described by Slingo and Schrecker [1982], Herman and Curry [1984] calculated the bulk radiative properties of the clouds (reflection, transmission and absorption) and their results agreed quite well with the values obtained during the Arctic Stratus Experiment. Adopting the discrete ordinate method, Tsay et al. [1989] then developed a comprehensive radiation model and used it to simulate the downward and upward flux profiles measured during the Arctic Stratus Experiment. These results also showed good agreement with observations. Both the models developed by Slingo and Schrecher [1982] and by Tsay et al. [1989] parameterized the optical properties of these clouds in terms of their cloud liquid water content and equivalent radius, and included the scattering and absorption by atmospheric molecules. The optical properties of Arctic Haze and snow were also parameterized in the model of Tsay et al. [1989].

Snow cover is one of the major characteristics in the polar regions. Because of its high albedo and high emissivity, and therefore its importance in controlling the radiation energy budget, radiation in snow has also been studied quite extensively, especially the albedo. Time series of albedos show high all-wave albedos (75-90%) in late winter and early spring, dropping as snow melt begins to about 60% as indicated from measurements in both the Arctic [Langleben, 1971] and in the

Antarctic [Weller, 1968]. The reduction of albedo due to snow aging has been documented for visible wavelengths by Grenfell and Maykut [1977] and for the near infrared by O'Brien and Munis [1975] as well as over the wavelength region from 0.4 to 2.5 μm by Grenfell et al. [1981].

Measurements of the attenuation of solar radiation in snow have been reported by Weller [1969] and by Schwerdtfeger and Weller [1977], as well as by other investigators. The asymptotic flux extinction coefficient has been measured as a function of wavelength by Grenfell and Maykut [1977] and Kuhn and Siogas [1978]. A recent set of observed spectral albedos on the Antarctic Plateau [Grenfell et al., 1994] showed a uniformly high value of 0.96-0.98 across the UV and visible spectrum, which agrees with model predictions for clean snow (unpolluted snow). These spectrally-resolved measurements are better suited for testing theoretical models than are all-wave extinction measurements.

Radiative transfer in snow has also been modelled by many investigators [e.g., Giddings and Lachapelle, 1961; Barkstrom, 1972; Barkstrom and Querfeld, 1975; Bohren and Barkstrom, 1974; Berger, 1979; Wiscombe and Warren, 1980; Choudhury and Chang, 1981]. The early models did not explicitly compute scattering by individual ice grains but set up a two-stream radiative transfer framework, which required two input parameters that were normally found by fitting experimental data. The models developed by Bohren and Barkstrom [1974] and by Choudhury and Chang [1981] started to consider the single scattering by ice grains and applied modern radiative transfer theory. The most accurate model for computing radiative fluxes in snow was developed by Wiscombe and Warren [1980]. This model used Mie theory to calculate the optical properties of snow. The delta-Eddington approximation [Joseph et al., 1976] is used to handle the anisotropic phase function. This model has the capability of simulating the dependence of the spectral albedo on grain size and density, and the results agree quite well with observations.

Brandt and Warren [1993] studied the solar heating rates in Antarctic snow and simulated the sub-surface temperature maximum by using the two-stream radiative transfer model.

Radiation penetration in sea ice and the ocean has recently received more attention due to its strong effect on sea ice decay and consequently on climate. Grenfell and Maykut [1977] carried out a number of measurements of light transmission and reflection in the arctic basin, in which spectral albedos (400 - 1000 nm) and extinction coefficients (400-800 nm) were determined for melt ponds and various types of bare ice. They used the Bouguer-Lambert law to estimate the transmission and absorption within the ice under clear and cloudy skies from total flux measurements at the surface. They found that near the surface, multiyear ice absorbed slightly more energy than did first-year blue ice, but at depths below 10 cm the flux divergence in the first-year ice was three to four times larger than in the multiyear ice. By using a two-stream model and considering the snow, ice and ocean each as one homogeneous layer, Grenfell [1979] investigated the total transmission, absorption and reflection of solar radiation for bare blue and white ice between 0.02 and 0.8 m in thickness as well as for blue ice covered with 0.01 to 0.4 m of dry packed snow. According to this two-stream model, the radiative energy absorption at the surface is independent of ice thickness, but significant departures from Beer's law by as much as 200% are evident in all cases below a depth of 2.5 mm and the total transmission through thin ice (less than 0.8 m) is from 50% to 300% greater than is predicted by Beer's law depending on ice type. Perovich [1990] studied the solar heating of a stratified ocean in the presence of a static ice cover. The contribution of the absorption of shortwave radiation in determining the thermohaline structure of the under ice water was modeled and compared with observations. Results showed that the temperature maximum beneath the ice was established by absorption of solar radiation, regardless of whether leads

were present or not. Based on simple models for the scattering and absorption, Buckley and Trodahl [1987] used the Monte Carlo method to simulate the light transmission in sea ice. They found that a satisfactory fit could be obtained only by assuming a strongly scattering top layer lying above a bulk layer in which the scattering is anisotropic.

Compared with the extensive investigations carried out for the atmosphere and ocean, the investigation of radiative transfer in and the optical properties of sea ice is inadequate, even though sea ice is the most important component controlling the radiative energy balance and light transport in the coupled atmosphere, sea ice and ocean system. The radiation in sea ice is controlled by the absorption of pure ice, as well as by scattering and absorption of inclusions, such as brine pockets, air bubbles, solid salts and other impurities. Based on phase equilibrium constraints and experimental data, Cox and Weeks [1983] developed an equation to relate the fractional volumes of brine pockets, air bubbles and solid salts to the ice temperature, density, and salinity. However, the size distribution of these inclusions and their dependence on temperature, salinity and density is not well understood. Therefore, the dependence of their optical properties on the physical properties is not entirely clear. Most radiation computations in sea ice have been simulated by Beer's law or by a two-stream radiative transfer model. The application of modern radiative transfer theory to sea ice was pioneered by Perovich and Grenfell [1982], who first considered asymmetric scattering in sea ice by a four-stream representation using the discrete ordinate method. Their solution was adjusted to account for the refraction at the air-ice interface. A 16-stream radiative transfer model developed by Grenfell [1983], started to treat scattering by individual particles (air bubbles and brine pockets) and related the optical properties to the initial temperature, salinity, density and growth rate of the ice. The major limitation of this model was that it treated only a single homogeneous layer and, as a re-

sult, was applicable only to a limited set of ice types. Perovich [1990] introduced a multilayer two-stream model based on the formulation of Dunkle and Bevans [1956]. Because the two-stream model considered only one upward and one downward direction, it is most suitable for a uniform radiation field, and it is difficult to correctly account for the refraction at the air-ice interface. Prior to the present work, the most sophisticated radiative transfer model developed for application to sea ice is the multilayer 4-stream model of Grenfell [1991]. This model took into account the refraction at each layer interface and related the optical properties of sea ice to its physical and structural characteristics. Since the same number (four) of streams was used in every layer, some approximations and interpolation had to be applied in an attempt to satisfy the reflection and refraction conditions at the air-ice interface due to the change in refractive index across the interface. Although models that use the same number of streams in the atmosphere and ocean have the advantage of simplicity in implementation, they lack the flexibility to choose the number of streams so as to optimize the computational time for a desired level of accuracy. This lack of flexibility and internal consistency implies that such models are not suitable for providing benchmark results against which approximate (low stream) results could be tested.

The error in radiative transfer modeling is contributed by two sources. One is theoretical, which is related to the methodology used to solve the radiative transfer equation and the magnitude of that error is dependent on the optical properties for a specified method. The other is related to the specification of the model input parameters, the optical or physical properties. These two errors could be made to cancel each other by tuning one or more characteristic parameters if they are not uniquely specified, as they presently are for sea ice. Keeping this in mind, one should perhaps not be surprised to find that good agreement between models and observations is frequently reported, even though large errors are inherent in the

solutions. Therefore, good matching can not necessarily be taken as a verification of the modeling. On the contrary, it may just indicate that the optical properties of the sea ice are poorly specified. To distinguish errors in the specification of sea ice characteristics from the theoretical (and numerical) modeling errors, an accurate radiative transfer model is required. On the other hand, improved accuracy of the ice characterization is needed for improved overall modeling accuracy.

Even in theory, the computational accuracy generally increases with the number of streams when the discrete ordinate method is used to solve the radiative transfer equation. The 2-stream and 4-stream models have the advantage of computational simplicity and in some special circumstances, they do provide adequate accuracy. For example, in the absence of scattering, even Beer's law yields the exact solution; and if the radiation field is isotropic, the 2-stream approximation may yield accurate results. The number of streams required to satisfy a prescribed accuracy is dependent on the optical properties, specifically the scattering asymmetry factor and the single scattering albedo. Unfortunately, the scattering in sea ice is often highly asymmetric and the single scattering albedo over the solar spectrum varies widely, which usually implies that a high number of streams is required to obtain adequate computational accuracy.

The increasing availability of radiative measurements of improved accuracy in the ice, the need to quantify the effects of solar radiation on marine ecosystem in the polar oceans, and the critical role played by sea ice in the radiative transfer process in the entire atmosphere, sea ice and ocean system, call for the development of a comprehensive and accurate radiative transfer model to treat the radiation in sea ice as well as in the coupled system.

On the other hand, all the radiative transfer problems in the atmosphere and in the ice and ocean are presently treated separately. In other words, the radiation computation in the atmosphere is carried out with assumed surface albedo,

whereas the radiation in sea ice and ocean is treated with assumed known incident conditions at the ice surface. Usually uniform illumination is assumed. However, to study the radiative interaction between the atmosphere, clouds, snow, sea ice and ocean, a radiative transfer model with consistent treatment of radiation in the coupled system is needed. To develop such a comprehensive radiative transfer model is the objective of this thesis work.

In chapter 2 of this thesis, I will present the methodology developed to solve the theoretical problem employing the discrete ordinate method (DOM) to solve the radiative transfer equation in a coupled system consisting of two strata with different indices of refraction. The atmosphere-ocean system will be taken as an example.

In chapter 3, the radiative transfer solution for the coupled system will be applied to the atmosphere, sea ice and ocean system to study the solar energy balance in the coupled system and to study the effect of sea ice on the radiative interaction in the whole system.

In chapter 4, application of the radiative transfer model to study the transport of photosynthetically active radiation in sea ice and ocean will be presented. The effects of clouds, ozone, snow and ice algae will be examined.

A summary discussion and conclusions will be presented in chapter 5.

Chapter 2

Radiative Transfer in Non-uniformly Refracting Layered Media

A general equation for the transport of monochromatic radiation in one spatial dimension can be expressed as

$$u\frac{dI(\tau,u,\phi)}{d\tau} = - I(\tau,u,\phi) + \frac{a(\tau)}{4\pi}\int_0^{2\pi} d\phi' \int_{-1}^1 p(\tau,u,\phi,u',\phi')I(\tau,u',\phi')du'$$
$$+ S(\tau,u,\phi) \tag{2.1}$$

where $I(\tau,u,\phi)$ is the unpolarized spectral radiance (omitting index of frequency ν for simplicity) at vertical optical depth τ (measured downward from the upper boundary) and in direction (u,ϕ). Here u is the cosine of the polar angle, which is positive with respect to the upward normal and ϕ is the azimuthal angle. $a(\tau)$ is the single scattering albedo and $p(\tau,u,\phi,u',\phi')$ is the phase function representing the probability of an incident photon in the direction (u',ϕ') being scattered into

---

[0]The first part of this chapter is based on material published as Z. Jin and K. Stamnes, Radiative transfer in nonuniformly refracting layered media: Atmosphere-ocean system, *Appl. Opt.*, *33*, 431-442, 1994.

11

direction (u, ϕ) after a collision with a scattering particle. Thus, the integral term on the right hand side of Eq. (2.1) represents the radiation contributed by scattering from all directions to direction (u, ϕ). $S(\tau, u, \phi)$ represents any internal source of radiation.

The main difference in solving the radiative transfer problem for the atmosphere-ocean system or the atmosphere-sea ice-ocean system from that for the atmosphere only, is that one must take into account the refractive index change at the air-water or air-ice interfaces. A number of radiative transfer models that take refraction into account have been developed for the computation of underwater light fields or for the remote sensing of ocean properties. Some of them simulate a coupled ocean-atmosphere system. Among these models, most have adopted the Monte Carlo technique to solve the radiative transfer equation [e.g., Gordon, 1987; Kattawar and Adams, 1989; Morel and Gentili, 1991; Kirk, 1981; Stavn and Weidemann, 1988], whereas the invariant imbedding technique and the doubling-adding method were used by Mobley [1989] and by Nakajima and Tanaka [1983], respectively. The models differ primarily in the mathematical techniques used to solve Eq. (2.1) and in the treatment of boundary conditions at the ocean surface.

The discrete ordinate method (DOM) [Chandrasekhar, 1960] has been satisfactorily used to solve the radiative transfer problem in a vertically inhomogeneous atmosphere and has been proven to be reliable and efficient [e.g., Liou, 1973, 1975; Stamnes and Swanson, 1981; Stamnes and Conklin, 1984; Stamnes et al. 1988; Tsay et al. 1989]. The principle of the DOM is to convert the integro-differential equation (2.1) into a system of ordinary differential equations by means of a quadrature formula. The contributions of Stamnes and his colleagues have led to an unconditionally stable solution based on this method [Stamnes and Swanson, 1981; Stamnes and Conklin, 1984]. This method has the following unique features: (i) because the solution is analytic, the computational speed is completely inde-

pendent of individual layer and total optical thickness which may be taken to be arbitrarily large. The computational time is directly proportional to the number of horizontal layers used to resolve the vertical inhomogeneity of the optical properties in the media; (ii) accurate irradiances, scalar irradiances and azimuthally-averaged radiance are obtained with just a few streams which makes the code very efficient; (iii) because the solution is analytic, radiances and irradiances can be returned at arbitrary optical depths unrelated to the computational levels; (iv) the DOM is essentially a matrix eigenvalue/eigenvector solution, which implies that the asymptotic solution is automatically obtained. Therefore, the smallest eigenvalue is the asymptotic extinction and the associated eigenvector is the asymptotic radiance.

However, in all previous applications of this method there was no need to consider changes in refractive properties because optically only a single medium with a constant index of refraction was considered. The principal difficulty encountered in attempts to extend the DOM to the atmosphere-ocean system and to the atmosphere-sea ice-ocean system results from the refraction of radiation across the air-water or air-ice interface where refractive index changes occur. The Fresnel refraction and reflection at those interfaces will affect the form of the radiative transfer equation and the particular solutions in the whole system. Consequently, the radiance continuity relations at the interface are totally different from the non-refractive case.

Neglecting the refractive index change at the ice-water interface, the solution of the radiative transfer equation in the atmosphere-sea ice-ocean system is similar to that in the atmosphere-ocean system. For simplicity, I will take the atmosphere-ocean system as an example to demonstrate the procedure of solving radiative transfer in such a coupled system. The air-water interface is assumed to be flat and the atmosphere and ocean are both assumed to be vertically stratified so that the optical properties depend only on the vertical coordinate. To account for any

vertical inhomogeneities, the atmosphere and the ocean can be divided into any suitable number of horizontal layers, as required to resolve the vertical structure of the optical properties of each medium.

In the following sections, I will first derive the formulation of the radiative transfer equation for the coupled system, which is different from that for the uniformly refracting medium. I will then select an appropriate quadrature and apply the DOM to find a general solution which is suitable for every layer. The formulation and procedure required to apply the interface and boundary conditions to such a coupled system will be presented. In section 2 some model consistency tests will be performed. The importance of proper stream distributions in the Fresnel cone and the total reflection region in the ocean to achieving fast convergence is also discussed, as is the effect of scattering asymmetry on convergence. Following that, some examples from applying this formalism to the atmosphere-ocean system are presented in section 3, including comparisons performed with and without the inclusion of the effects arising from changes in the index of refraction at the air-ocean interface in order to demonstrate the importance of including this change. Finally, in section 4 comparisons with several models that use different solving methods are presented.

2.1   Formulation and Solution

Formulation and solution of the radiative transfer equation for the atmosphere-ocean system have many similarities with that for the atmosphere only. Only the differences will be emphasized here. Figure 2.1 schematically illustrates the radiative transfer model for the atmosphere-ocean system. In the ocean, region I is the total reflection region and region II is the refraction region. The width of each region depends on the relative index of refraction of the two media. The downward
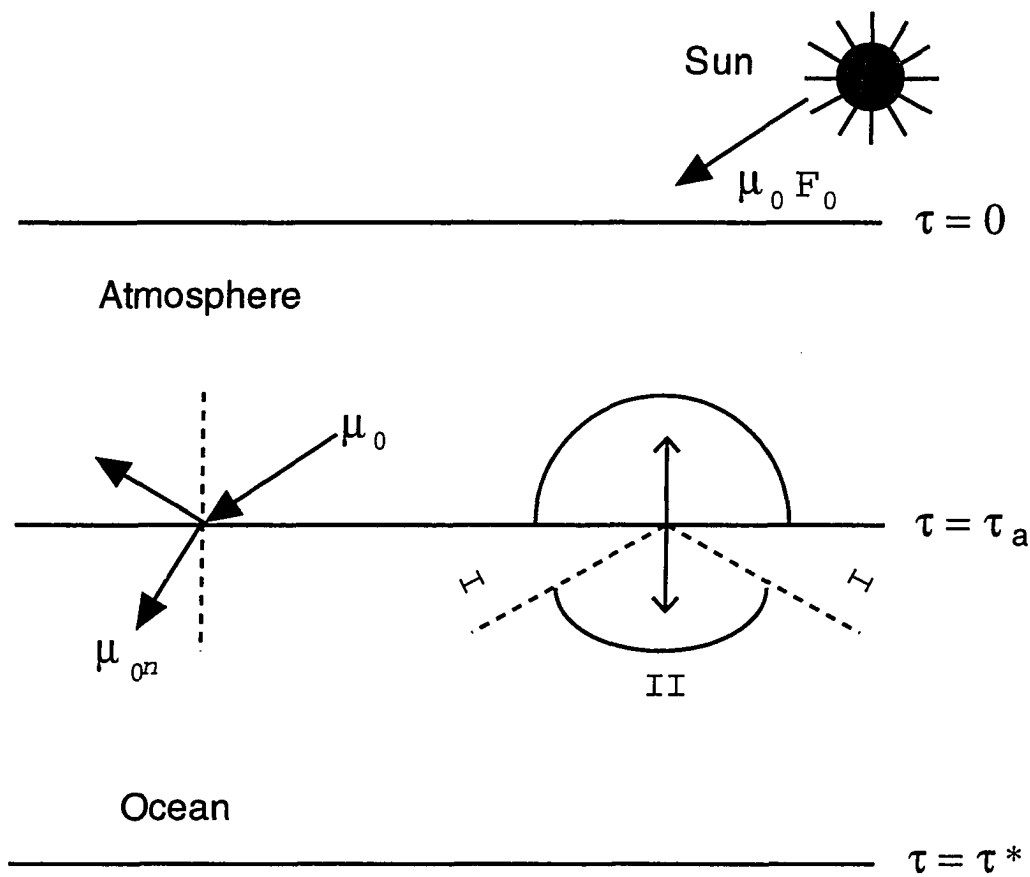
Figure 2.1 Schematic diagram of the coupled radiative transfer model for the atmosphere -ocean system

radiation distributed over 2π steradians in the atmosphere will be restricted to a cone (less than 2π steradians) after being refracted across the interface into the ocean. Photons in region II of the ocean may be scattered into region I. Note, however, that photons in region I of the ocean can not reach the atmosphere directly and vice versa. 'Communication' between the atmosphere and region I has to be achieved through the scattering process between region I and region II in the ocean. As will be demonstrated, all these characteristics for the coupled system can be described by a properly formulated radiative transfer equation and an appropriate implementation.

2.1.1 Basic Equations

For the coupled system, the source term S (for simplicity consider only a solar beam source) in Eq. (2.1) in the atmosphere can be expressed as

$$
\begin{aligned}
S_{air}(\tau, u, \phi) &= \frac{a(\tau)}{4\pi} F^s p(\tau, u, \phi, -\mu_0, \phi_0) \exp(-\tau/\mu_0) \\
&+ \frac{a(\tau)}{4\pi} F^s R(-\mu_0, n) p(\tau, u, \phi, \mu_0, \phi_0) \exp(-(2\tau_a - \tau)/\mu_0) \quad (2.2)
\end{aligned}
$$

where μ_0 is the cosine of the solar zenith angle and is positive, ϕ_0 is the azimuthal angle for the incident solar beam, F^s is the solar beam intensity at the top of the atmosphere, n is the index of refraction of the ocean relative to the atmosphere and τ_a is the total optical depth of the atmosphere. The first term in Eq. (2.2) represents the contribution from the downward incident beam source, while the second term represents the contribution from the upward beam source reflected at the atmosphere-ocean interface because of the Fresnel reflection caused by the change in refractive index between air and sea water. $R(-\mu_0, n)$ is the ocean surface reflectance for the solar beam (see Appendix A for derivation). In the

ocean, the source term can be written as

$$
\begin{aligned}
S_{ocn}(\tau, u, \phi) \;=\;& \frac{a(\tau)}{4\pi}\frac{\mu_0}{\mu_{0n}(\mu_0, n)} F^s T(-\mu_0, n) p(\tau, u, \phi, -\mu_{0n}, \phi_0) \exp(-\tau_a/\mu_0) \\
& \times \; \exp\left[-(\tau - \tau_a)/\mu_{0n}\right] \tag{2.3a}
\end{aligned}
$$

where $T(-\mu_0, n)$ is the transmittance through the interface, and μ_{0n} is the cosine of the solar zenith angle in the ocean, which is related to μ_0 by Snell's law

$$
\mu_{0n}(\mu_0, n) = \sqrt{1 - (1 - \mu_0{}^2)/n^2}. \tag{2.3b}
$$

Equation (2.1) implicitly assumes that the scattering phase function depends only on the scattering angle Θ which is related to the polar and azimuthal angles of the incident and the scattered directions through the cosine law of spherical trigonometry

$$
\cos(\Theta) = uu' + \sqrt{(1 - u^2)(1 - u'^2)}\cos(\phi - \phi'). \tag{2.4}
$$

This relation can be utilized to "isolate" the azimuth-dependence in Eq. (2.1) by the following procedures of expansion and decomposition. Expansion of the phase function $p(\tau, \cos\Theta)$ in a series of 2N Legendre polynomials and the intensity (radiance) in a Fourier cosine series [Chandrasekhar, 1960; Stamnes et al., 1988]

$$
I(\tau, u, \phi) = \sum_{m=0}^{2N-1} I^m(\tau, u) \cos m(\phi - \phi_0) \tag{2.5a}
$$

$$
\begin{aligned}
p(\tau, u, \phi, u', \phi') \;\equiv\;& p(\tau; \cos\Theta) \\
=\;& \sum_{l=0}^{2N-1} (2l + 1) g_l(\tau) P_l(\cos\Theta) \tag{2.5b}
\end{aligned}
$$

leads to the replacement of equation (2.1) with 2N independent equations (one for each Fourier component)

$$
\begin{aligned}
u\frac{dI^m(\tau, u)}{d\tau} \;=\;& -I^m(\tau, u) + \int_{-1}^{1} D^m(\tau, u, u') I^m(\tau, u') du' + S^m(\tau, u) \\
& m = 0, 1, \ldots, 2N - 1 \tag{2.6a}
\end{aligned}
$$

and

$$D^m(\tau, u, u') = \frac{a(\tau)}{2} \sum_{l=m}^{2N-1} (2l+1)g_l(\tau)\frac{(l-m)!}{(l+m)!}P_l^m(u)P_l^m(u') \tag{2.6b}$$

where $P_l^m(u)$ is the associated Legendre polynomial, the expansion coefficient $g_l(\tau)$ is given by

$$g_l(\tau) = \frac{1}{2}\int_{-1}^{1} P_l(\cos\Theta)p(\tau, \cos\Theta)d\cos\Theta \tag{2.6c}$$

and $S^m(\tau, u)$ is the decomposed m^{th} Fourier component of the beam source. In the atmosphere it is

$$S_{air}^m(\tau, u) = X_0^m(\tau, u)\exp(-\tau/\mu_0) + X_{01}^m(\tau, u)\exp(\tau/\mu_0) \tag{2.6d}$$

where

$$\begin{aligned} X_0^m(\tau, u) &= \frac{a(\tau)}{4\pi}F^s(2-\delta_{m0})\sum_{l=0}^{2N-1}(-1)^{l+m}(2l+1)g_l(\tau)\frac{(l-m)!}{(l+m)!} \\ &\times P_l^m(u)P_l^m(\mu_0), \end{aligned} \tag{2.6e}$$

$$\begin{aligned} X_{01}^m(\tau, u) &= \frac{a(\tau)}{4\pi}F^sR(-\mu_0, n)\exp(-2\tau_a/\mu_0)(2-\delta_{m0}) \\ &\times \sum_{l=0}^{2N-1}(2l+1)g_l(\tau)\frac{(l-m)!}{(l+m)!}P_l^m(u)P_l^m(u_0) \end{aligned} \tag{2.6f}$$

$$\delta_{m0} = \begin{cases} 1, & \text{if m=0;} \\ 0, & \text{otherwise.} \end{cases} \tag{2.6g}$$

The mth Fourier component of the source term in the ocean can be expressed as

$$S_{ocn}^m(\tau, u) = X_{02}^m(\tau, u)\exp(-\tau/\mu_{0n}), \tag{2.6h}$$

where

$$\begin{aligned} X_{02}^m(\tau, u) &= \frac{a(\tau)}{4\pi}\frac{\mu_0}{\mu_{0n}(\mu_0, n)}T(-\mu_0, n)F^s\exp[-\tau_a(\frac{1}{\mu_0} - \frac{1}{\mu_{0n}})](2-\delta_{m0}) \\ &\times \sum_{l=0}^{2N-1}(-1)^{l+m}(2l+1)g_l(\tau)\frac{(l-m)!}{(l+m)!}P_l^m(u)P_l^m(\mu_{0n}). \end{aligned} \tag{2.6i}$$

The solution of equation (2.1) has now been transformed into solving a series of ϕ-independent equations (2.6a).

2.1.2 Quadrature Rule and Discrete Ordinate Approximation

The discrete ordinate approximation to (2.6a) is obtained by replacing the integral in equation (2.6a) by a quadrature sum and thereby transforming the integro-differential equation (6a) into a system of coupled differential equations. Thus, for each layer in the atmosphere, we obtain [Stamnes et al., 1988]

$$
\mu_i^a \frac{dI^m(\tau, \mu_i^a)}{d\tau} = -I^m(\tau, \mu_i^a) + \sum_{\substack{j=-N_1 \\ j \neq 0}}^{N_1} w_j^a D^m(\tau, \mu_i^a, \mu_j^a) I^m(\tau, \mu_j^a)
$$
$$
+ S_{air}^m(\tau, \mu_i^a), \qquad i = \pm 1, \ldots, \pm N_1, \qquad (2.7a)
$$

and similarly, for layers in the ocean, we find

$$
\mu_i^o \frac{dI^m(\tau, \mu_i^o)}{d\tau} = -I^m(\tau, \mu_i^o) + \sum_{\substack{j=-N_2 \\ j \neq 0}}^{N_2} w_j^o D^m(\tau, \mu_i^o, \mu_j^o) I^m(\tau, \mu_j^o)
$$
$$
+ S_{ocn}^m(\tau, \mu_i^o), \qquad i = \pm 1, \ldots, \pm N_2 \qquad (2.7b)
$$

where μ_i^a, w_i^a and μ_i^o, w_i^o are quadrature points and weights for atmosphere and ocean respectively and $\mu_{-i} = -\mu_i$, $w_{-i} = w_i$. The quadrature structure is shown in Figure 2.2. Note that instead of using a constant number of streams for each layer as usual, we have used different numbers of streams for the atmosphere and the ocean ($2N_1$ and $2N_2$, respectively). In region II of the ocean, which communicates directly with the atmosphere, we use the same number of streams ($2N_1$) as in the atmosphere. This properly accounts for the shrinking caused by refraction of the angular domain in the ocean. In region I of the ocean, where total reflection of photons moving in the upward direction occurs at the ocean-atmosphere interface, we invoke additional streams ($2N_2 - 2N_1$) to accommodate the scattering interaction between regions I and II in the ocean. Although there are many
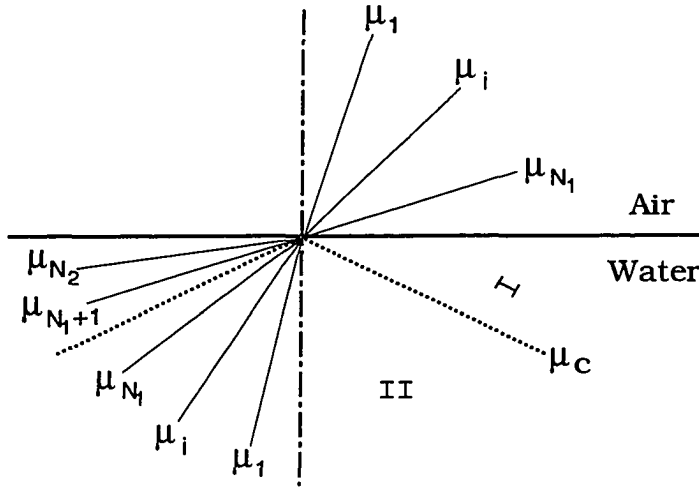
Figure 2.2 Schematic illustration of the discrete directions in the atmosphere and the ocean .

options for choosing a quadrature, this choice will strongly affect the application of interface continuity conditions and the accuracy of the solution. The Double Gauss quadrature rule is used to determine the quadrature points and weights, μ_i^a and w_i^a ($i = 1, \ldots, N_1$), in the atmosphere, as well as the quadrature points and weights, μ_i^o and w_i^o ($i = N_1 + 1, \ldots, N_2$), in the total reflection region of the ocean. The quadrature points in the Fresnel cone of the ocean are obtained by simply 'refracting' the downward 'streams' in the atmosphere, $[\mu_1^a, \ldots, \mu_{N_1}^a]$, into the ocean [Nakajima and Tanaka, 1983; Tanaka and Nakajima, 1977]. Thus, in this region, μ_i^o is related to μ_i^a by Snell's law,

$$\mu_i^o = f(\mu_i^a) = \sqrt{1 - (1 - (\mu_i^a)^2)/n^2}, \qquad i = 1, 2, \ldots, N_1 \tag{2.8}$$

and from this relation, the weights for this region can be derived as

$$w_i^o = w_i^a \left[\frac{df(\mu^a)}{d\mu^a} \right]_{\mu^a = \mu_i^a} = \frac{\mu_i^a}{n^2 f(\mu_i^a)} w_i^a, \qquad i = 1, 2, \ldots, N_1. \tag{2.9}$$

The advantage of this choice of quadrature is that the quadrature points are clustered towards the $\mu = 0$ directions both in the atmosphere and the ocean, and in addition, towards the critical angle direction in the ocean. This clustering gives superior results near these directions where the radiances vary rapidly. Also, this choice of quadrature will simplify the application of the interface continuity condition and avoids the loss of accuracy incurred by the interpolation necessitated by adopting the same quadrature i.e., the same number of streams, for the atmosphere and the ocean.

Finally, it is easy to show that the chosen quadrature points and weights make phase function renormalization unnecessary, so that energy conservation is satisfied automatically as pointed out first by Wiscombe [1977].

2.1.3 Solution

An accurate, reliable and efficient method to obtain the solution of the homogeneous version of Equation (2.7a) or (2.7b) was presented by Stamnes and Swanson [1981]. Following the same procedure, we directly give the homogeneous solution here for simplicity. In the atmosphere, it is (omitting hereafter superscript m denoting the Fourier components)

$$I(\tau,\mu_i^a) = \sum_{j=1}^{N_1}\{C_{-j}G_{-j}(\mu_i^a)\exp(k_j\tau)+C_jG_j(\mu_i^a)\exp(-k_j\tau)\}, \qquad i = \pm 1,\ldots,\pm N_1,$$

$$(2.10a)$$

and similarly, in the ocean

$$I(\tau,\mu_i^o) = \sum_{j=1}^{N_2}\{C_{-j}G_{-j}(\mu_i^o)\exp(k_j\tau) + C_jG_j(\mu_i^o)\exp(-k_j\tau)\}, \qquad i = \pm 1,\ldots,\pm N_2$$

$$(2.10b)$$

where the k_j and G_j are eigenvalues and eigenvectors determined by solving an algebraic eigenvalue problem, and the C_j are unknown 'constants of integration'

to be determined by the application of boundary and continuity conditions as discussed below.

As for the particular solution, in the atmosphere it can be expressed as

$$U(\tau, \mu_i^a) = Z_0(\mu_i^a)\exp(-\tau/\mu_0) + Z_{01}(\mu_i^a)\exp(\tau/\mu_0) \qquad (2.11a)$$

where $i = \pm 1, \pm 2, \ldots, \pm N_1$, and the coefficients $Z_0(\mu_i^a)$ and $Z_{01}(\mu_i^a)$ are determined by the following system of linear algebraic equations

$$\sum_{\substack{j=-N_1 \\ j\neq 0}}^{N_1} \{(1 + \frac{\mu_j^a}{\mu_0})\delta_{ij} - w_j^a D(\tau, \mu_i^a, \mu_j^a)\}Z_0(\mu_j^a) = X_0(\tau, \mu_i^a), \qquad (2.11b)$$

$$\sum_{\substack{j=-N_1 \\ j\neq 0}}^{N_1} \{(1 - \frac{\mu_j^a}{\mu_0})\delta_{ij} - w_j^a D(\tau, \mu_i^a, \mu_j^a)\}Z_{01}(\mu_i^a) = X_{01}(\tau, \mu_i^a). \qquad (2.11c)$$

The particular solution in the ocean can be expressed as

$$U(\tau, \mu_i^o) = Z_{02}(\mu_i^o)\exp[-\tau/\mu_{0n}(\mu_0, n)], \qquad (2.12a)$$

where $i = \pm 1, \pm 2, \ldots, \pm N_2$, and $Z_{02}(\mu_i^o)$ is determined by the following system of linear algebraic equations

$$\sum_{\substack{j=-N_2 \\ j\neq 0}}^{N_2} [(1 + \frac{\mu_j^o}{\mu_{0n}})\delta_{ij} - w_j^o D(\tau, \mu_i^o, \mu_j^o)]Z_{02}(\mu_j^o) = X_{02}(\tau, \mu_i^o). \qquad (2.12b)$$

The general solution is just the sum of the homogeneous solution and the particular solution.

2.1.4 Boundary and Interface Conditions

The vertically inhomogeneous medium is represented by multiple adjacent homogeneous layers in the atmosphere and the ocean, respectively. The solutions derived previously will be used in each layer. We assume that the system consists of L_1

layers of atmosphere and L_2 layers of ocean. Then we may write the solution for the pth layer as

$$I_p(\tau, \mu_i^a) = \sum_{j=1}^{N_1}\{C_{-jp}G_{-jp}(\mu_i^a)\exp(k_{jp}\tau) + C_{jp}G_{jp}(\mu_i^a)\exp(-k_{jp}\tau)\} + U_p(\tau, \mu_i^a),$$
$$i = \pm 1, \ldots, \pm N_1 \quad \text{and} \quad p \leq L_1, \tag{2.13}$$

$$I_p(\tau, \mu_i^o) = \sum_{j=1}^{N_2}\{C_{-jp}G_{-jp}(\mu_i^o)\exp(k_{jp}\tau) + C_{jp}G_{jp}(\mu_i^o)\exp(-k_{jp}\tau)\} + U_p(\tau, \mu_i^o),$$
$$i = \pm 1, \ldots, \pm N_2 \quad \text{and} \quad L_1 < p \leq L_1 + L_2. \tag{2.14}$$

Totally there are $2N_1 \times L_1 + 2N_2 \times L_2$ unknown coefficients C_{jp} in equations (2.13) and (2.14). They will be determined by (i) the boundary conditions to be applied at the top of the atmosphere and the bottom of the ocean, (ii) continuity conditions at each interface between layers in the atmosphere and ocean, and finally (iii) the reflection and refraction occurring at the atmosphere/ocean interface where we require Fresnel's equations to be satisfied.

These conditions are implemented as follows:
at the top of atmosphere, we require

$$I_1(0, -\mu_i^a) = I_\infty(-\mu_i^a), \qquad i = 1, \ldots, N_1; \tag{2.15a}$$

at the interfaces between atmospheric layers,

$$I_p(\tau_p, \mu_i^a) = I_{p+1}(\tau_p, \mu_i^a), \qquad i = \pm 1, \ldots, \pm N_1, \quad \text{and} \quad p = 1, \ldots, L_1 - 1; \tag{2.15b}$$

at the interface between atmosphere and ocean,

$$I_{L_1}(\tau_a, \mu_i^a) = I_{L_1}(\tau_a, -\mu_i^a)R(-\mu_i^a, n) + [I_{L_1+1}(\tau_a, \mu_i^o)/n^2]T(+\mu_i^o, n),$$
$$i = 1, 2, \ldots, N_1; \tag{2.15c}$$

$$I_{L_1+1}(\tau_a, -\mu_i^o)/n^2 = [I_{L_1+1}(\tau_a, \mu_i^o)/n^2]R(+\mu_i^o, n)$$
$$+ \ I_{L_1}(\tau_a, -\mu_i^a)T(-\mu_i^a, n), \qquad i = 1, 2, \ldots, N_1; \tag{2.15d}$$

$$I_{L_1+1}(\tau_a, -\mu_i^o) = I_{L_1+1}(\tau_a, \mu_i^o), \qquad i = N_1 + 1, \ldots, N_2; \qquad (2.15e)$$

at the interfaces between ocean layers,

$$I_p(\tau_p, \mu_i^o) = I_{p+1}(\tau_p, \mu_i^o), \qquad i = \pm 1, \ldots, \pm N_2, \quad p = L_1 + 1, \ldots, L_1 + L_2 - 1;$$

$$(2.15f)$$

and finally at the bottom boundary,

$$I_{L_1+L_2}(\tau^*, \mu_i^o) = I_g(\mu_i^o), \qquad i = 1, 2, \ldots, N_2. \qquad (2.15g)$$

We defined $R(\pm\mu_i, n)$ and $T(\pm\mu_i, n)$ as the specular reflectance and transmittance of the invariant intensity (radiance), I/n_{abs}^2 (n_{abs} is the absolute index of refraction at the location where I is measured). The minus sign applies to the downward intensity, and the positive to the upward intensity. Formulas for R and T can be derived from the basic Fresnel equations. The results are [see Appendix A for detailed derivation]

$$R(-\mu_i^a, n) = \frac{1}{2}\left\{\left(\frac{\mu_i^a - n\mu_i^o}{\mu_i^a + n\mu_i^o}\right)^2 + \left(\frac{\mu_i^o - n\mu_i^a}{\mu_i^o + n\mu_i^a}\right)^2\right\}, \qquad (2.16a)$$

$$R(+\mu_i^o, n) = R(-\mu_i^a, n), \qquad (2.16b)$$

$$T(-\mu_i^a, n) = 2n\mu_i^a\mu_i^o\left\{\left(\frac{1}{\mu_i^a + n\mu_i^o}\right)^2 + \left(\frac{1}{\mu_i^o + n\mu_i^a}\right)^2\right\}, \qquad (2.16c)$$

$$T(+\mu_i^o, n) = T(-\mu_i^a, n). \qquad (2.16d)$$

Equations (2.15c) and (2.15d) ensure that, by satisfying Fresnel's equations, the radiation fields in the atmosphere and the ocean are properly coupled through the interface, whereas equation (2.15e) represents the total reflection in region I in the ocean. The total optical depth of the atmosphere and ocean is denoted by τ^* in equation (2.15g). $I_\infty(-\mu_i^a)$ is the intensity incident at the top of the atmosphere, and $I_g(\mu_i^o)$ is determined by the bidirectional reflectance distribution function (BRDF) of the underlying surface at the bottom of the ocean. The

accurate specification of the BRDF is obviously important only for shallow waters. Substitution of equations (2.13) and (2.14) into equations (2.15a)-(2.15g) yields

$$\sum_{j=1}^{N_1} \{C_{j1}G_{j1}(-\mu_i^a) + C_{-j1}G_{-j1}(-\mu_i^a)\} = I_\infty(-\mu_i^a) - U_1(0, -\mu_i^a), \qquad i = 1, \ldots, N_1$$

$$(2.17a)$$

$$\sum_{j=1}^{N_1} \{C_{jp}G_{jp}(\mu_i^a)e^{-k_{jp}\tau_p} + C_{-jp}G_{-jp}(\mu_i^a)e^{k_{jp}\tau_p}$$

$$- \left[C_{j,p+1}G_{j,p+1}(\mu_i^a)e^{-k_{j,p+1}\tau_p} + C_{-j,p+1}G_{-j,p+1}(\mu_i^a)e^{k_{j,p+1}\tau_p}\right]\}$$

$$= U_{p+1}(\tau_p, \mu_i^a) - U_p(\tau_p, \mu_i^a), \qquad i = \pm 1, \ldots, \pm N_1; p = 1, \ldots, L_1 - 1 \quad (2.17b)$$

$$\sum_{j=1}^{N_1} \{C_{j,L_1} \left[G_{j,L_1}(\mu_i^a) - R(-\mu_i^a, n)G_{j,L_1}(-\mu_i^a)\right] e^{-k_{j,L_1}\tau_a}$$

$$+ \ C_{-j,L_1} \left[G_{-j,L_1}(\mu_i^a) - R(-\mu_i^a, n)G_{-j,L_1}(-\mu_i^a)\right] e^{k_{j,L_1}\tau_a}\}$$

$$- \ \sum_{j=1}^{N_2} \left[C_{j,L_1+1}G_{j,L_1+1}(\mu_i^o)e^{-k_{j,L_1+1}\tau_a} - C_{j,L_1+1}G_{j,L_1+1}(\mu_i^o)e^{k_{j,L_1+1}\tau_a}\right] \frac{T(+\mu_i^o, n)}{n^2}$$

$$= \ \frac{T(+\mu_i^o, n)}{n^2}U_{L_1+1}(\tau_a, \mu_i^o) - U_{L_1}(\tau_a, \mu_i^a), \qquad i = 1, 2, \ldots, N_1 \qquad (2.17c)$$

$$\sum_{j=1}^{N_1}[C_{j,L_1}G_{j,L_1}(-\mu_i^a)e^{-k_{j,L_1}\tau_a} + C_{-j,L_1}G_{-j,L_1}(-\mu_i^a)e^{k_{j,L_1}\tau_a}]T(-\mu_i^a, n)$$

$$- \ \sum_{j=1}^{N_2}\{C_{j,L_1+1}[\frac{R(+\mu_i^o, n)}{n^2}G_{j,L_1+1}(\mu_i^o) - \frac{1}{n^2}G_{j,L_1+1}(-\mu_i^o)]e^{-k_{j,L_1+1}\tau_a}$$

$$+ \ C_{-j,L_1+1}[\frac{R(+\mu_i^o, n)}{n^2}G_{-j,L_1+1}(\mu_i^o) - \frac{1}{n^2}G_{-j,L_1+1}(-\mu_i^o)]e^{k_{j,L_1+1}\tau_a}\}$$

$$= \ \frac{1}{n^2}U_{L_1+1}(\tau_a, -\mu_i^o) - \frac{R(+\mu_i^o, n)}{n^2}U_{L_1+1}(\tau_a, \mu_i^o) - T(-\mu_i^a, n)U_{L_1}(\tau_a, -\mu_i^a),$$

$$i = 1, 2, \ldots, N_1 \qquad (2.17d)$$

$$\sum_{j=1}^{N_2}\{C_{j,L_1+1}[G_{j,L_1+1}(\mu_i^o) - G_{j,L_1+1}(-\mu_i^o)]e^{-k_{j,L_1}\tau_a}$$

$$+ \ C_{-j,L_1+1}[G_{-j,L_1+1}(\mu_i^o) - G_{-j,L_1+1}(-\mu_i^o)]e^{k_{j,L_1}\tau_a}\}$$

$$= \ U_{L_1+1}(\tau_a, -\mu_i^o) - U_{L_1+1}(\tau_a, \mu_i^o), \qquad i = N_1 + 1, \ldots, N_2 \qquad (2.17e)$$

$$\sum_{j=1}^{N_2} \{C_{jp} G_{jp}(\mu_i^o) e^{-k_{jp}\tau_p} + C_{-jp} G_{-jp}(\mu_i^o) e^{k_{jp}\tau_p}$$

$$- \left[C_{j,p+1} G_{j,p+1}(\mu_i^o) e^{-k_{j,p+1}\tau_p} + C_{-j,p+1} G_{-j,p+1}(\mu_i^o) e^{k_{j,p+1}\tau_p}\right] \}$$

$$= U_{p+1}(\tau_p, \mu_i^o) - U_p(\tau_p, \mu_i^o), \qquad i = \pm 1, \ldots, \pm N_2; p = 1, \ldots, L_1 + L_2 - 1 \quad (2.17f)$$

$$\sum_{j=1}^{N_2} [C_{j,L_1+L_2} G_{j,L_1+L_2}(\mu_i^o) e^{-k_{j,L_1+L_2}\tau^*} + C_{-j,L_1+L_2} G_{-j,L_1+L_2}(\mu_i^o) e^{k_{j,L_1+L_2}\tau^*}]$$

$$= I_g(\mu_i^o) - U_{L_1+L_2}(\tau^*, \mu_i^o) \qquad i = 1, 2, \ldots, N_2 \qquad (2.17g)$$

Equation (2.17) constitute a system of $(2N_1 \times L_1) + (2N_2 \times L_2)$ linear algebraic equations from which the same number of unknown coefficients, the $C_{\pm jp}$, are determined. Matrix inversion of this system of equations yields the desired coefficients and thereby completes the solution for the coupled atmosphere-ocean system. However, it is completed only mathematically not numerically, because equations (2.17) are intrinsically ill-conditioned.

2.1.5 Scaled Solution

In situations of large optical depth, the positive exponentials in Equation (2.17) will cause numerical overflows during the execution of the computer program and the system of algebraic equations resulting from straightforward application of Equation (2.17) is notoriously ill-conditioned. To avoid these numerical overflow and ill-conditioning problems, it is necessary to remove the positive exponentials in Equations (2.17). This is achieved by the scaling transformation [Stamnes and Conklin, 1984]

$$C_{+jp} = C'_{+jp} e^{k_{jp}\tau_{p-1}} \qquad and \qquad C_{-jp} = C'_{-jp} e^{-k_{jp}\tau_p}. \qquad (2.18)$$

By this transformation, instead of solving for the C_{jp} in Equation (2.17) one solves an algebraic equation for the C'_{jp} for which the numerical scheme is unconditionally

stable. Detailed discussion of the scaling transformation was given by Stamnes and Conklin [1984]. Here only the simplest case for the atmosphere-ocean system is demonstrated as an example. This case consists of one layer of atmosphere where 2-stream is to be used and one layer of ocean where 4-stream is to be applied (i.e., $L_1 = 1$; $L_2 = 1$; $N_1 = 1$; $N_2 = 2$). Upon substitution of these parameters into Equation (2.17), the right hand side of (2.17) can be written in matrix form as

$$
\begin{bmatrix}
A_{11} & A_{12} & 0 & 0 & 0 & 0 \\
A_{21}e^{-k_{1,1}\tau_1} & A_{22}e^{k_{1,1}\tau_1} & A_{23}e^{-k_{2,2}\tau_1} & A_{24}e^{-k_{1,2}\tau_1} & A_{25}e^{k_{1,2}\tau_1} & A_{26}e^{k_{2,2}\tau_1} \\
A_{31}e^{-k_{1,1}\tau_1} & A_{32}e^{k_{1,1}\tau_1} & A_{33}e^{-k_{2,2}\tau_1} & A_{34}e^{-k_{1,2}\tau_1} & A_{35}e^{k_{1,2}\tau_1} & A_{36}e^{k_{2,2}\tau_1} \\
0 & 0 & A_{43}e^{-k_{2,2}\tau_1} & A_{44}e^{-k_{1,2}\tau_1} & A_{45}e^{k_{1,2}\tau_1} & A_{46}e^{k_{2,2}\tau_1} \\
0 & 0 & A_{53}e^{-k_{2,2}\tau_2} & A_{54}e^{-k_{1,2}\tau_2} & A_{55}e^{k_{1,2}\tau_2} & A_{56}e^{k_{2,2}\tau_2} \\
0 & 0 & A_{63}e^{-k_{2,2}\tau_2} & A_{64}e^{-k_{1,2}\tau_2} & A_{65}e^{k_{1,2}\tau_2} & A_{66}e^{k_{2,2}\tau_2}
\end{bmatrix}
\begin{bmatrix}
c_{1,1} \\ c_{-1,1} \\ c_{2,2} \\ c_{1,2} \\ c_{-1,2} \\ c_{-2,2}
\end{bmatrix}
$$

where the A_{ij} are the factors multiplying the $C_{i,j}$ in equation (2.17). These factors can be obtained easily by applying the given values for L_1, L_2, N_1 and N_2 to Equation (2.17) (this tedious procedure was omitted here for simplicity). This matrix is obviously ill-conditioned (because of the exponentials with positive arguments) and has to be scaled by (2.18) as follows to remove this flaw.

The scaling leaves the first column in the above matrix unchanged, while the rest of the columns are multiplied by exponential factors as follows: column 2 by $e^{-k_{1,1}\tau_1}$, column 3 by $e^{k_{2,2}\tau_1}$, column 4 by $e^{k_{1,2}\tau_1}$, column 5 by $e^{-k_{1,2}\tau_2}$ and finally column 6 by $e^{-k_{2,2}\tau_2}$. The resulting matrix has elements which are either constants, A_{ij}, or else constants A_{ij} multiplied with exponentials whose arguments are negative and proportional to τ_1 or $(\tau_2 - \tau_1)$. Thus, it is obvious that this matrix is

well-conditioned and that it in the limit of large values of τ_1 or $(\tau_2 - \tau_1)$ reduces to

$$
\begin{bmatrix}
A_{11} & 0 & 0 & 0 & 0 & 0 \\
0 & A_{22} & A_{23} & A_{24} & 0 & 0 \\
0 & A_{32} & A_{33} & A_{34} & 0 & 0 \\
0 & 0 & A_{43} & A_{44} & 0 & 0 \\
0 & 0 & 0 & 0 & A_{55} & A_{56} \\
0 & 0 & 0 & 0 & A_{65} & A_{66}
\end{bmatrix}
$$

which shows that the ill-conditioning problem has been entirely eliminated.

The characteristic of the coefficient matrix is that it is a diagonal band matrix (i.e., only the elements in the diagonal band are non-zero). This structure should be exploited to make the solution of the algebraic equation more efficient, especially for large numbers of layers when large numbers of elements in the upper-right and lower-left triangles are zero. However, due to the fact that the stream number used in the different layers is not constant for the coupled system, the band coefficient matrix is no longer symmetric in structure. Some examples of the coefficient matrix will be demonstrated in Appendix B.

Substituting the coefficients C'_{jp} obtained from the equations above to Equations (2.13) and (2.14) yields the azimuthal components of the radiance (intensity). Once the solutions for each (and all) Fourier components have been determined, we may compute the radiance at the quadrature directions from equation (2.5a). Since the fluxes and the mean intensity (the total scalar irradiance divided by 4π in oceanographic terminology [Morel and Smith, 1982]) are azimuthally integrated quantities, only the $m = 0$ (azimuth-independent) component contributes. Therefore the downward and upward fluxes (irradiances) $F^{\pm}(\tau)$ and the mean intensity $\bar{I}(\tau)$ at optical depth τ can be computed according to the following formulas [Stamnes, 1986]

$$
F^{\pm}(\tau) = \int_0^{2\pi} d\phi \int_0^1 \mu I(\tau, \pm\mu, \phi) d\mu
$$

$$= 2\pi \sum_{i=1}^{N} w_i \mu_i I^0(\tau, \pm \mu_i) \qquad (2.19)$$

$$\begin{aligned} \bar{I}(\tau) &= \frac{1}{4\pi} \int_0^{2\pi} d\phi \int_{-1}^{1} I(\tau, u, \phi) du \\ &= \frac{1}{2} \sum_{\substack{i=-N \\ i \neq 0}}^{N} w_i I^0(\tau, \mu_i) \end{aligned} \qquad (2.20)$$

and the downward scalar irradiance (E_{od}) and the upward scalar irradiance (E_{ou}) can be written as

$$\begin{aligned} E_{od}(\tau) &= \frac{1}{2\pi} \int_0^{2\pi} d\phi \int_{-1}^{0} I(\tau, \mu, \phi) d\mu \\ &= \sum_{i=1}^{N} w_i I^0(\tau, -\mu_i) \end{aligned} \qquad (2.21)$$

$$\begin{aligned} E_{ou}(\tau) &= \frac{1}{2\pi} \int_0^{2\pi} d\phi \int_0^{1} I(\tau, \mu, \phi) d\mu \\ &= \sum_{i=1}^{N} w_i I^0(\tau, \mu_i) \end{aligned} \qquad (2.22)$$

Since Eqs. (2.19)-(2.22) are general formulas, when these are applied to actual computations the quadrature number N as well as the quadrature directions μ_i and weights w_i are different in the atmosphere from those in the ocean.

The net downward flux (total irradiance) $F(\tau)$ and the flux divergence $\frac{dF(\tau)}{dz}$ at depth z can be expressed as

$$F(\tau) = F^-(\tau) - F^+(\tau) \qquad (2.23)$$

$$\frac{dF(\tau)}{dz} = 4\pi\alpha(z)\bar{I}(\tau) \qquad (2.24)$$

where $\alpha(z)$ is the absorption coefficient at depth z. Thus, in the absence of thermal emission sources, the radiative flux divergence is equal to the absorption of solar radiation per unit volume at depth z. Remember that the radiative quantities

above are monochromatic, so integrations of Eqs. (2.19)-(2.24) over frequency or wavelength are needed to produce the corresponding radiative quantities over a specified spectral region.

2.2 Model Tests

Before considering actual applications, I will present a number of consistency and convergence tests aimed at checking the basic soundness of the solution. First, consider a conservative situation, in which there is no absorption in the whole system. In other words, we replace the atmosphere and the ocean with two strata consisting of media with different refractive indices, but without absorption. At the bottom of the lower stratum, we assume that the 'surface' is totally reflecting. The variation in irradiances with the relative index of refraction n at four particular levels is shown in Figure 2.3. The effect of adding some absorption is also illustrated. The net irradiance is defined in (2.23) which is the difference between the total downward irradiance and total upward irradiance. In the conservative case, the net irradiance is zero everywhere consistent with the energy conservation requirement, so that the total upward irradiance everywhere overlaps with the total downward irradiance. The total downward and upward irradiances increase rapidly with increasing n in the lower stratum, but not in the upper stratum because of the "energy trapping" in the total reflection region as discussed by Stavn et al. [1984] and by Plass et al. [1981]. Figure 2.3 also shows that the variation in the irradiances with n is very sensitive to the absorption in the lower medium. A single scattering albedo of 0.9 just in the lower medium leads to a drastic reduction of the irradiance changes versus n as compared to the conservative case. At the bottom, the overlap of total upward irradiance with the total downward irradiance for this absorptive case is due to the assumed bottom surface albedo of

Optical Depth = 0.0 (Top)

Just Above The Interface

Just Below The Interface

Optical Depth = 2.00 (Bottom)
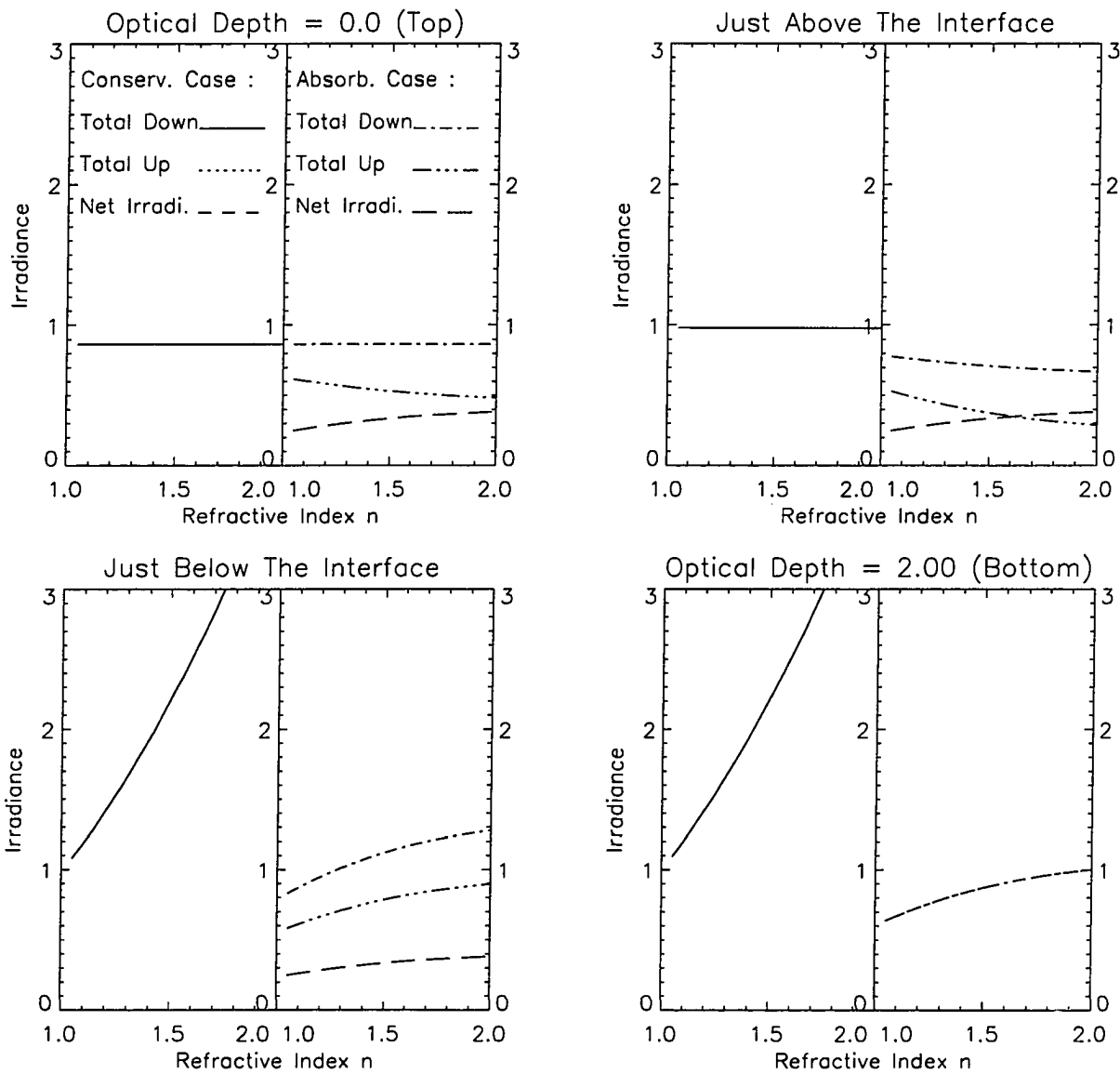
Figure 2.3 Variation of irradiances with the relative index of refraction at several locations for isotropic scattering, incident flux $F^s = 1.0$ with incident zenith angle $\theta_0 = 30^\circ$, bottom surface albedo=1.0, $\tau_a = 1.0$, and $\tau^* = 2.0$. For the absorption case, the only difference from the conservative case is that the single scattering albedo $a = 0.9$ in the lower medium.

unity. The results shown in Figure 2.3 pertain to isotropic scattering, but we have verified by computations that the choice of phase function and optical depth does not significantly affect the general behavior of the irradiances indicated above for the case of an absorbing lower medium, and there is no effect for the conservative case.

As just discussed, in the conservative case with a surface albedo of unity, the upward irradiance should equal the total downward irradiance at the top. This suggests that for the conservative case the incident downward irradiance, which is equivalent to $\mu_0 F^s$, can be taken as a 'benchmark' for the total upward irradiance computation at the top. Figure 2.4 shows the computed upward irradiances at the top obtained by using different streams and their comparison with the 'benchmark' with the same conditions as in Figure 2.3 but with an asymmetry factor of 0.7 for the Henyey-Greenstein phase function used here. The number ratio represents $2N_1/(2N_2 - 2N_1)$, the number of streams adopted within the refractive region divided by that adopted for the total reflective region. The results indicate that although an increase in the number of streams will eventually increase the accuracy, the convergence depends strongly on n for a given combination of streams in the two regions. For example, the upper left panel of Figure 2.4 indicates that the combination '4/2' (four streams for region II and two streams for region I) will produce best accuracy for smaller values of n (about 1.1 to 1.2). The combination '4/4' is best for n between 1.3 and 1.5, while the combination '4/6' is better for larger n. Furthermore, as demonstrated in the other three panels, when the number of streams are increased in both regions, the overall accuracy increases as it should. Our computations also show that the convergence behavior indicated above is true at any level. Generally, for larger n, to obtain optimal results, one must assign more streams to the total reflective region because it becomes wider. Experience has shown that the quantitative relation between this optimum 'stream' ratio and
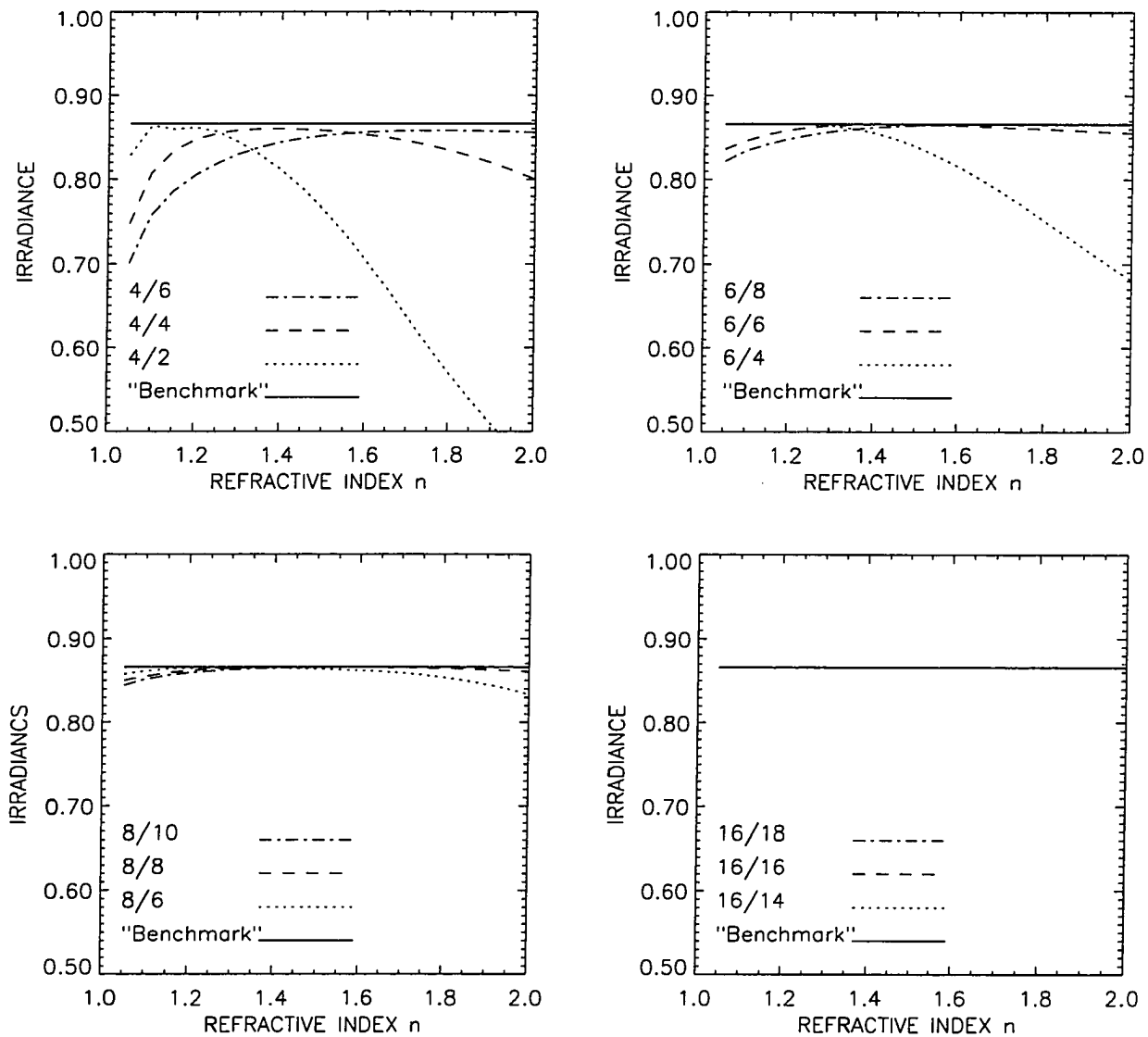
Figure 2.4 The effect of 'stream' combinations within the refractive region and the total reflective region (represented by the number ratio) on the convergence for the Henyey-Greenstein scattering phase function with asymmetry factor $g = 0.7$. Other input parameters are the same as those for the conservative case in Figure 2.3. Shown in the panels are the upward irradiances at the top of the slabs and their comparison with the "Benchmark" irradiance incident on the system .
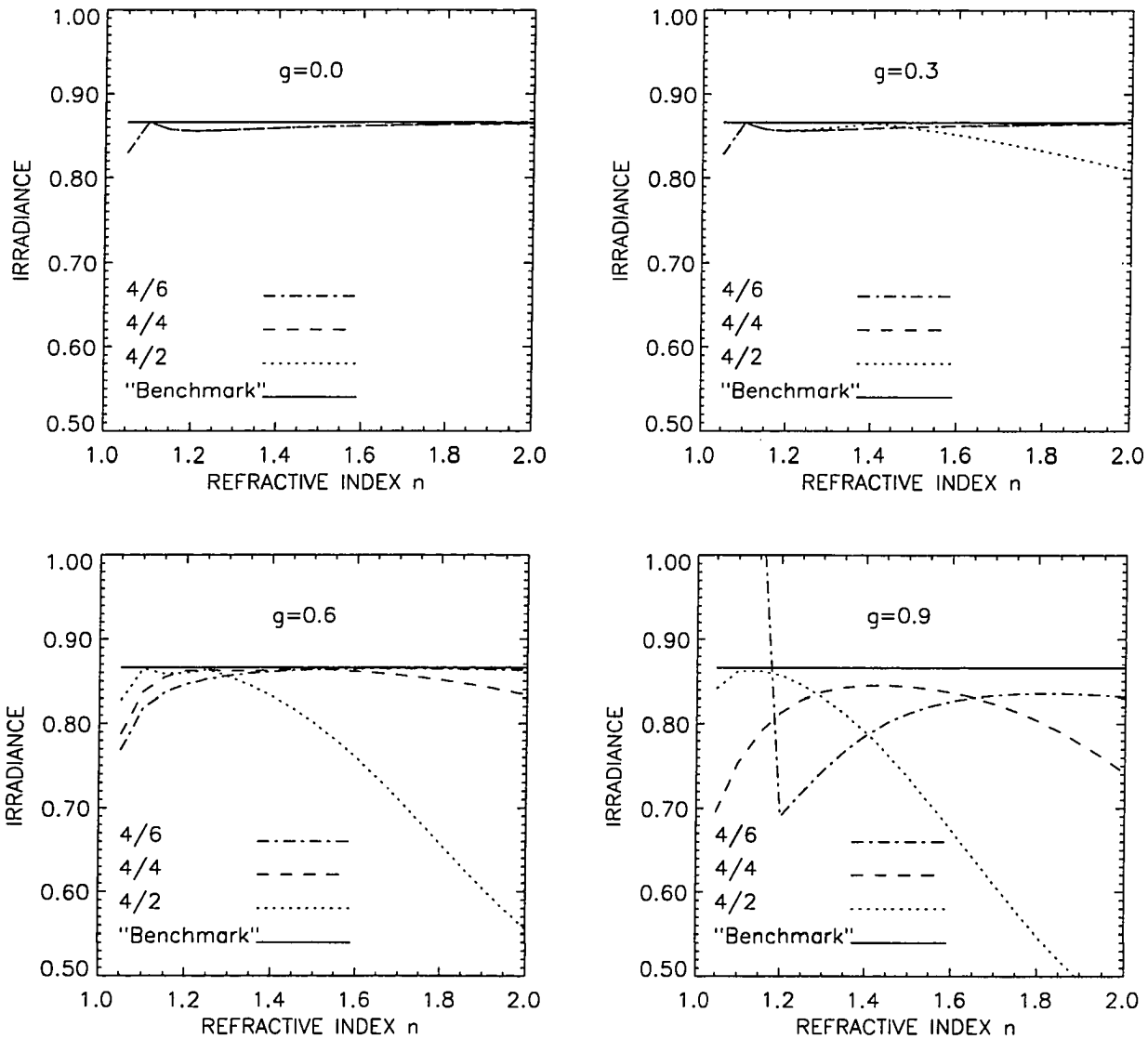
Figure 2.5 Similar to Figure 2.4, but shows the effect of scattering asymmetry on irradiance computation and only for one group of 'stream' combinations .

n should be $\frac{N_2}{N_1} \simeq n^2$, but this has not been proven mathematically.

In addition to the distribution of quadrature points between the two regions, the convergence is also strongly dependent on the asymmetry of the phase function. For the Henyey-Greenstein phase function which depends only on the asymmetry factor g, Figure 2.5 shows that for smaller asymmetry factors (i. e. less anisotropy), fewer quadrature points are needed to attain good accuracy. We have adopted the delta-M transformation [Wiscombe, 1977], which has been shown to optimize the performance of the model and to improve the accuracy in flux computation for strongly forward peaked scattering.

2.3 Examples of Application in the Atmosphere-Ocean System

In this section the coupled radiative transfer model described above will be applied to the atmosphere-ocean system for a number of simplified examples. The profiles of pressure, gas concentrations and temperature are taken from the McClatchey [1972] model atmosphere for mid-latitude summer and the atmosphere is divided into 24 layers. For simplicity, only clear atmosphere and pure sea water are considered here. Therefore, we may adopt the Rayleigh scattering phase function both for the atmosphere and the ocean. The optical properties of seawater are taken from Smith and Baker [1981]. Because of the homogeneity of pure sea water, it is not necessary to use multiple layers in the ocean even though the model can easily accommodate an arbitrary number of layers in the ocean. The first example shows the computed downward irradiances at the top of atmosphere and at several depths in the ocean as illustrated in Figure 2.6. Here the solar zenith angle is specified to be 30° and the relative refractive index for the ocean is specified to
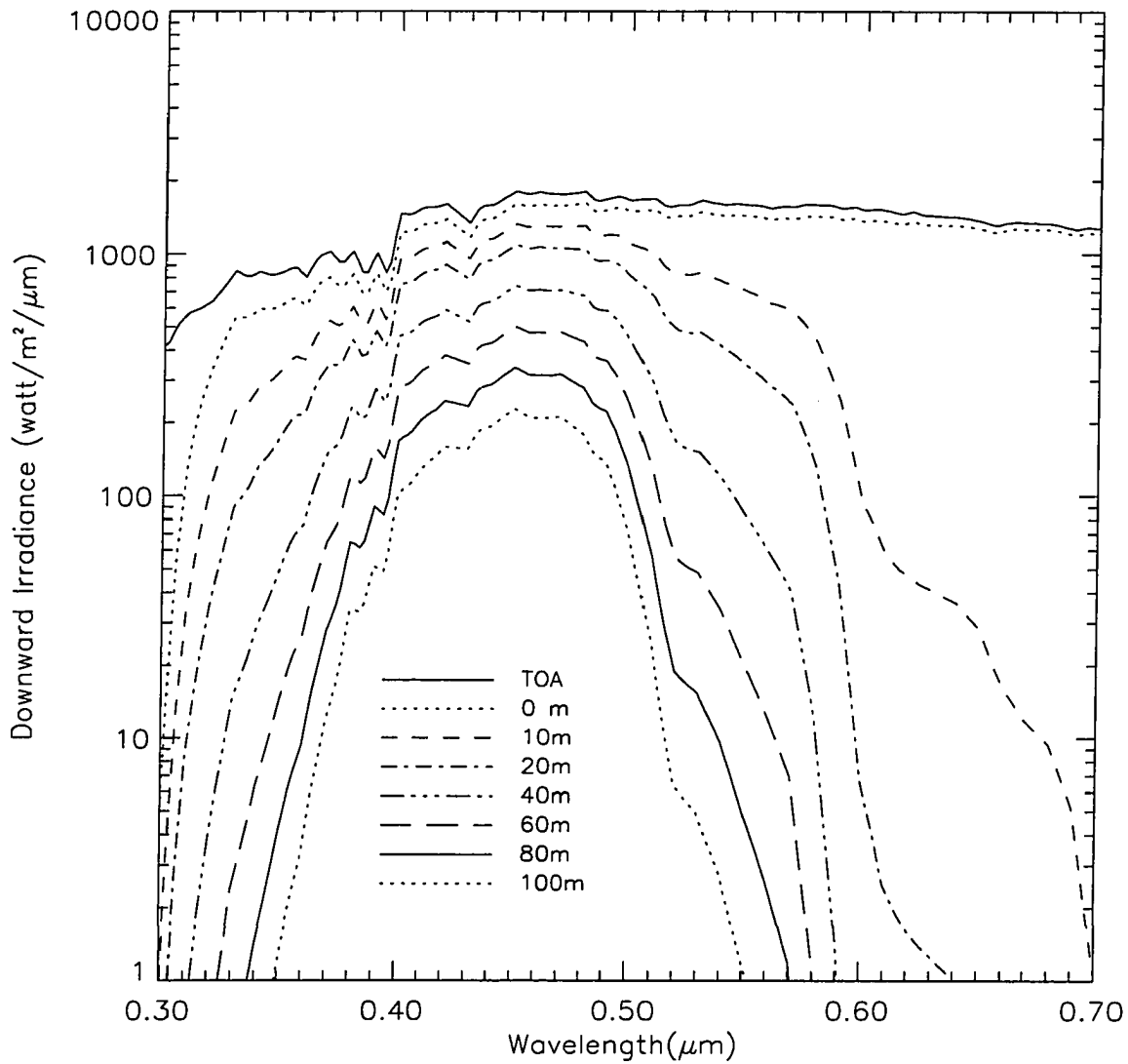
Figure 2.6 Spectral distributions of downward irradiances at the top of the atmosphere, and at several depths in the ocean for a clear mid-latitude atmosphere and a pure sea water model assuming a solar zenith angle $\theta_0 = 30^0$.

be 1.33 (neglecting for simplicity the small wavelength dependence here). This Figure shows that the atennuation of light in the ocean is strongly dependent on the wavelength.

Next in Figure 2.7 we show the computed reflectance of the ocean surface for several solar zenith angles and compare it with the results obtained when the effects of refraction are ignored. The difference in the upward and downward irradiances at the ocean surface between including and neglecting refraction is also shown. The results indicate that underestimation of the reflectance would occur for most wavelengths if the change in index of refraction across the interface between the ocean and the atmosphere is ignored. As the solar zenith angle increases, the specular reflection, caused by the difference in the indices of refraction between the atmosphere and the ocean, contributes more to the total reflectance of the ocean surface, and consequently more to the upward irradiance at the ocean surface. Therefore, for larger solar zenith angles the discrepancy between the reflectances computed with and without refraction becomes larger.

Figure 2.8 shows the distribution of downward irradiance and upward irradiance with height in the atmosphere and depth in ocean for the same atmosphere and ocean model used above at wavelength of 500 nm. For comparison, corresponding results obtained by neglecting refraction are also displayed. There is considerable interest in the energy absorption as a function of altitude in the atmosphere or depth in the ocean, because this absorbed energy drives the atmospheric and oceanic circulation. Because the absorbed energy within each layer is proportional to the mean intensity (same as the total scalar irradiance defined by Morel and Smith [1982] divided by 4π), we show in Figure 2.9 the mean intensity versus height in the atmosphere and versus depth in the ocean. Also shown are the same results obtained by ignoring refraction and the relative error, $|(I_{refr.} - I_{norefr.})/I_{refr.}| \times 100$. We note that the relative error may be as large as 20% just below the ocean sur-
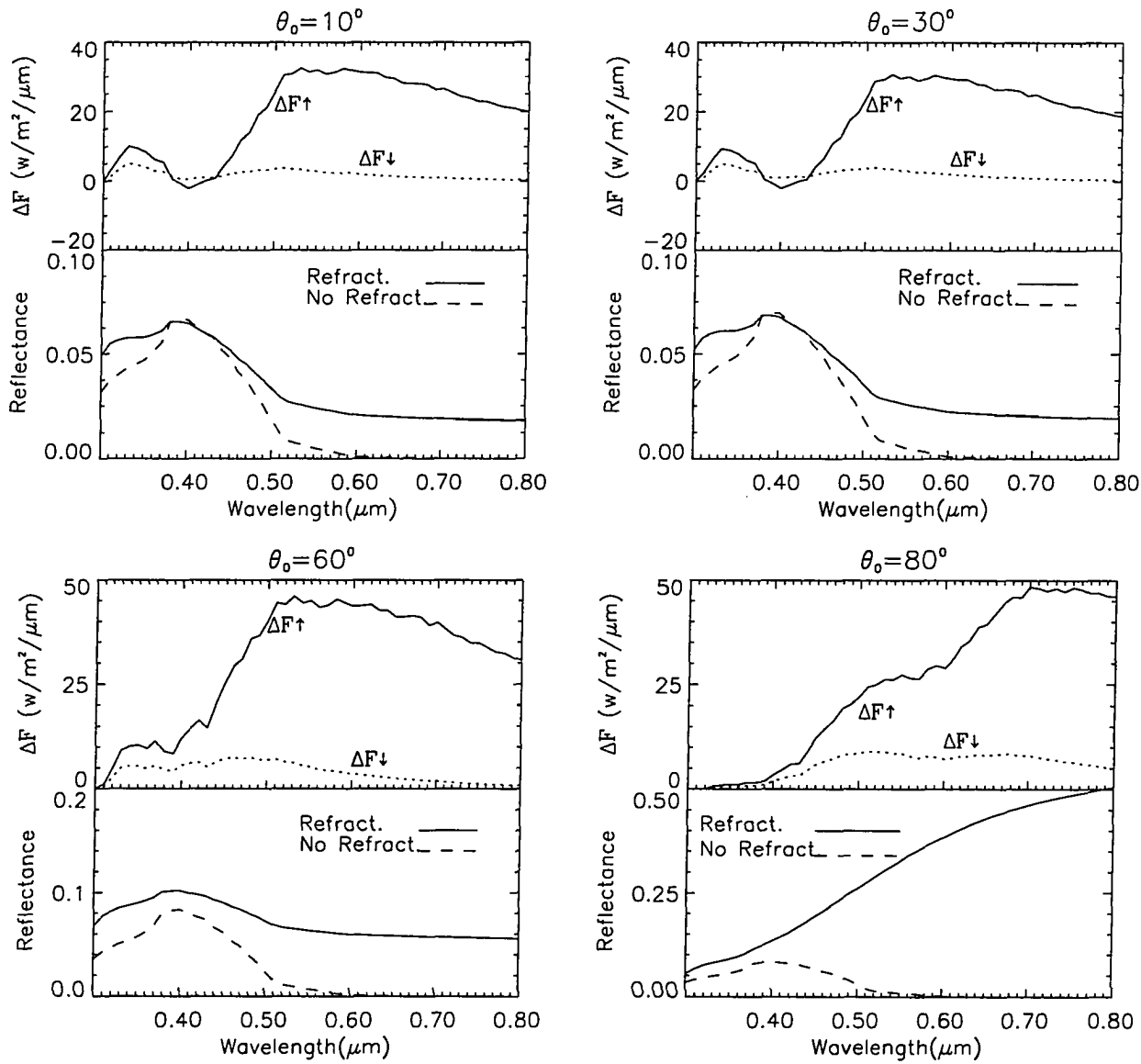
Figure 2.7 Spectral distribution of ocean surface reflectance for considering refraction and neglecting refraction and for several solar zenith angles. Also shown are the downward and upward irradiance differences at the ocean surface between considering and neglecting refraction, $\Delta F_{\downarrow} = F_{Refr.\downarrow} - F_{Noref.\downarrow}$, $\Delta F_{\uparrow} = F_{Refr.\uparrow} - F_{Noref.\uparrow}$. The same atmosphere and ocean models as in Figure 2.6 are used.
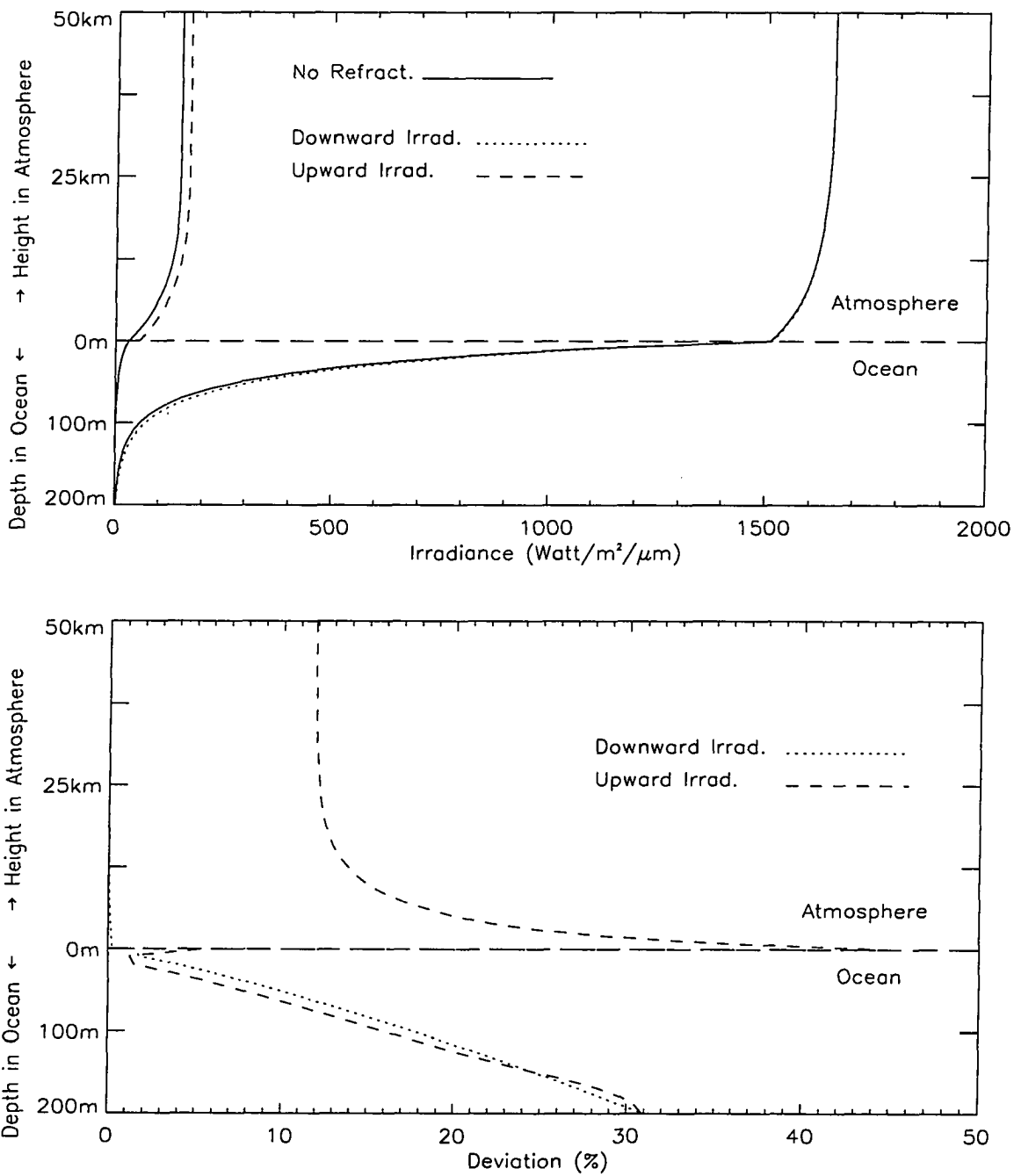
Figure 2.8 Distributions of the downward and the upward irradiances with height in the atmosphere and with depth in the ocean as well as the results of neglecting refraction and their relative deviation. $\theta_0 = 30°$, $\lambda = 500nm$.

face. Although the error is large in the deep ocean, the radiation field is already significantly attenuated there.

Figure 2.10 shows the azimuthally-averaged radiance distribution just above and just below the ocean interface. Again results obtained by ignoring refraction are also displayed. The results indicate that refraction significantly alters the radiance distribution. Just below the ocean surface, the downward radiance discontinuity position shifts from the horizontal direction for the case of no refraction to the critical angle direction when refraction is included. The refraction also significantly changes the upward radiation field just above the ocean surface. Knowledge of the radiance distribution here is particularly important for correct interpretations of intensity measurements in remote sensing applications.

All the quantities computed above (Figures 2.6 to 2.10) are accurate to within 1%. To obtain this accuracy, a stream ratio of 6/10 (6 streams in the atmosphere, 10 streams in the ocean) was applied in these calculations, while a ratio of 40/70 is used for Figure 2.10 but only for the purpose of obtaining enough points to plot a smoother curve.

2.4 Comparison With Other Models for Underwater Light Computations

The present model has recently been compared with six other models which approached the radiative transfer problem in the atmosphere-ocean system with different methods [*Mobley et al.*, 1993]. These include five Monte Carlo models and a model using an invariant imbedding technique. Several canonical (standard) problems of different complexities were defined for the comparison of results produced by these radiative transfer models. Models claiming to incorporate the air-water
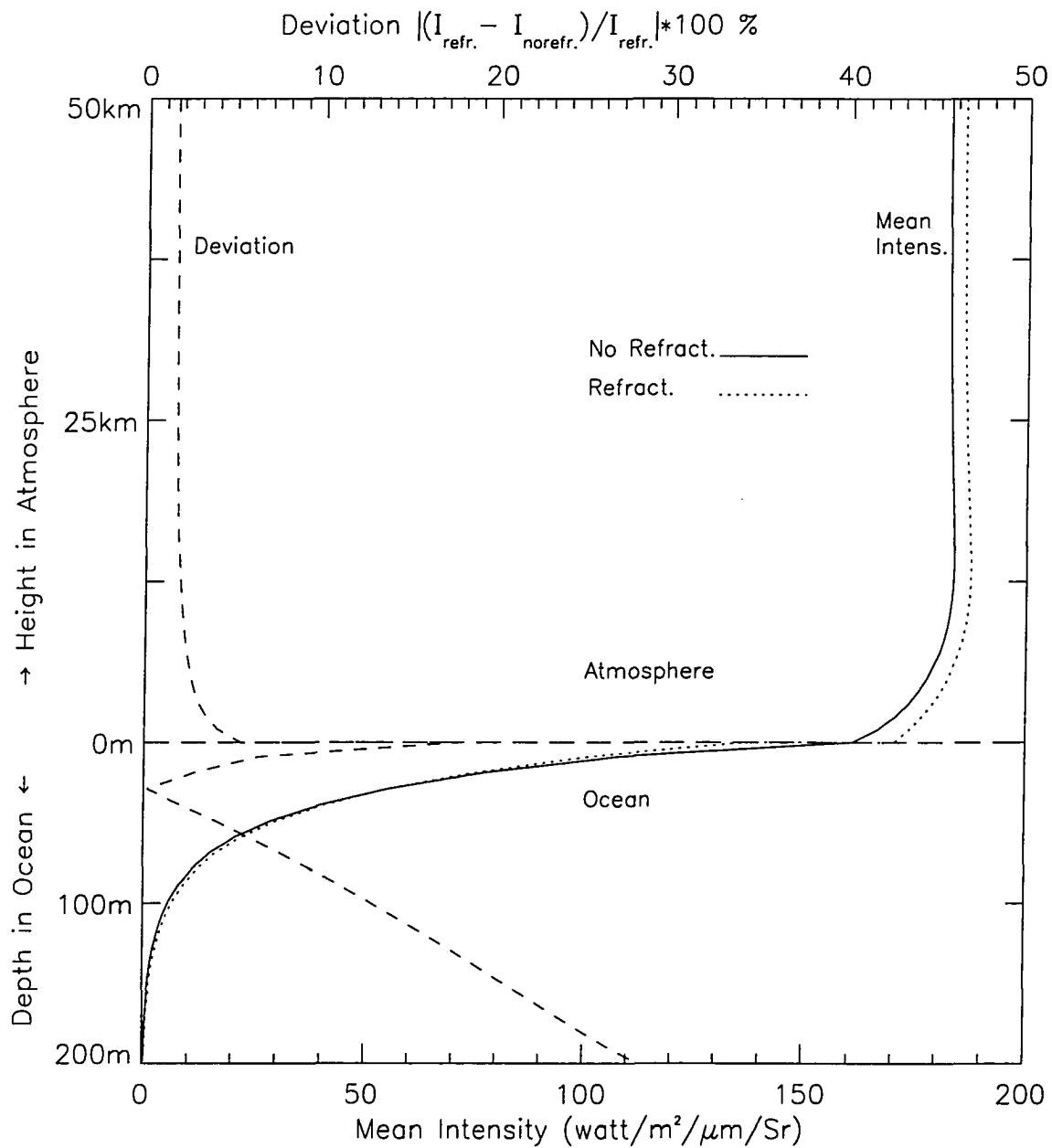
Figure 2.9 Distribution of the total mean intensity (total scalar irradiance/4π) with height in the atmosphere and depth in the ocean as well as the result of neglecting refraction and its relative deviation. $\theta_0 = 30^\circ$, $\lambda = 500nm$.
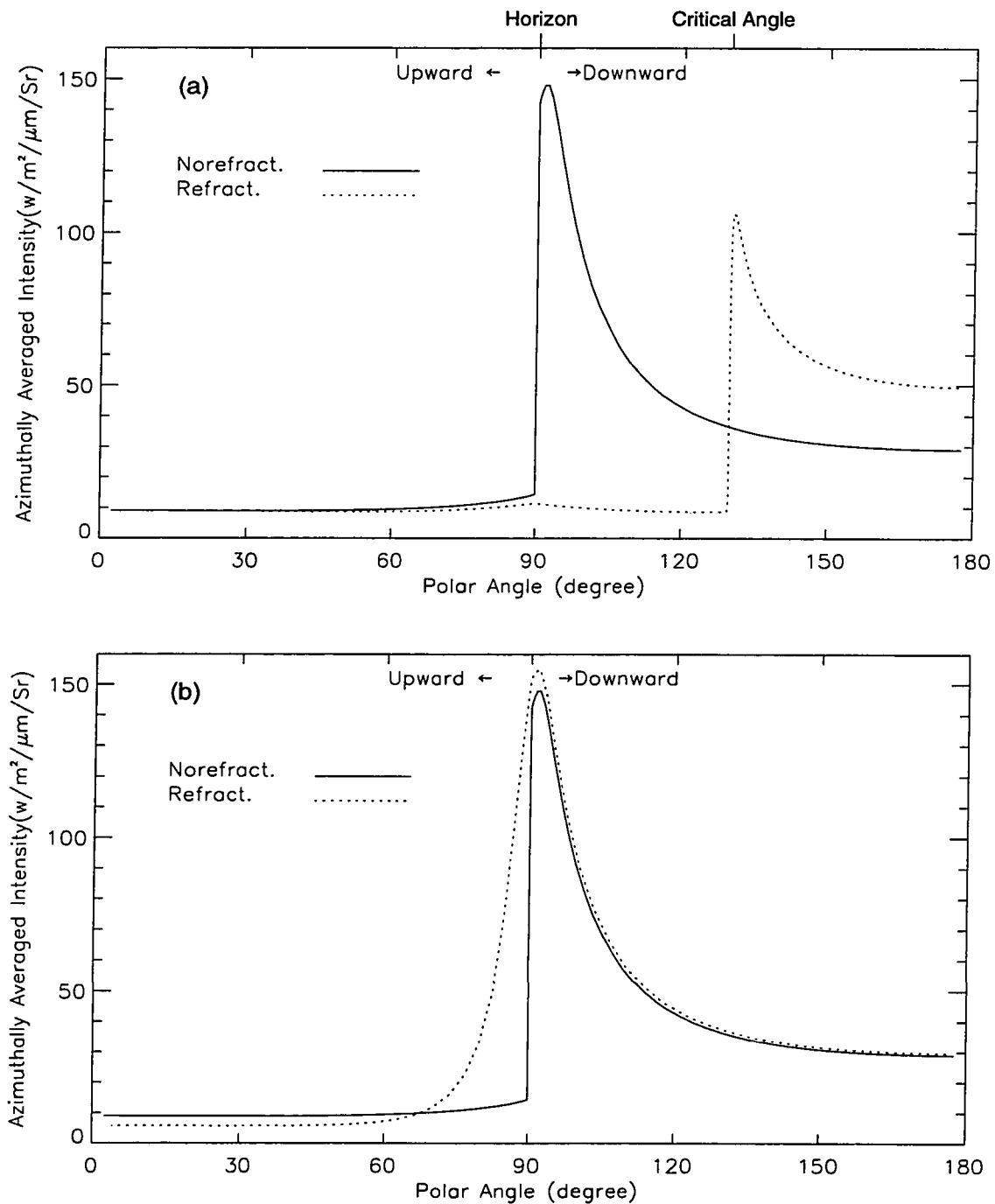
Figure 2.10 Distributions of the azimuthally-averaged intensity (radiance) for the refractive case ($n = 1.33$) and the non-refractive case ($n = 1.0$). $\theta_0 = 30^0$, $\lambda = 500nm$. (a) Just below the ocean surface; (b) Just above the ocean surface .

boundary correctly and to provide realistic simulations of the oceanic optical environment should be able to solve these problems with acceptable accuracy. The comparison included not only irradiances and radiances, but also the execution time for different problems. The problems defined for comparison cover the extreme range of oceanic inherent optical properties: single scattering albedo (a) from 0.2 to 0.9, representing a highly absorbing case and a highly scattering case; phase functions for pure Rayleigh and pure particulate scattering; and the presence of strong vertical stratification in the ocean. A typical oceanic phase function with strongly forward-peaked scattering was adopted for particulate scattering. The detailed specification of these canonical problems was given in the paper by Mobley et al. [1993]. Briefly, problem 1 is an unrealistically simple problem, where only the Rayleigh scattering is considered; problem 2 used realistic optical properties for seawater and was designed to test the models' abilities to handle realistic phase functions under both highly scattering and highly absorbing cases; problem 3 is designed to test the models' abilities to compute light fields in highly stratified water with vertically varying hydrosol (chlorophyll) concentration distributions; problem 4 considers atmospheric effects; problem 5 consider the effects of a wind-roughened sea surface; and problem 6 imposes a finite-depth bottom. Because the detailed comparison results were demonstrated in the figures and tables in Mobley et al. [1993], they will not be repeated here. Instead, I will present the average values from all the models and compare them with those from our model for some of the problems to illustrate the performance of our model. The results are shown in Table 2.1, here F^- and E_{od} are the downward irradiance and the upward scalar irradiances respectively, as defined in (2.19) and (2.22), and I_u represents the nadir-viewing radiance as seen by a sensor pointed straight down.

The radiance distribution at selected ocean depths for problem 2 was also compared. Figure 2.11 shows the results of radiance distribution in the plane of the

Table 2.1 Average Values of F^-, E_{ou} and I_u Computed by Different Models at Selected Depths for the Problems Defined in Mobley et al. [1993] and Comparisons With Values From the Present Model .

Optical Depth	Average Value			Value From DOM			Difference (%)		
	F^-	E_{ou}	I_u	F^-	E_{ou}	I_u	F^-	E_{ou}	I_u
Problem 1, a=0.9 (N=7)									
1	3.66-1	3.72-1	4.85-2	3.66-1	3.73-1	4.88-2	0.0	0.3	0.6
5	4.33-2	4.35-2	5.59-3	4.33-2	4.35-3	5.79-3	0.0	0.0	3.6
10	3.16-3	3.20-3	4.37-4	3.15-3	3.16-3	4.21-4	0.3	1.3	3.7
Problem 1, a=0.2 (N=7)									
1	1.41-1	1.34-2	1.72-3	1.42-1	1.34-2	1.71-3	0.4	0.0	0.6
5	1.07-3	1.00-4	1.37-5	1.07-3	9.92-5	1.30-5	0.0	0.8	5.1
10	2.93-6	3.00-7	3.39-8	3.03-5	2.70-7	3.75-8	3.4	10.0	10.6
Problem 2, a=0.9 (N=7)									
1	4.13-1	9.31-2	6.99-3	4.14-1	9.41-2	6.89-3	0.2	1.1	1.4
5	1.87-1	4.63-2	3.26-3	1.87-1	4.66-2	3.13-3	0.0	0.7	3.9
10	6.85-2	1.65-2	1.21-3	6.85-2	1.65-2	1.14-3	0.0	0.0	5.8
Problem 2, a=0.2 (N=7)									
1	1.62-1	9.66-4	5.47-5	1.62-1	9.72-4	5.76-5	0.0	0.6	5.3
5	2.27-3	1.37-5	6.24-7	2.28-3	1.35-4	7.96-7	0.4	1.5	27.6
10	1.30-5	7.28-8	4.02-9	1.31-5	7.01-8	4.54-9	0.8	3.7	12.9
Problem 3 (N=6)									
5 m	2.30-1	4.34-2	3.13-3	2.30-1	4.40-2	3.02-3	0.0	1.4	3.5
25 m	1.62-3	2.86-4	2.12-5	1.63-3	2.92-4	2.01-5	0.6	2.1	5.2
60 m	5.23-5	5.13-6	3.57-7	5.12-5	5.12-6	4.24-7	2.1	0.2	18.8
Problem 6 (N=3)									
1	1.62-1	9.81-4	6.84-5	1.62-1	9.93-4	6.94-5	0.0	1.2	1.5
5	2.28-3	2.28-3	3.60-4	2.28-3	2.28-3	3.63-4	0.0	0.0	0.8

N is the number of models included in the averages. The notation 3.66-1, for example, means 3.66×10^{-1}.

sun at depths of $\tau{=}0$, 5, and 20 in the ocean for problem 2. Where the solid lines represent the results from our model, and the dashed lines represent the average of all the other models. The data set resulting from other models was kindly provided by Mobley [personal communication, 1994]. Direction (θ_v, ϕ_v) in Figure 2.11 gives the viewing direction, i.e., the direction an instrument points to detect photons traveling in the ($\theta = 180^o - \theta_v$, $\phi = 180^o + \phi_v$) direction. Thus, $\theta_v = 180^o$ corresponds to looking straight up and seeing photons heading straight down; the nadir radiance, L_u, of Table 2.1 is the value plotted at $\theta_v = 0^o$. The sun is in the $\phi_v = 0^o$ half-plane.

The large spike in the radiance near (θ_v, ϕ_v)=(140°, 0°) is the refracted solar beam. The noticeable radiance difference and θ_v offset in the position of the plotted peak radiance occurs because all the other models calculate radiance in a grid of quadrilateral regions and choose their quad boundaries differently. The radiance values are plotted at the θ_v values of the quad centers and plotted points are connected by straight lines. Because the present model computes radiances in specific directions, rather than quad-averaged radiances as the other models do, the solid lines show a more pronounced spike in the radiance near the solar direction, and more pronounced changes near the critical angle. The higher angular resolution used in the present model also produces a much narrower peak. The angular quadrature points are clustered near the critical angle and near the horizon, to get increased resolution in regions where the radiance varies rapidly with polar angle.

The computer resources required for each problem were also compared, showing that the present model is especially efficient for the computations of irradiances and azimuthally averaged radiances. Comparison of the asymptotic radiances and the asymptotic diffuse attenuation coefficient were also carried out, and show a very good agreement between the present results with those from other models.

Comparison of Radiance Distribution
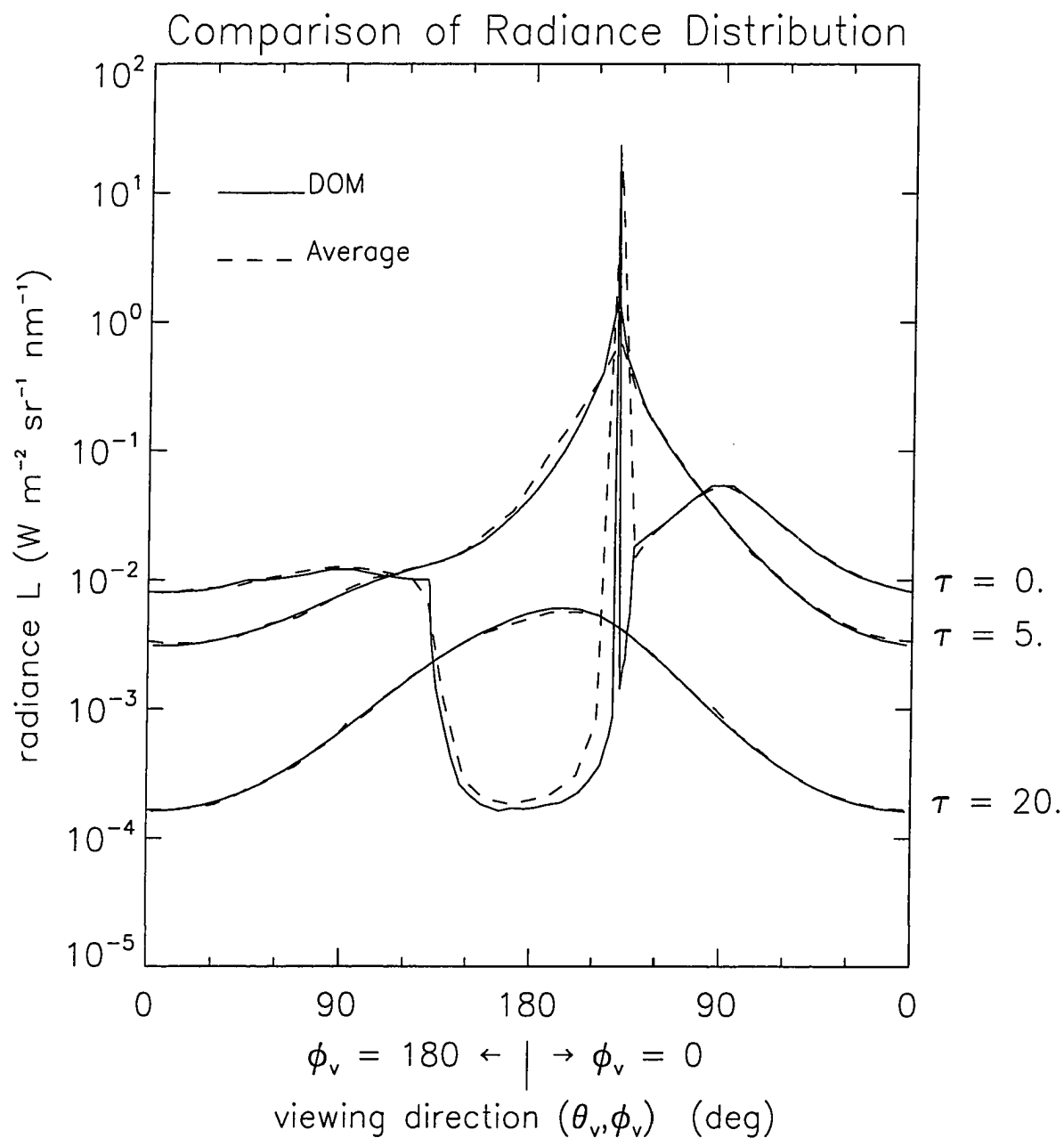
Figure 2.11   Radiance distribution in the plane of the sun for problem 2 in Mobley [1993] and a comparison with the average of the other models. Angles (θ_v, ϕ_v) are viewing directions: $\theta_v = 180° - \theta$ and $\phi_v = 180° + \phi$, where (θ, ϕ) are the directions of photon travel .

These will not be discussed here.

2.5   Summary

A comprehensive methodology has been developed, based on the discrete ordinate method, for solving the radiative transfer equation pertinent to a system consisting of two strata with different indices of refraction. The method is well suited to provide consistent solutions of the radiative transfer problem for the coupled atmosphere-ocean system. The refraction and total reflection at the interface of the two strata have been taken into account by assigning different numbers of angular quadrature points (discrete ordinates or 'streams') in the atmosphere and the ocean. Thus, interpolation at the interface between two media is entirely avoided, and the radiation field both in the atmosphere and the ocean can be efficiently solved simultaneously. The vertical inhomogeneity of the atmosphere and ocean can be accounted for by dividing each stratum into a suitable number of homogeneous layers and considering the optical properties to be constant within each layer but varying from layer to layer.

Test results show that the solution conserves energy and is both reliable and efficient. The accuracy depends on the number of 'streams' utilized to discretize the angular dependence. Good accuracy for irradiance and mean intensity are obtained with just a few 'streams'. Preliminary results obtained from applying these procedures to the atmosphere-ocean system show that refraction significantly affects both the radiation field and the radiative energy absorption in both the atmosphere and ocean. A more realistic quantification of the radiation field in the atmosphere and ocean environment can be simulated when actual optical properties of the atmosphere, including clouds and aerosols, and of the ocean, including particulates versus depth, are available. The radiative transfer model presented

in this chapter provides a means for estimating light reflection, transmission and heating and cooling rates, and for studying the radiative interaction between the atmosphere and the ocean.

Based on the results presented above, we can conclude that the radiative transfer model for the coupled system has correctly incorporated the mathematical representations of the relevant radiative processes (absorption and scattering) and of the effects of the air-water boundary. The solution of the radiative transfer problem in the coupled system is both accurate and reliable.

Chapter 3

Application to the Study of Solar Energy Distribution in the Atmosphere-Sea Ice-Ocean System

Polar sea ice plays an important role in the global climate system. Solar radiation is the dominant energy component controlling the heat and mass balance of sea ice in the polar regions. On the other hand, sea ice is a critical component in controlling the transfer and partitioning of radiation in the entire atmosphere, sea ice and ocean system. To understand the interaction between the atmosphere, sea ice, and ocean, it is necessary to investigate factors that affect the disposition of the solar radiation within this coupled system, such as the amount of the solar radiative energy stored in the interior of the ice, transmitted into the ocean, and

---

[0]This chapter is based on material published as Z. Jin, K. Stamnes, W. Weeks and S.-C. Tsay, The effects of sea ice on the solar energy budget in the atmosphere-sea ice-ocean system: A model study, *J. Geophys. Res., 99*, 25,281-25,294, 1994.

Reproduced with permission of the copyright owner. Further reproduction prohibited without permission.

reflected back to the atmosphere. Because of the unique and important role played by sea ice in the solar energy distribution in the coupled system, it is important that this natural medium receive considerable attention.

Numerous theoretical and experimental studies have been carried out to investigate the absorption and scattering of solar radiation by sea ice [e.g., *Grenfell and Maykut*, 1977; *Grenfell*, 1979, 1991; *Buckley and Trodahl*, 1987] and the penetration of radiation into the ocean [*Perovich and Maykut*, 1990; *Maykut and Grenfell*, 1975]. Studies of the role of solar radiation in the heat and mass balance of sea ice [*Untersteiner*, 1961; *Langleben*, 1966; *Shine and Crane*, 1984] have shown the importance of solar radiative energy on sea ice decay. While the direct effects of the incoming solar radiation on the heat and mass balance of the ice are now well understood and are fairly easy to treat in models, relatively little is known about the quantitative partitioning of the absorbed radiation among the atmosphere, sea ice, and ocean and the effects of the ice state and clouds on this partitioning of energy. In this chapter, I will apply the radiative transfer model described in Chapter 2 to study the radiative transfer process in the coupled atmosphere-sea ice-ocean system and to assess quantitatively how the physical properties of the ice affect the disposition and partitioning of the solar radiative energy within the atmosphere, the sea ice, and the ocean, within the various layers in the ice, and within the system as a whole. The effects of clouds, surface snow cover, and surface melt ponds on the absorption and distribution of solar energy in the coupled system will also be investigated.

3.1 Input Parameterizations

The solution of the radiative transfer equation for non-uniformly refracting media can be directly used for the atmosphere, sea ice and ocean system. Figure 3.1
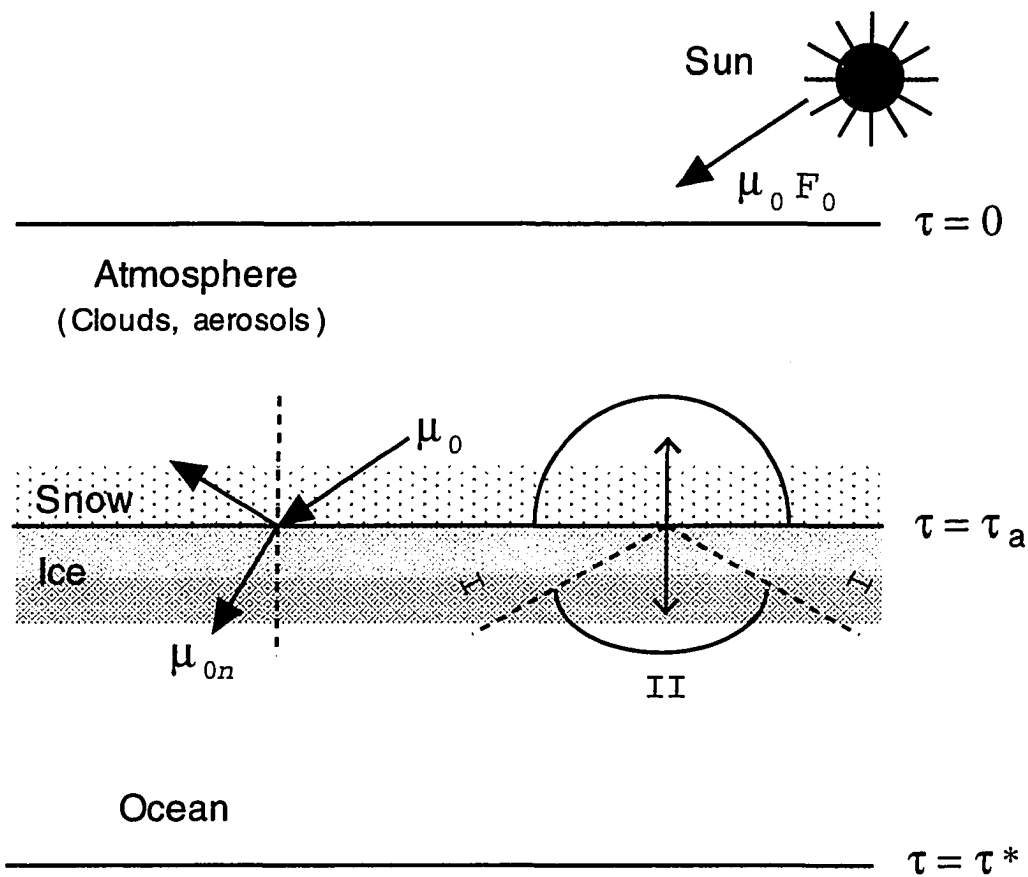
Figure 3.1 Schematic diagram of the coupled radiative transfer model for the atmosphere-sea ice-ocean system.

shows a schematic diagram of radiative transfer in this coupled system. To compute the radiative quantities, we need to specify either the optical properties in every layer or the appropriate physical parameters from which one may derive the optical properties. In addition, we have to specify the bottom and top boundary conditions. The bottom boundary condition refers to the reflecting property of the bottom surface, i.e., the seafloor. As most areas of the polar oceans can be considered optically infinite in depth, the bottom boundary is not particularly important in this study, and assuming it to be a Lambertian surface with any assumed albedo is sufficient. The top boundary condition required is the incident solar spectrum and the solar elevation. The observational data describing the solar spectrum at the top of the atmosphere used here is from *Coulson* [1975].

3.1.1 Optical Properties for Atmosphere, Clouds, Snow and Ocean

Within the atmosphere we consider the absorption and scattering by atmospheric gases, clouds, and aerosols [*Tsay et al.*, 1989]. Although molecular (Rayleigh) scattering is dominated by nitrogen and oxygen gases which constitute more than 99% of the Earth's atmosphere, molecular absorption is dominated by trace gases, mainly water vapor, carbon dioxide, and ozone. The absorption by other minor trace gases is not considered in this study. To account for the total solar energy, one must integrate over the entire solar spectrum, a spectral region where numerous absorption lines of atmospheric gases exist [*Rothman et al.*, 1987]. As a result, incorporation of the line structures into a multiple-scattering radiative transfer code will result in a very time consuming computation. To maximize computational efficiency, parameterization of gaseous absorption over a spectral region containing many lines is necessary when absorption is included in a multiple-scattering

scheme. Therefore the method called exponential-sum fitting of transmissions (ESFT) has been adopted.

The ESFT method approximates the transmission function of a given spectral region by a finite sum of M exponential terms as follows [*Hunt and Grant*, 1969; *Wiscombe and Evans*, 1977]:

$$T(u) = \sum_{i=1}^{M} w_i \exp(-b_i u) \tag{3.1}$$

where T represents the band transmission function and u denotes the equivalent absorber amount. The b_i are the equivalent absorption coefficients and the w_i are the associated weights. The $b_i u$ behave like monochromatic optical depths which can easily be incorporated into the multiple-scattering scheme. The main virtue of the ESFT method is that it reduces the nongray radiative transfer problem involving integration over a finite spectral interval (for which Beer's law does not apply) to a series of monochromatic problems. Also, the overlap of absorbing gases can be easily treated due to the multiplicative property of the transmission [*Goody and Yung*, 1989].

The optical properties of Arctic clouds are parameterized in terms of the equivalent radius RE and the liquid water content LWC of the cloud as follows [*Slingo*, 1989; *Tsay et al.*, 1989]:

$$a = c_1 + c_2 RE \tag{3.2a}$$

$$g = c_3 + c_4 RE \tag{3.2b}$$

$$\beta_{ext}/LWC = c_5 + c_6/RE \tag{3.2c}$$

where a, g, and β_{ext} are the single-scattering albedo, the asymmetry factor of scattering, and the extinction coefficient respectively. The c_i terms are parameterized coefficients determined from numerical fitting of these equations to the optical properties obtained by Mie computations [*Tsay et al.*, 1989]. Although

a more accurate parameterization of the optical properties of clouds is available [*Hu and Stamnes*, 1993], the simpler parameterization used here is believed to be adequate for the small equivalent droplet radii prevailing in the Arctic.

The optical properties of snow, including possible soot contamination, are also obtained through Mie computations, which require the refractive index of ice/soot and the mean radius of snow and soot particles as input. Here we have utilized the models of *Wiscombe and Warren* [1980] and *Warren and Wiscombe* [1980], whose results for computed snow albedo agree well with the available field measurements.

In the ocean, scattering and absorption coefficients of seawater are taken from *Smith and Baker* [1981], who provide values applicable to the 0.2 μm to 0.8 μm region. For wavelengths larger than 0.8 μm, only absorption is considered, because the scattering is weak and the absorption is strong. We also neglect particulates in the ocean in this study, because of their minor effect on the energy budget in the coupled system.

3.1.2 Optical Properties for Sea Ice

In sea ice the processes considered include the absorption by pure ice, scattering and absorption by brine pockets, air bubbles and solid salts trapped within the ice as described by *Grenfell* [1983, 1991]. To obtain the optical properties for bulk sea ice, the relative amounts of each component in the ice have to be determined. Based on the work by *Cox* and *Weeks* [1983], the brine volume fraction (V_{br}), the air volume fraction (V_{bu}), and the solid salt volume fraction (V_{ss}) can be related to the ice salinity (S), temperature (T), bulk density (ρ), brine density (ρ_b) and pure ice density (ρ_i) due to the phase equilibrium constraints. The following formulas, which are applicable from -2°C to -30°C [*Cox* and *Weeks*, 1983] are used in this

study:

$$V_{br} = \rho S / F_1(T) \tag{3.3a}$$

$$V_{bu} = 1 - \frac{\rho}{\rho_i} + \rho S F_2(T)/F_1(T) \tag{3.3b}$$

$$V_{ss} = C(T)\rho_b V_{br}/\rho_s. \tag{3.3c}$$

The dependence of brine density ρ_b on the salinity and the pure ice density on the temperature is expressed as

$$\rho_b(Mg/m^3) = 1.0 + 0.0008 S_b(\%_o) \tag{3.4a}$$

$$\rho_i(Mg/m^3) = 0.917 - 1.403 \times 10^{-4} T(^\circ C) \tag{3.4b}$$

The density of solid salt ρ_s is taken to be a constant $1.5 Mg/m^3$. The brine volume is assumed to be zero (completely frozen) below $-30^\circ C$ and the terms $F_1(T)$, $F_2(T)$ and $C(T)$ are parameterized functions of temperature (see Cox and Weeks [1983] for details) that are determined from the phase equilibrium table of Assur [1958] which, in turn, is based on the experimental results of Nelson and Thompson [1954]. The fact that the phase equilibrium table of Assur is in good agreement with experimentally observed brine volumes (at temperatures warmer than -40°C) has been demonstrated by direct comparisons with NMR measurements of the relative water content in sea ice [*Richardson* and *Keller*, 1966]. The advantage of the Cox and Weeks equations is that they are simple to utilize in a computational model such as that employed in the present study. However the results are identical to results obtained earlier by Anderson [1958] and, in principle, similar to an approach used even earlier by Zubov [1945].

The absorption coefficient for pure ice is based on the data sets reported by *Grenfell and Perovich* [1981] and *Warren* [1984]. The optical properties of the brine pockets, air bubbles, and solid salts are obtained from Mie calculations with assumed spherical shapes. Unfortunately, field observations on size distributions

for these inclusions are few. Therefore we have assumed values that appear reasonable. The size distribution for air bubbles is represented by a power law [*Grenfell, 1983*]

$$N(r) = N_0 r^{-1.24} \qquad (3.5)$$

where the upper and lower limits of 2 mm and 0.1 mm were used. The constant N_0 can be derived from the integration of the air volume over the size distribution together with the Cox and Weeks equation (3.3b). The solid salts are assumed to be monodisperse with radii of 10 μm. As might be expected, the solid salt contribution only becomes significant at ice temperatures below the crystallization temperature of NaCl$\cdot$2H$_2$O (-22.9°C). Only one measurement on the size distribution of brine pockets has been reported by *Perovich and Gow* [1991] for young sea ice, but the lower and upper size limits and their relation with salinity and temperature were unknown. *Grenfell* [1991] assumed a constant number concentration of 10 per cubic millimeter and a monodisperse distribution. As this assumption could overestimate brine scattering if the salinity is low, we will assume a uniform size distribution with a number concentration of $0.6S$ per cubic millimeter (S is the salinity in per mil) to coincide with the observational brine pocket size (typically tenths of a millimeter). This size distribution also causes the rate of change of the radius with temperature to approximately agree with the correlation length change with temperature observed by Perovich and Gow [1991]. As ice warms, the size distribution used here permits growth in the size of the brine pockets but ignores the merging of brine inclusions, which may decrease the scattering. Owing to the large particle size and the anomalous scattering resulting from the similarity in the refractive indices of ice and brine, the phase functions of brine pockets always show an extremely strong forward scattering peak. Therefore most of the scattered light is concentrated in a very small cone around the forward direction and can be added back to the incident radiation, so that the actual scattering coefficient can be

scaled down dramatically. In addition, although an increase in brine pocket size will increase the extinction and scattering coefficients, this change will also strengthen the forward scattering, which actually reduces the scattering effectiveness. These factors make the error in radiation computation resulting from the uncertainty in brine size distribution much smaller than might be expected. As a example, Figure 3.2 shows the scattering phase functions computed at a wavelength of 500 nm for three different brine size distributions. Because the size of the brine inclusions is much larger than the wavelength, the phase function shows little variation as the brine size distribution changes.

Each component in the sea ice interacts differently with radiation. Pure ice acts mainly as an absorber. Although air bubbles and brine pockets both scatter light strongly, air bubbles scatter more effectively, while brine pockets also absorb radiation. The optical properties of the sea ice depend on the volume occupied by each component. Relations represented by Eq. (3.3a) and Eq. (3.3b) are plotted in Figure 3.3, which shows that the fractional volume of air is sensitive to bulk ice density, but not to ice salinity, while the fractional volume of brine is sensitive to the ice salinity and temperature, but not to the ice density. Therefore, when the air volume instead of ice density is the directly available input parameter, the brine volume calculated from Eq. (3.3a) based on an approximated density should still be accurate enough.

3.2 The Radiative Energy Budget in the Atmosphere, Sea Ice and Ocean System

For solar radiation the spectral region considered here is from 0.25 μm to 4.0 μm, which includes approximately 99% of the total solar radiation energy incident at
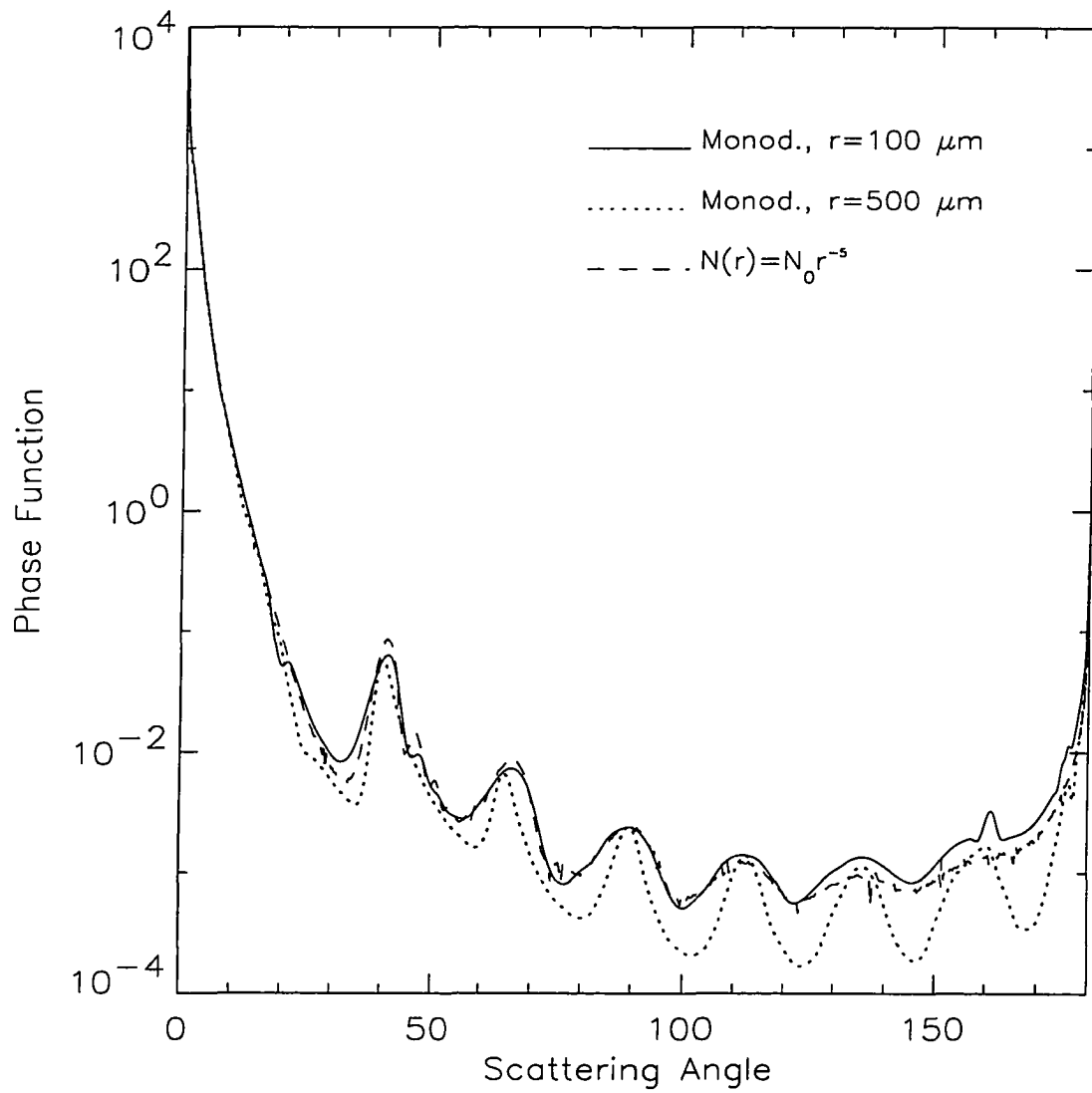
Figure 3.2 Phase function of brine pockets for three different size distributions, (i) monodisperse with radius of 0.1 mm; (ii) monodisperse with radius of 0.5 mm; (iii) power law distribution with lower and upper limits of 0.1 mm and 3 mm. Wavelength for these examples is 500 nm .

Fraction Volume of Brine and Air as a Function of Ice Density and Salinity
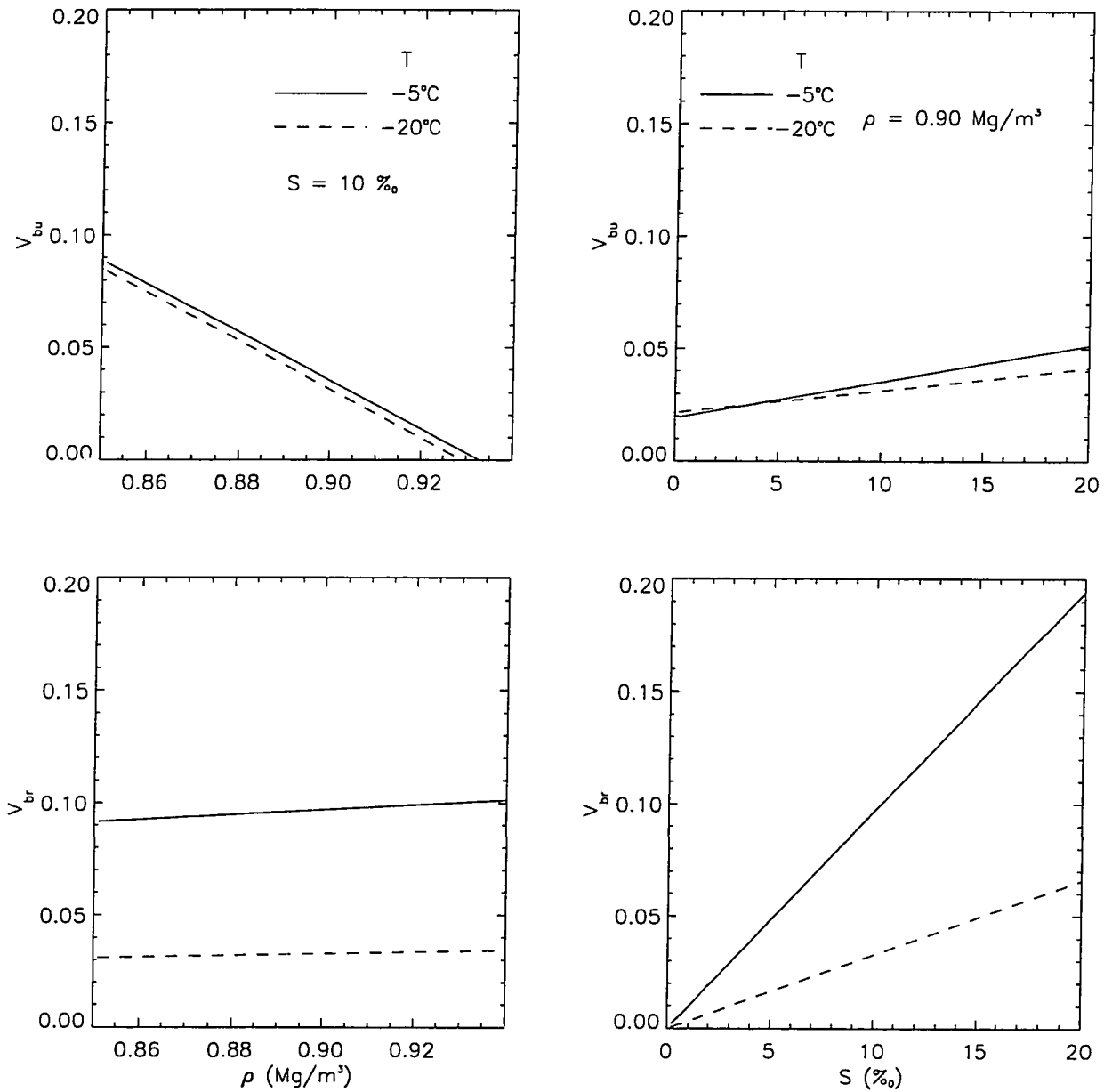
Figure 3.3 Fraction volumes of brine and air in sea ice as a function of ice density and salinity .

the top of the atmosphere. In this study the solar spectrum is divided into 24 bands and the ESFT method described earlier is adopted to simulate the absorption by water vapor, carbon dioxide, oxygen, and ozone in each band. For test purposes we have taken the profiles of pressure, gaseous concentrations in the atmosphere from the *McClatchey et al.* [1972] model atmosphere for the sub-arctic summer and divided the atmosphere into 25 layers. These profiles of atmospheric properties are shown in Figure 3.4. For sea ice, although modeled salinity profiles are available [*Cox and Weeks*, 1988; *Eicken*, 1992], an adequate treatment of density profile variations does not exist. Therefore, we will, as a first approximation, assume that although the density and salinity may change with thickness, for a given thickness these values are constant throughout the ice sheet. We will also assume that there is a linear temperature profile with the bottom temperature of the ice fixed at $-2°C$. Although this is known to be an excellent approximation for young ice types, as sea ice thickens non-linear effects become increasingly common [*Maykut*, 1978]. The ice is divided into three to seven layers in the following studies, depending on ice properties. In the ocean we will neglect vertical variations in the properties of seawater and consider it as one homogeneous layer.

3.2.1 Spectral Radiative Absorption

The first test is for ice with thickness 3.0 m, salinity $3\%_{00}$, density 0.90 Mg/m^3 and surface temperature $-10°C$, approximately the ice surface temperature in the middle of May and September observed in the central Arctic [*Maykut*, 1978]. For this ice model, which can be considered to be representative of multiyear ice, the single-scattering co-albedo (the ratio of the absorption coefficient and extinction coefficient) in the 24 spectral bands at three depths in the ice is shown in Figure 3.5, which indicates strong absorption in the infrared part of the solar spectrum and
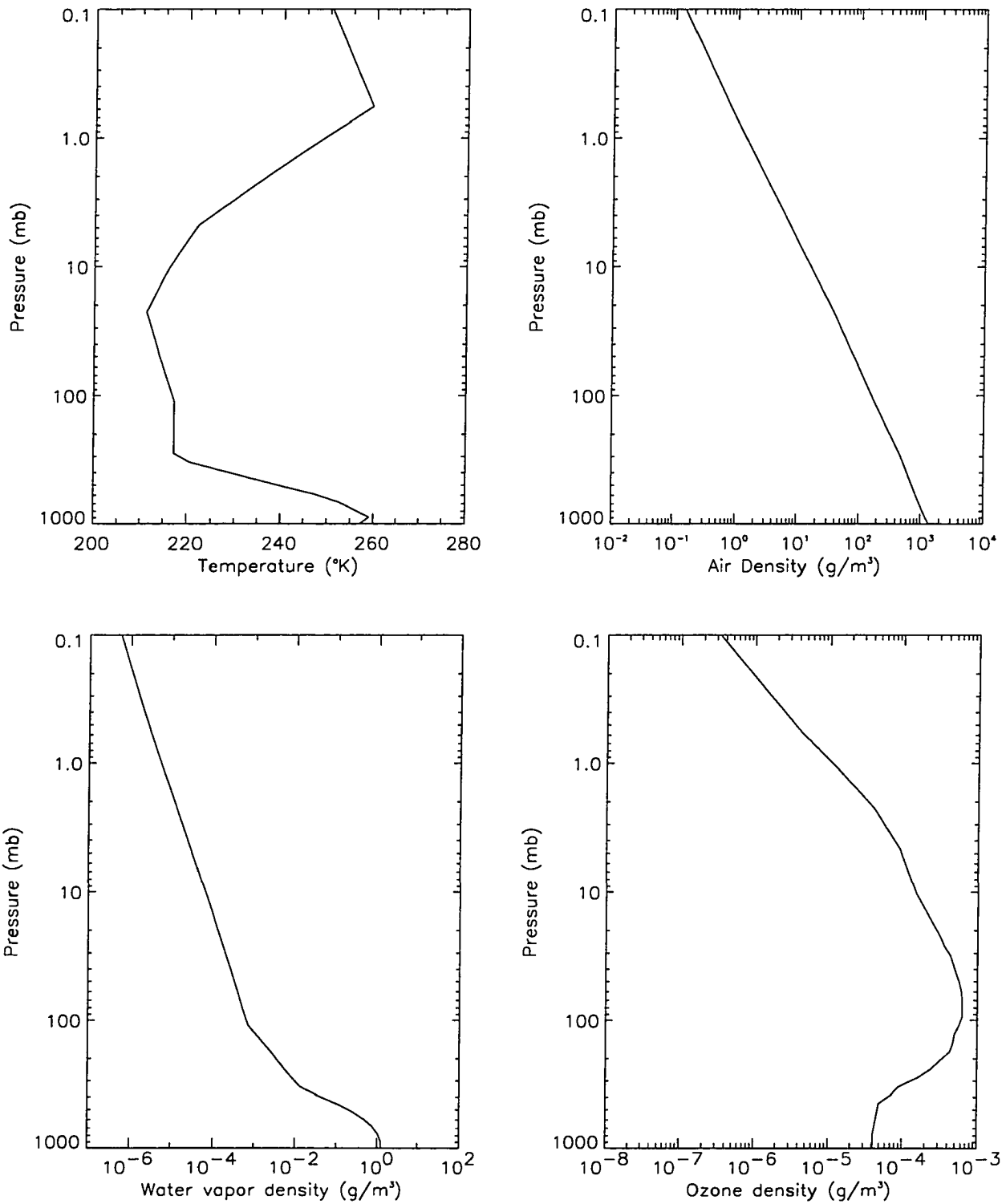
Figure 3.4 Profiles of temperature and gas concentrations as a function of pressure for the McClatchey subarctic summer atmosphere model .

relatively weak absorption in the visible region. Figure 3.6 shows the net fluxes in the 24 spectral bands at various levels and with a solar zenith angle of 60°. The net (downward) flux is defined as the difference between the downward and upward fluxes (irradiances) as given by (2.23). Therefore the vertical distance between any two curves represents the radiation energy absorbed by a column with unit cross-sectional area between the corresponding two levels, and the area beneath the bottom line represents the absorption of radiation by the ocean. Figure 3.6 indicates that much of the solar radiation will be absorbed within the uppermost 0.1 m of the ice and the absorption also varies greatly as a function of wavelength, which is well correlated with the single-scattering co-albedo shown in Figure 3.5. Only the visible radiation can penetrate into the deeper layers of the ice and into the ocean.

For the same conditions as in Figure 3.6 (top) panel, but including a layer of Arctic stratus cloud in the atmosphere, the bottom panel in Figure 3.6 shows that the absorption by the atmosphere is increased, especially at the longer wavelengths, due to the cloud absorption. Consequently, absorption by the ice and by the ocean will decrease in every spectral band, especially in the upper layer of the ice. On the basis of observational data [*Herman and Curry*, 1984; *Tsay and Jayaweera*, 1984], the cloud used here has an equivalent droplet radius of 7 μm and a water content of 0.2 g/m^3. The cloud base is assumed to occur at a height of 700 m with a thickness of 300 m, representative of mean observational values for Arctic stratus.
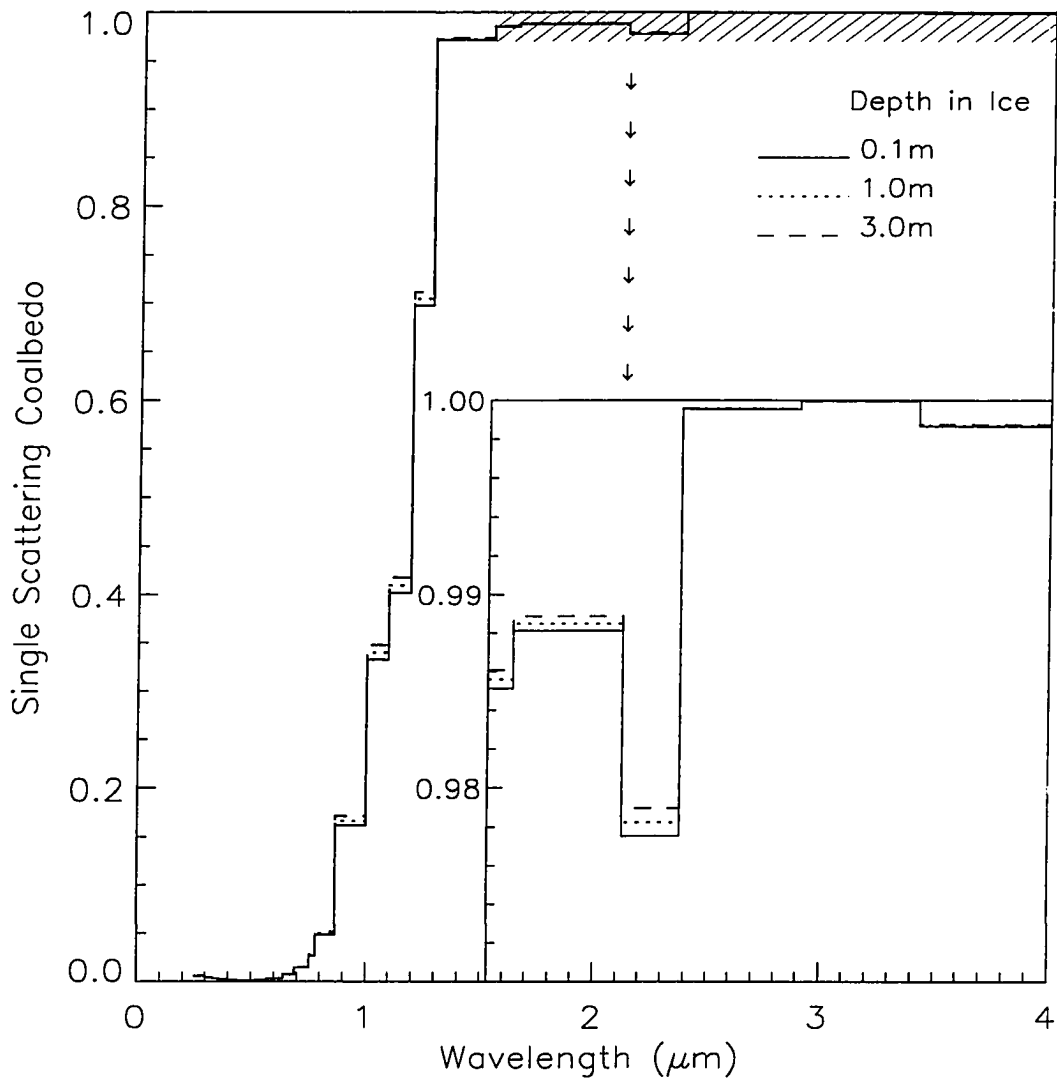
Figure 3.5 The single-scattering co-albedo at three levels for ice with thickness of 3.0 m, density of 0.9 Mg/m^3, salinity of 3%$_{00}$, and surface temperature of -10°C .
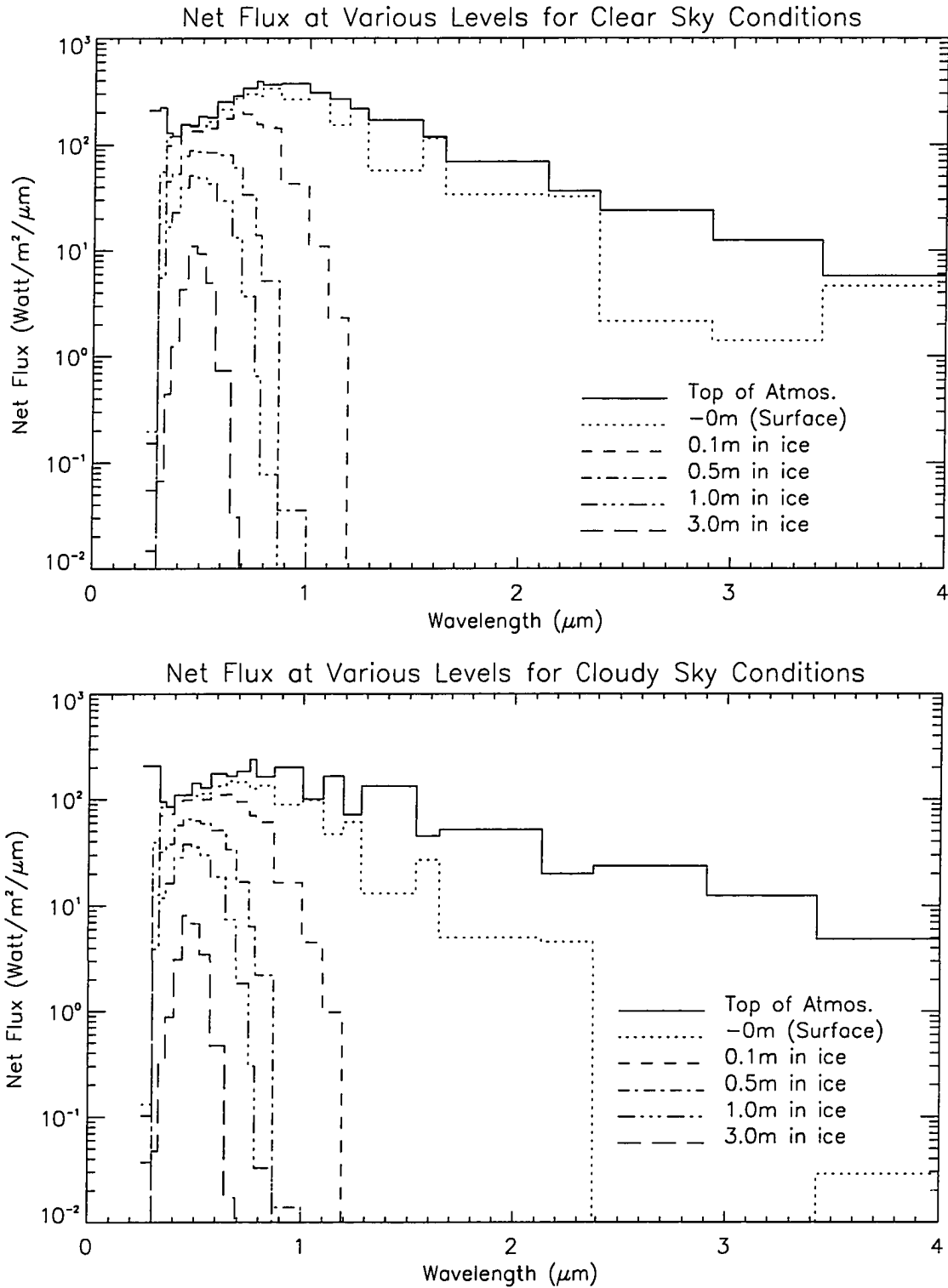
Figure 3.6 Spectral distribution of net flux at various levels for (top) clear sky and (bottom) cloudy sky conditions .

3.2.2 Absorption and Partitioning of Solar Energy in the Atmosphere-Sea Ice-Ocean System

Next we use the same models for the atmosphere, cloud, sea ice, and ocean as in Figure 3.6, but change the ice thickness to 2 m and the ice salinity to $5\%_{00}$, values representative of average salinity for thick, first-year ice [*Cox and Weeks*, 1988]. Table 3.1 quantitatively shows the distribution of the absorbed radiative energy by the atmosphere, ocean and various sublayers of the ice under both clear and cloudy sky conditions for this situation. The values in the second column represent the total amount absorbed by the entire atmosphere-sea ice-ocean system. The total solar absorption is obtained by integration over the 24 spectral bands ranging from 0.25 μm to 4.0 μm, and the total visible absorption is the integral over 12 spectral bands ranging from 0.28 μm to 0.78 μm. The energy absorbed by different layers and its percentage of the total (values in the parentheses) are listed in the rest of the columns. The data in Table 3.1 show that the total disposition of the solar radiation in the entire atmosphere-sea ice-ocean system is sensitive to bulk ice density (i.e., the amount of air included in the ice). This is especially true for visible radiation, which experiences a twofold increase under clear sky conditions when the ice density increases from 0.86 Mg/m^3 to 0.92 Mg/m^3. However, the presence of a cloud drastically reduces this sensitivity. The cloud also reduces the total absorption in the coupled system, because the cloud reflects more solar radiation back to space. The total system albedo is increased from 0.53 under a clear sky to 0.69 under a cloudy sky for the cloud used here and for the ice density of 0.86 Mg/m^3 (from 0.46 to 0.67 for ice density 0.90 Mg/m^3). Although the total radiative absorption in the whole system increases with ice density, the percentage of absorption by the atmosphere decreases, and consequently the amount of absorption in the atmosphere remains almost unchanged. In fact, the atmospheric

absorption decreases slightly with increasing ice density. The explanation for this is that less dense ice includes more air bubbles, which scatter and thereby reflect more radiation back to the atmosphere. Under clear sky conditions the top layer in the ice acts as a main absorber with the uppermost 1 cm of the ice absorbing more than 20% of the total radiative energy deposited in the whole atmosphere-sea ice-ocean system. Clouds significantly reduce both the amount and the percentage absorbed by the top layer of the ice, because most of the infrared part of the solar radiation has been absorbed and reflected by the cloud before it reaches the ice surface. Owing to less backscattering because of fewer air bubbles, denser ice also results in more transmission of radiation into the ocean and therefore produces higher absorption in the seawater under the ice. The sensitivity of this absorption by the ocean to the ice density is also reduced by clouds.

Similar to Table 3.1, Table 3.2 shows the partitioning of the absorbed solar radiation in the atmosphere-sea ice-ocean system for different ice salinities but with a fixed ice density of 0.9 Mg/m^3. These results show that the total absorption of solar radiation in the whole system decreases as the ice salinity increases and that this sensitivity is reduced by the presence of clouds. The atmosphere contributes more to the total radiative absorption as the ice salinity increases, because high salinity means more brine in the ice and therefore more brine pockets acting as scatterers, increasing the amount of reflected radiation. As the light propagates into the deeper layers of the ice and into the ocean, both the amount and the percentage of the radiative absorption in these layers do not show nearly as strong a dependence on the salinity as they do on the density, as was demonstrated in Table 3.1. This is due to the different scattering and absorptive properties of brine pockets and air bubbles. Brine pockets are stronger forward scatterers than air bubbles, and, in addition, they also act as absorbing bodies.

Table 3.3 shows the distribution of the total solar radiation absorbed by the

Table 3.1 The Amount of Solar Energy Absorbed by Various Layers and Its Percentage of the Total for Different Ice Densities .

Density, Mg/m^3	Total Absorption, W/m^2	Absorption in Various Layers and Its Percentage of the Total					
		Atmosphere	Ice				Ocean
			0-1 cm	1-10 cm	0.1-1 m	1-2 m	
Visible (0.28 - 0.78 μm), Clear Sky							
0.86	62.6	21.4(34)	1.5(2.4)	10.4(17)	23.1(37)	3.1(4.9)	3.0(4.8)
0.88	73.2	21.1(29)	1.8(2.4)	12.5(17)	29.9(41)	3.3(4.5)	4.6(6.3)
0.90	90.5	20.8(23)	2.0(2.2)	14.7(16)	41.0(45)	4.4(4.9)	7.6(8.4)
0.92	127.7	20.0(16)	1.9(1.5)	16.0(13)	61.6(48)	9.7(7.6)	18.4(14.)
Total (0.25 - 4.0 μm), Clear Sky							
0.86	315.1	114.9(36)	87.9(28)	72.2(23)	34.0(11)	3.1(1.0)	3.0(1.0)
0.88	334.5	114.3(34)	89.3(27)	79.5(24)	43.5(13)	3.3(1.0)	4.6(1.4)
0.90	361.8	113.5(31)	89.8(25)	86.8(24)	59.7(17)	4.4(1.2)	7.6(2.1)
0.92	411.6	112.2(27)	88.2(21)	90.8(22)	92.1(22)	9.8(2.4)	18.5(4.5)
Visible (0.28 - 0.78 μm), Cloudy Sky							
0.86	50.4	21.5(43)	0.9(1.8)	6.7(13)	16.2(32)	2.5(5.0)	2.5(5.1)
0.88	56.3	21.3(38)	1.0(1.8)	7.6(14)	20.0(35)	2.6(4.5)	3.8(6.7)
0.90	65.2	21.1(32)	1.0(1.6)	8.2(13)	25.7(39)	3.2(4.9)	6.0(9.1)
0.92	81.4	20.8(26)	0.8(1.0)	7.4(9)	33.6(41)	5.9(7.2)	12.9(16.)
Total (0.25 - 4.0 μm), Cloudy Sky							
0.86	210.2	132.9(63)	20.2(9.6)	30.8(15)	21.3(10)	2.5(1.2)	2.5(1.2)
0.88	217.7	132.6(61)	20.2(9.3)	32.5(15)	26.0(12)	2.6(1.2)	3.8(1.7)
0.90	228.3	132.2(58)	19.9(8.7)	33.5(15)	33.5(15)	3.2(1.4)	6.0(2.6)
0.92	246.3	131.7(53)	18.9(7.7)	31.2(13)	45.6(19)	5.9(2.4)	12.9(5.2)

Percentages of the total energy absorbed by different layers are given in parentheses.

Table 3.2 The Amount of Solar Energy Absorbed by Various Layers and Its Percentage of the Total for Different Ice Salinities .

Salinity, %oo	Total Absorption, W/m^2	Absorption in Various Layers and Its Percentage of the Total					
			Ice				
		Atmosphere	0-1 cm	1-10 cm	0.1-1 m	1-2 m	Ocean
Visible (0.28 - 0.78 μm), Clear Sky							
2.0	114.9	20.5(18)	2.4(2.1)	19.1(17)	58.4(51)	7.6(6.6)	6.9(6.0)
6.0	84.0	20.9(25)	1.8(2.2)	13.2(16)	35.8(43)	5.5(6.5)	6.8(8.0)
10.0	73.9	21.3(29)	1.4(1.9)	10.1(14)	31.6(43)	6.0(8.2)	3.4(4.5)
14.0	71.9	21.4(30)	1.4(1.9)	9.5(13)	32.8(46)	5.9(8.1)	1.0(1.4)
Total (0.25 - 4.0 μm), Clear Sky							
2.0	392.0	112.9(29)	93.0(24)	93.2(24)	78.3(20)	7.6(1.9)	6.9(1.8)
6.0	353.3	113.7(32)	88.7(25)	84.5(24)	54.1(15)	5.5(1.6)	6.8(1.9)
10.0	335.2	114.4(34)	85.0(25)	77.6(23)	48.8(15)	6.0(1.8)	3.4(1.0)
14.0	325.6	114.8(35)	82.1(25)	73.0(22)	48.8(15)	5.9(1.8)	1.0(0.3)
Visible (0.28 - 0.78 μm), Cloudy Sky							
2.0	77.5	20.8(27)	1.3(1.7)	10.1(13)	35.2(45)	5.1(6.6)	4.9(6.3)
6.0	61.6	21.2(34)	0.9(1.5)	7.4(12)	22.5(37)	4.1(6.7)	5.4(8.7)
10.0	57.3	21.4(37)	0.8(1.4)	6.1(11)	21.6(38)	4.7(8.2)	2.7(4.7)
14.0	57.2	21.6(38)	0.8(1.4)	6.2(11)	23.3(41)	4.5(7.9)	0.8(1.4)
Total (0.25 - 4.0 μm), Cloudy Sky							
2.0	241.5	131.9(55)	20.8(8.6)	35.4(15)	43.4(18)	5.1(2.1)	4.9(2.0)
6.0	224.4	132.3(59)	19.6(8.7)	32.6(15)	30.3(13)	4.1(1.8)	5.4(2.4)
10.0	218.7	132.7(61)	18.7(8.6)	30.8(14)	29.1(13)	4.7(2.1)	2.7(1.2)
14.0	217.2	133.0(61)	18.1(8.3)	30.2(14)	30.6(14)	4.5(2.1)	0.8(0.4)

Percentages of the total energy absorbed by different layers are given in parentheses.

atmosphere, snow, ice, and ocean for different snow depths on the ice and for a fixed ice density (0.90 Mg/m^3) and salinity ($5\%_{00}$). The snow is specified to have a average grain radius of 1.0 mm and density of 0.4 Mg/m^3, values representative of old snow near the melting point [*Wiscombe and Warren*, 1980]. When the results in Table 3.3 are compared with those in Tables 3.1 and 3.2 for clear sky conditions, the total solar radiation disposition in the whole system is significantly reduced because of the higher reflection at the snow surface and the resulting isolation of the absorptive ice below. Although the absorption by snow and ice are different for different snow thicknesses, the total absorption by the whole system and the absorption by the atmosphere are similar for the four snow depths used, indicating the snow surface albedo is already saturated when the snow thickness exceeds 5 cm. Even more importantly, only 5 cm of the snow layer is responsible for nearly half of the total solar absorption.

Similar to Table 3.3, Table 3.4 shows the partioning of the absorbed total solar radiation across the system obtained under four different solar elevations. As expected, a lower solar elevation (larger zenith angle) causes less absorption in the whole system, because it implies less radiative energy input to the system and also produces a higher reflection at the ice surface. Furthermore, for lower solar elevations, as a result of a higher reflection at the surface and a longer path length of light, a larger fraction of the total absorption occurs in the atmosphere and a correspondingly smaller fraction in the various layers of the ice and in the ocean. However, the presence of a cloud layer will increase the sensitivity of the fractional absorption in the ice and in the ocean to changes in solar elevation.

The occurrence of melt ponds on the ice has been shown to be important in the overall energy balance [*Ebert and Curry*, 1993]. A simulation of the solar energy distribution for different pond depths is presented in Table 3.5. Here it is assumed that the pond depth is uniform, and the energy distribution in a one-dimensional

Table 3.3 Absorbed Solar Energy by Various Layers and Its Percentage of the Total for Different Snow Depths .

Snow Depth, cm	Total Absorption, W/m²	Absorption in Various Layers and Its Percentage of the Total						
		Atmosphere	Snow	Ice				Ocean
				0-0.1 m	0.1-1 m	1-2 m		
Clear Sky								
5	275.9	117.0(42)	130.5(47)	11.2(4.1)	13.3(4.8)	1.7(0.6)		2.2(0.8)
10	275.9	117.0(42)	142.2(51)	3.0(1.1)	10.2(3.7)	1.3(0.5)		2.2(0.8)
20	275.9	117.0(42)	147.9(54)	1.6(0.6)	6.4(2.3)	0.7(0.3)		2.2(0.8)
30	275.9	117.0(42)	152.2(55)	0.8(0.3)	3.4(1.2)	0.3(0.1)		2.2(0.8)
Cloudy Sky								
5	200.2	133.7(67)	43.7(22)	7.9(4.0)	11.3(5.6)	1.5(0.8)		2.0(1.0)
10	200.2	133.7(67)	52.0(26)	2.4(1.2)	8.9(4.5)	1.1(0.6)		2.0(1.0)
20	200.2	133.7(67)	56.8(28)	1.4(0.7)	5.6(2.8)	0.7(0.3)		2.0(1.0)
30	200.2	133.7(67)	60.5(30)	0.7(0.4)	3.0(1.5)	0.3(0.2)		2.0(1.0)

Percentages of the total energy absorbed by different layers are given in parentheses.

Table 3.4 The Total Solar Energy Absorbed by Various Layers and Its Percentage of the Total for Different Solar Zenith Angles .

Solar Zenith Angle	Total Absorption, W/m²	Absorption in Various Layers and Its Percentage of the Total						
		Atmosphere	Ice					Ocean
			0-1 cm	1-10 cm	0.1-1 m	1-2 m		
Clear Sky								
40°	573.7	158.1(28)	142.5(25)	147.8(26)	104.4(18)	7.7(1.3)		13.2(2.3)
60°	361.8	113.5(31)	89.8(25)	86.8(24)	59.7(17)	4.4(1.2)		7.6(2.1)
70°	235.5	84.7(36)	55.8(24)	52.1(22)	35.6(15)	2.7(1.1)		4.6(1.9)
80°	105.6	50.4(48)	20.0(19)	19.0(18)	13.4(13)	1.0(1.0)		1.8(1.7)
Cloudy Sky								
40°	383.8	196.8(51)	39.4(10.)	65.1(17)	64.9(17)	6.1(1.6)		11.4(3.0)
60°	228.3	132.2(58)	19.9(8.7)	33.5(15)	33.5(15)	3.2(1.4)		6.0(2.6)
70°	148.0	93.5(63)	11.1(7.5)	19.0(13)	19.1(13)	1.8(1.2)		3.4(2.3)
80°	72.3	51.4(71)	4.1(5.7)	7.2(10)	7.4(10)	0.7(1.0)		1.4(1.9)

Percentages of the total energy absorbed by different layers are given in parentheses.

column of atmosphere, pond-over-ice, sea ice, and ocean is computed. The possible interaction with neighboring columns is ignored. This treatment is mandated by use of one-dimensional model. To simulate two-dimensional effects, one could, as a first approximation, use area-weighted combinations of different surface types as discussed for combination of leads and ice below. The same models for atmosphere, cloud, and ocean are used as above. Although the temperature at the ice top is 0°C and somewhat lower in the interior, for simplicity the temperature is specified to be −2°C (the same as the bottom temperature) throughout the complete ice thickness. The density is specified to be 0.93 Mg/m^3 when air volume is negligible, as it is for ice under ponds. A comparison with the results in the aforementioned tables shows that the total absorption by the whole system has been increased due to the reduced surface albedo. Also, the radiation penetration into the ocean has increased, while the absorption by the atmosphere shows only a slight change. A melt pond with a depth of only 5 cm can absorb nearly half of the total energy absorbed by the whole system.

The values in Tables 3.1, 3.2, and 3.4 indicate that although clouds reduce the total solar radiative absorption in the entire atmosphere-sea ice-ocean system, they can increase the amount of absorption in the atmosphere for the cloud model adopted here and consequently contribute to solar heating in the atmosphere. Although the increasing percentage and amount of solar absorption in the atmosphere due to the cloud is strongly dependent on solar elevation (also on liquid water path and height of clouds, as our unpublished results show), it is insensitive to ice density and salinity. Results in Tables 3.1 and 3.2 show that in the deeper layers of the ice (depth H > 1.0 m) and in the ocean the total amount of absorbed solar energy is equal to the amount absorbed in the visible portion of the spectrum in these same layers. This clearly demonstrates that only visible radiation penetrates to these layers.

Table 3.5 Absorbed Solar Energy by Various Layers and Its Percentage of the Total for Different Melt Pond Depths .

Pond Depth, cm	Total Absorption, W/m^2	Absorption in Various Layers and Its Percentage of the Total					
				Ice			
		Atmosphere	Ponds	0-0.1 m	0.1-1 m	1-2 m	Ocean
Clear Sky							
5	408.9	112.2(27)	176.8(43)	40.7(9.9)	55.8(14)	7.7(1.9)	15.8(3.9)
10	418.8	111.9(27)	224.0(54)	18.9(4.5)	41.8(10)	6.7(1.6)	15.5(3.7)
20	432.7	111.6(26)	264.0(61)	9.2(2.1)	27.8(6)	5.2(1.2)	14.9(3.4)
40	450.3	111.2(25)	302.1(67)	3.9(0.9)	16.0(4)	3.2(0.7)	13.9(3.1)
Cloudy Sky							
5	243.1	131.7(54)	48.7(20)	16.4(6.7)	29.9(12)	5.0(2.1)	11.3(4.7)
10	245.8	131.6(54)	67.0(27)	8.8(3.6)	23.1(9)	4.4(1.8)	11.0(4.5)
20	249.8	131.5(53)	84.0(34)	4.7(1.9)	15.9(6)	3.3(1.3)	10.4(4.2)
40	255.1	131.5(52)	100.4(39)	2.2(0.9)	9.5(4)	2.0(0.8)	9.5(3.7)

Percentages of the total energy absorbed by different layers are given in parentheses.

From these tables it is not difficult to determine the fraction of the net incoming solar radiation which penetrates into the interior of the ice (below a depth of 10 cm). This is an important parameter used in ice thermodynamic models [*Maykut and Untersteiner*, 1971; *Semtner*, 1976; *Ebert and Curry*, 1993] and polar climate models [*Parkinson and Washington*, 1979; *Bennett*, 1982; *Van Ypersele*, 1990]. For cloudy skies this value is dependent on the cloud conditions. For clear skies the tables show a minimum of 0.20, which corresponds to the lowest ice density (highest air volume) used in Table 3.1 . This value is higher than values (typically 0.17 or 0.18) used in ice thermodynamic models and climate models, while the parameters for sea ice used in the tables should have covered most of the ice property variations. This value is primarily determined by the scattering properties of the air bubbles in the uppermost few centimeters of ice.

3.2.3 Radiative Heating in Sea Ice

To demonstrate how the absorption within the sea ice responds to the variation of the physical properties of the ice, Figure 3.7 shows the absorption profiles (heating rates), $dF(z)/dz$ (in milliwatts per cubic centimeter), with depth in the sea ice for different densities and salinities under clear sky conditions. Here z is the depth in the sea ice measured downward from the upper ice surface. The same model inputs for atmosphere, sea ice, and ocean as used in Figure 3.6 have been used in these computations. The thicker lines in the plots represent the total absorbed solar radiation (0.25 μm-4.0 μm) while the thinner lines represent the radiative energy absorbed in the visible region (0.28 μm-0.78 μm). Owing to the rapid decrease in radiative absorption with depth in the near-surface layer of the ice, logarithmic scales were chosen for both axes.

These figures clearly demonstrate that although the absorption profiles are complicated within the first few centimeters of the top layer, below this depth, the radiative absorption increases as ice density increases and as salinity decreases. Again, these phenomena can be attributed to the different optical properties possessed by the different components in the ice. Generally, pure ice absorbs strongly in the whole solar spectrum except in the relatively narrow visible region, where a larger part of the solar radiative energy reaching the ice surface is concentrated. Both denser ice and less saline ice contain a larger fractional volume of pure ice, resulting in increased absorption. On the other hand, denser ice includes less air bubbles and the less saline ice includes less brine volume. Both of these reductions in the number of scatterers reduce the optical path for light propagating to deeper layers and consequently decrease the amount of absorption. Therefore the magnitude of the radiative absorption in the ice depends on these two competitive processes.
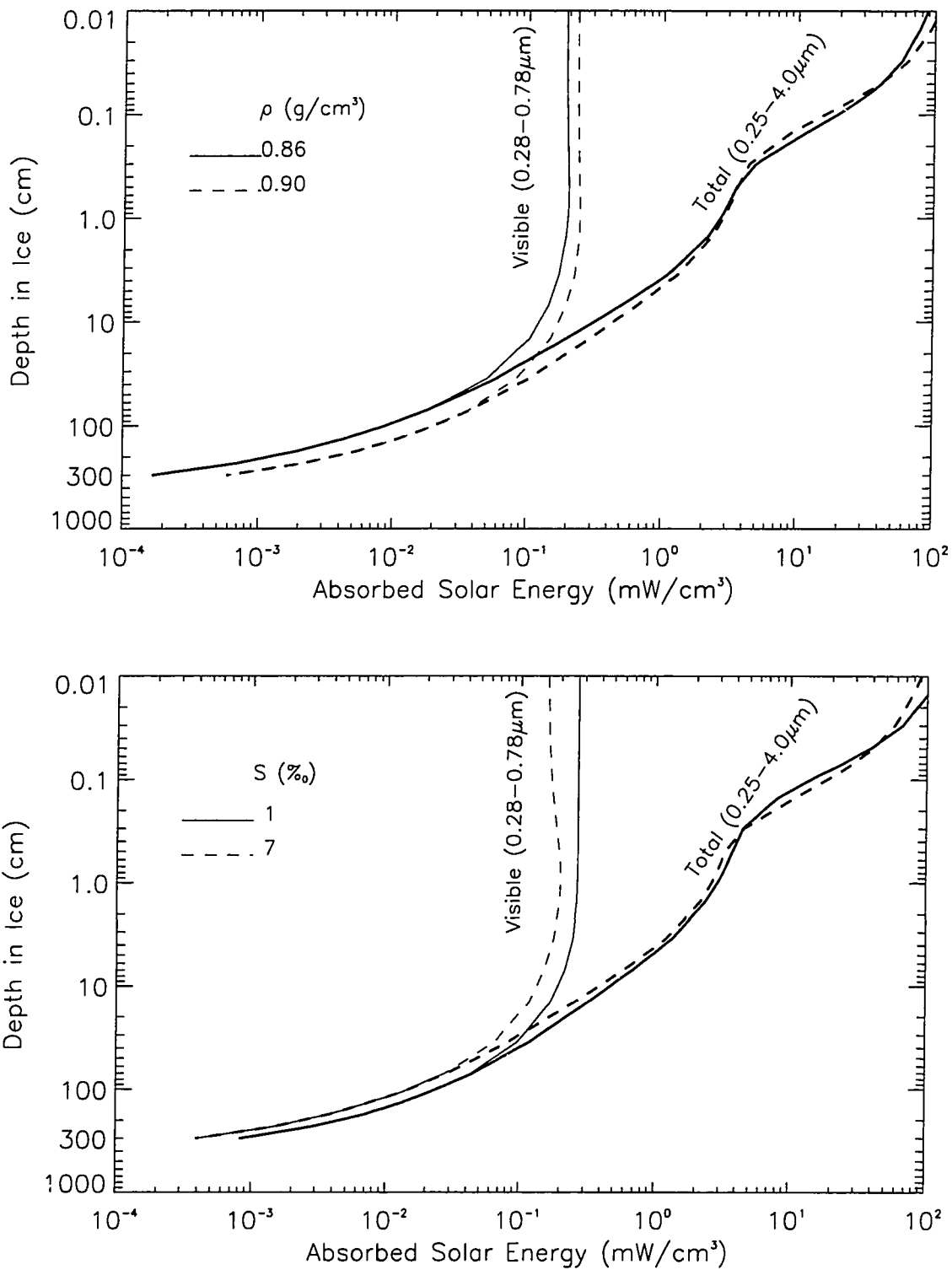
Figure 3.7 Distribution of the absorbed solar energy with depth in the ice for different ice densities (upper panel) and salinities (lower panel) under clear sky conditions .

Most of the infrared and ultraviolet energy in the solar radiation reaching the ice surface would be absorbed within a very thin top layer of the ice because of the strong absorption by pure ice at those wavelengths. Consequently, in the upper layers of sea ice the absorption of the total solar radiation is dominated by the presence of pure ice. This is reflected in Figure 3.7 by the total solar radiative absorption in the thin top layer increasing as ice density increases and as salinity decreases. Then, as more infrared radiation has been absorbed, enhanced absorption due to multiple scattering becomes more important and dominates immediately beyond the thin top layer, causing an increase in the total solar absorption as the ice density decreases and the salinity increases. However, absorption below the depth of a few centimeters, where most of the remaining radiation is in the visible spectrum, will increase with increasing ice density and decreasing salinity due to the less scattering, leading to less reflection by the ice. The absorption rate in the visible spectrum shows only a small change within about 10 cm of the top layer. Figure 3.7 shows that the absorbed amounts of total radiation and visible radiation get closer and closer as the depth increases, and at about 50 cm in depth they overlap. This indicates that almost all the radiation beyond the visible region is absorbed by the top 50 cm of sea ice.

3.2.4 Effects of the Ice Thickness

In this example we will investigate the effects of the ice thickness on the radiative energy budget in the atmosphere-sea ice-ocean system using the same atmosphere, cloud, and ocean models as above. The ice model is also similar, but observed changes in the average salinity as a function of ice thickness are now included based on a recent compilation of cold first-year ice data by W. F. Weeks (personal communication, 1994). The mean salinity values S at depth h_i in the ice are

observed to be well described by the following two linear relations:

$$S = 17.0 - 31.63h_i, \qquad h_i \leq 0.3 \, \text{m} \qquad (3.6a)$$

$$S = 8.0 - 1.63h_i, \qquad h_i > 0.3 \, \text{m} \qquad (3.6b)$$

The temperature at the top of the ice will still be assumed to remain at $-10°C$ and to increase linearly with depth to $-2°C$ at the ice-water interface. Figure 3.8 shows the dependence of the total solar energy absorbed by the atmosphere, sea ice, and ocean, respectively, on the ice thickness. Results indicate that although the total solar energy disposed in the entire system decreases as ice thickness increases, the rate of decrease becomes smaller as the ice thickness increases, with the total radiative absorption approaching a nearly constant value after the ice thickness reaches about 70 cm. As the ice thickness increases, the absorption by the ice increases and that by the ocean decreases, with the rates of change, again, depending on the ice thickness. On the other hand, the absorption by the atmosphere remains almost unchanged as ice thickness changes. A comparison of the two panels in Figure 3.8 indicates that not only does the cloud drastically reduce the energy disposition into the ice and the whole system for any ice thickness and that into the ocean for thin ice, but also it significantly reduces all sensitivities of the absorbed solar energy to the ice thickness, especially when the ice is thin. The solar zenith angle used here is still at $60°$. However, our unpublished results show that the general behavior indicated above is true for all solar elevations and cloud heights except that the magnitudes of all the components change.

3.2.5 Effects of Open Ocean

It is well known that the occurrence of areas of open water (leads, polynyas) within an ice field has an important impact on the solar energy distribution. Using the

(a). Clear Sky

(b). Cloudy Sky

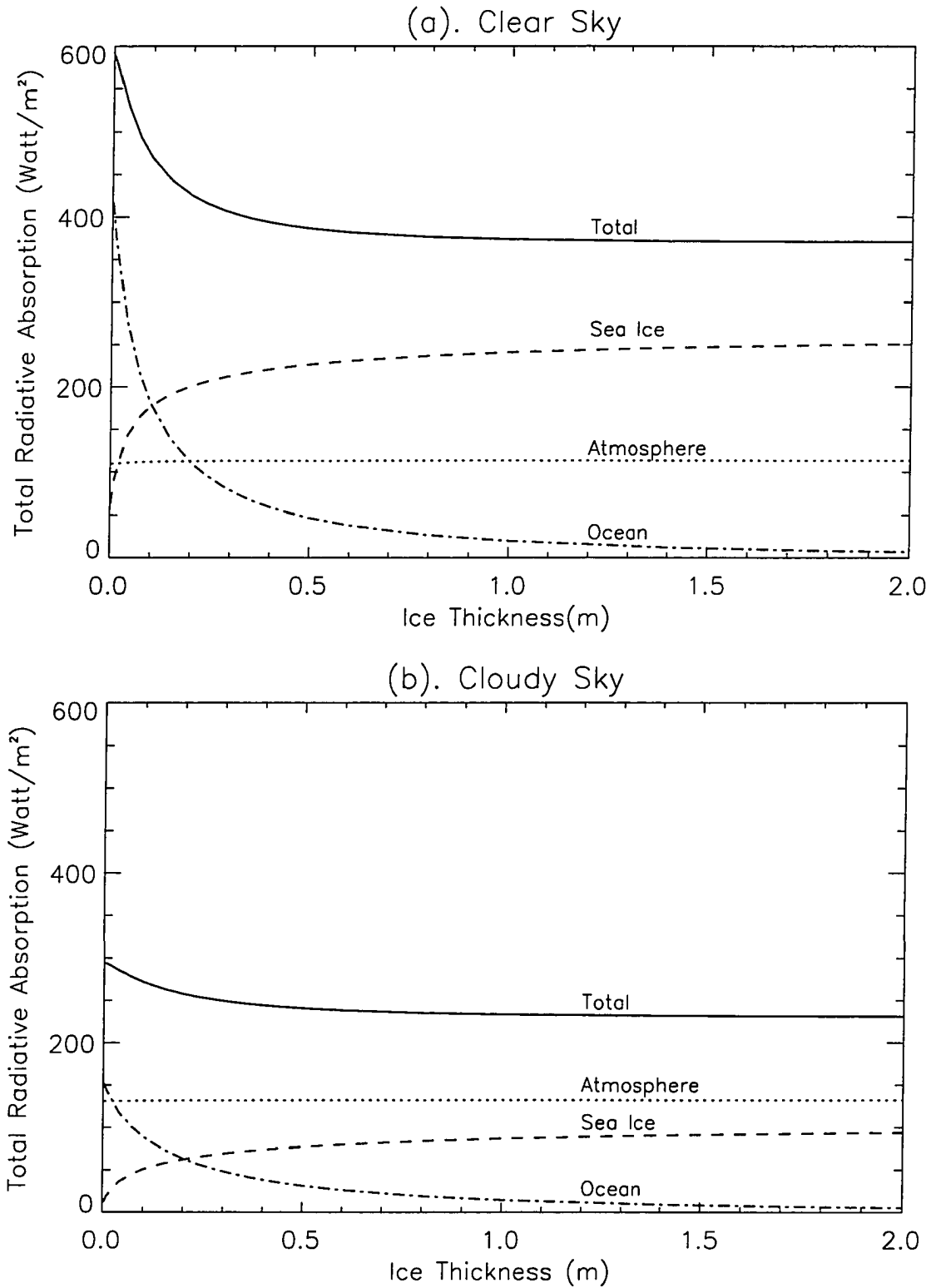**Figure 3.8** The distribution of total solar radiative absorption in the atmosphere, sea ice, and ocean system as a function of the ice thickness for (a) clear sky and (b) cloudy sky conditions .

(a). Clear Sky
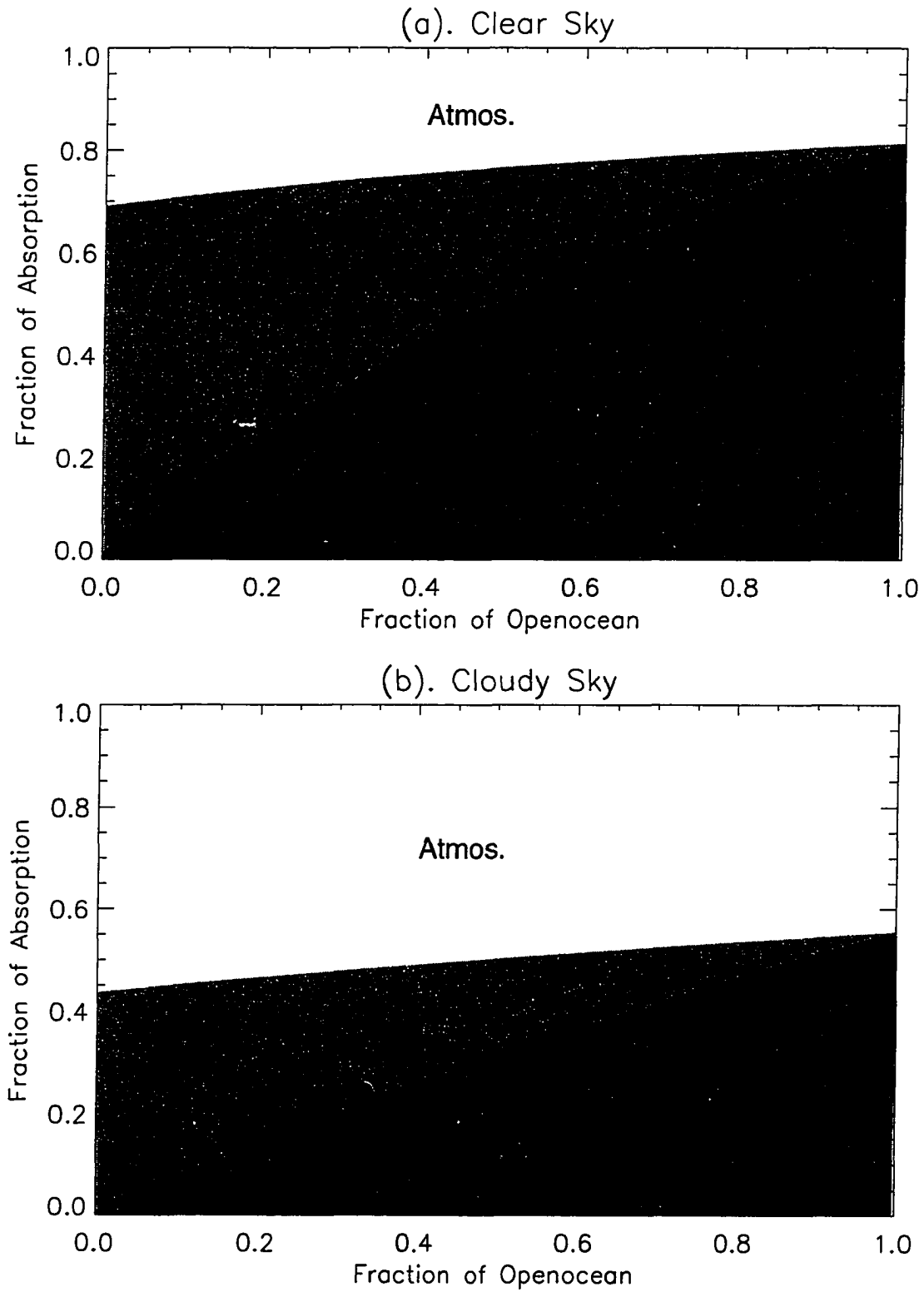
(b). Cloudy Sky

Figure 3.9 Distribution of the absorbed solar energy in the atmosphere, sea ice, and ocean as a function of open ocean fraction for (a) clear sky and (b) cloudy sky conditions .

same models as used in Tables 3.3 and 3.4, Figure 3.9 shows the solar energy partioning in the atmosphere, sea ice, and ocean (including open ocean and ocean under the ice) as a function of the area fraction of open water. The absorption by the atmosphere, ice, and ocean are represented by different shades of gray in Figure 3.9. Here the vertical distance covered by the three different shades gives the fraction of absorption. Area-weighted irradiances are used in this computation, as explained earlier. A similar method has been used and discussed by *Perovich* [1990] in estimating light reflection and transmission by spatially varying sea ice covers. This procedure actually ignores the horizontal radiation interaction by multiple scattering between the two different columns. Figure 3.9 shows that as the area fraction of open water increases, the solar radiation deposited in the ocean increases rapidly, from 2% under the ice cover to 80% under ice-free conditions and under clear sky conditions. The increase of the absolute value is even more pronounced, because the total absorption in the entire system increases with the open water fraction. Although the fraction of total absorption both in the ice and in the ocean is sensitive to the open ocean fraction, especially under clear skies, the fraction deposited in the atmosphere is not.

3.2.6 Effects of Cloud Microphysics

As presented in equations (3.2), the cloud optical properties are dependent on their microphysics. Therefore, variations in cloud microphysical properties will result in variations in cloud optical properties, and consequently alter the solar energy distribution in the whole atmosphere, sea ice and ocean system. Adopting the same models as above, Figure 3.10 shows the dependence of the solar energy disposition in the atmosphere-sea ice-ocean system on cloud microphysics. It indicates that the absorption in the atmosphere, sea ice and ocean will increase as the equivalent

radius of the cloud increases for the cloud model used here. On the other hand, absorption in the ice and ocean decreases as the liquid water content increases, but the absorption in the atmosphere exhibits the opposite dependence, and the combined effect is that the total absorption in the entire system will decrease as the liquid water content increases. Moreover, the absorption in sea ice shows greater sensitivity to both the equivalent radius and the liquid water content of clouds.

Figure 3.11 shows the effects of the equivalent radius and liquid water content of clouds on the outgoing shortwave energy at the top of atmosphere (TOA) and the incident solar energy at the ice surface. The results indicate that the outgoing flux at TOA will decrease as the equivalent radius increases, but increase as the liquid water content increases. Consequently, the downward flux at the surface exhibits opposite dependences on the microphysics of the clouds as compared with the outgoing flux.

For a fixed cloud equivalent radius of 7 μm, Figure 3.12 shows the effects of cloud liquid water path (LWP) on the solar energy balance in the atmosphere, sea ice and ocean system for various cloud heights. From this figure, we find that (i) the outgoing solar flux at the TOA increases as the LWP or cloud thickness increases, especially for thin clouds (low LWP); the higher the cloud, the faster this increase; (ii) although the downward flux at the ice surface and the total absorption of solar energy by the ice and ocean decrease as cloud thickness or LWP increases, they are not sensitive to the cloud height (their values for different cloud heights almost overlap with each other); (iii) on the other hand, absorption by the atmosphere is sensitive to cloud height and has different dependence on the LWP. For example, the absorption by the atmosphere simply increases as the LWP increases for the low clouds, but it decreases first (when the cloud is thin) and then increases as the LWP increases for high clouds.
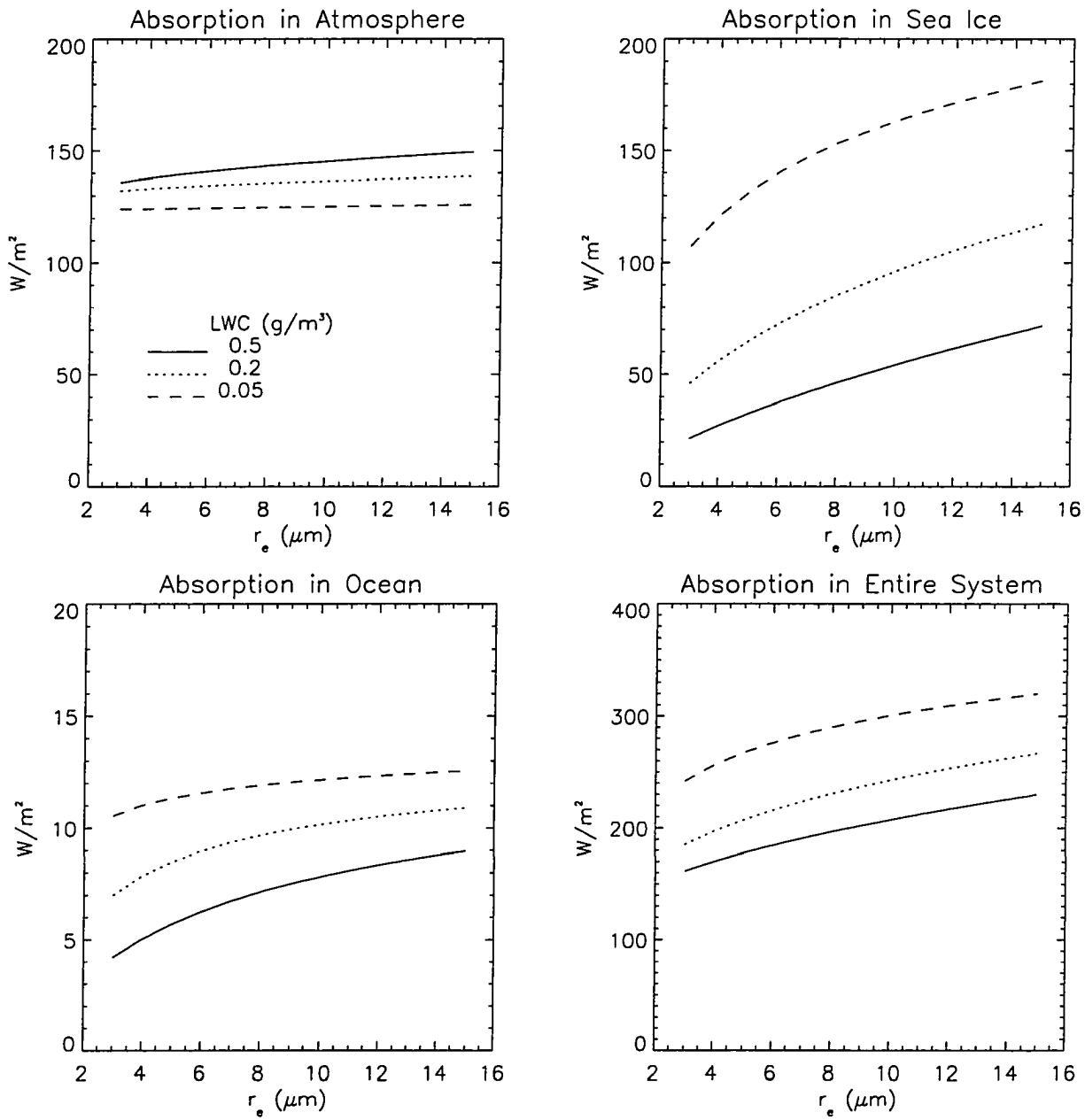
Figure 3.10 Absorption of solar radiation in various layers as a function of cloud equivalent radius .
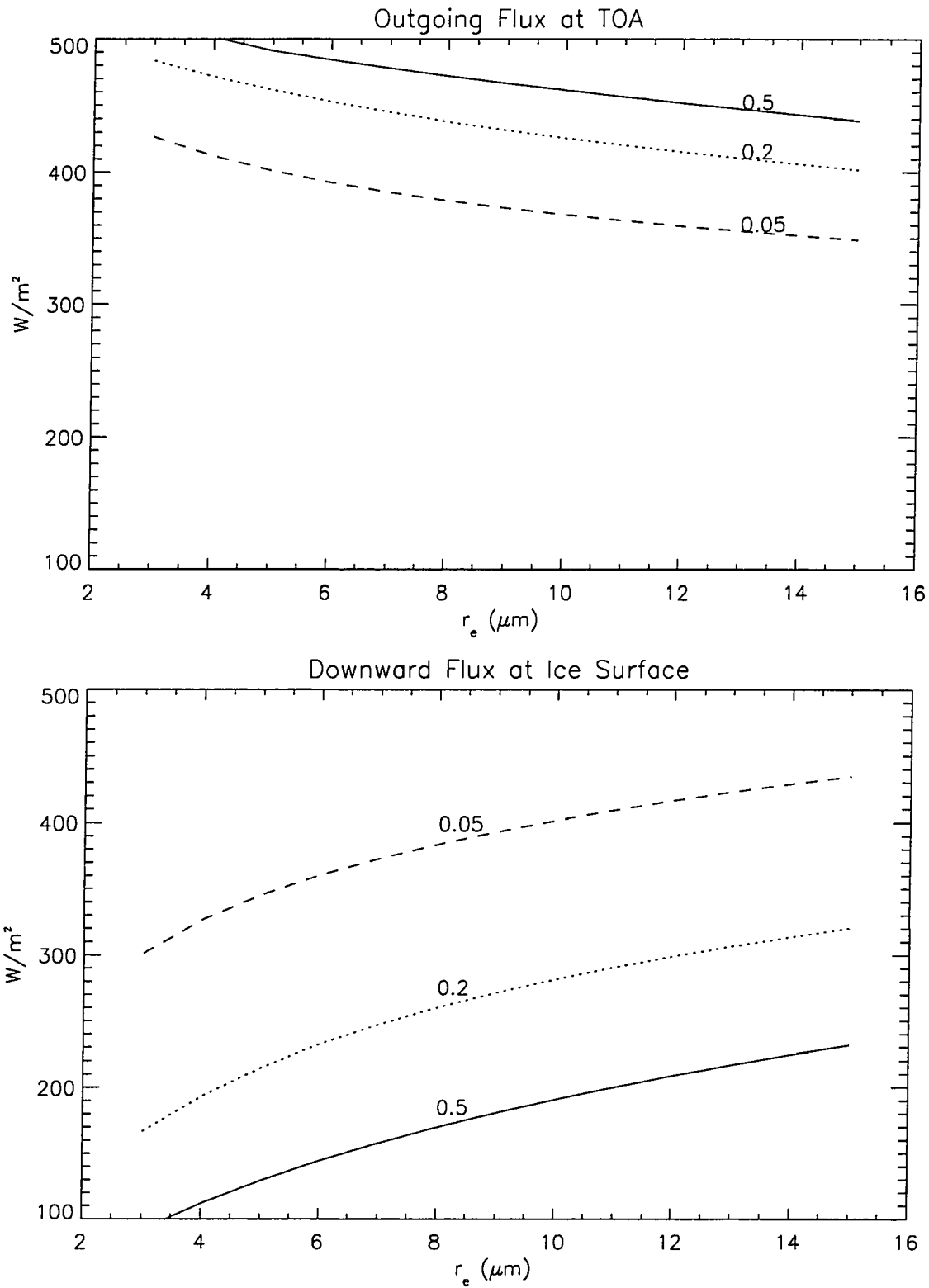
Figure 3.11 Shortwave flux as a function of the equivalent radius of cloud droplets. Labels represent the liquid water content of the clouds .
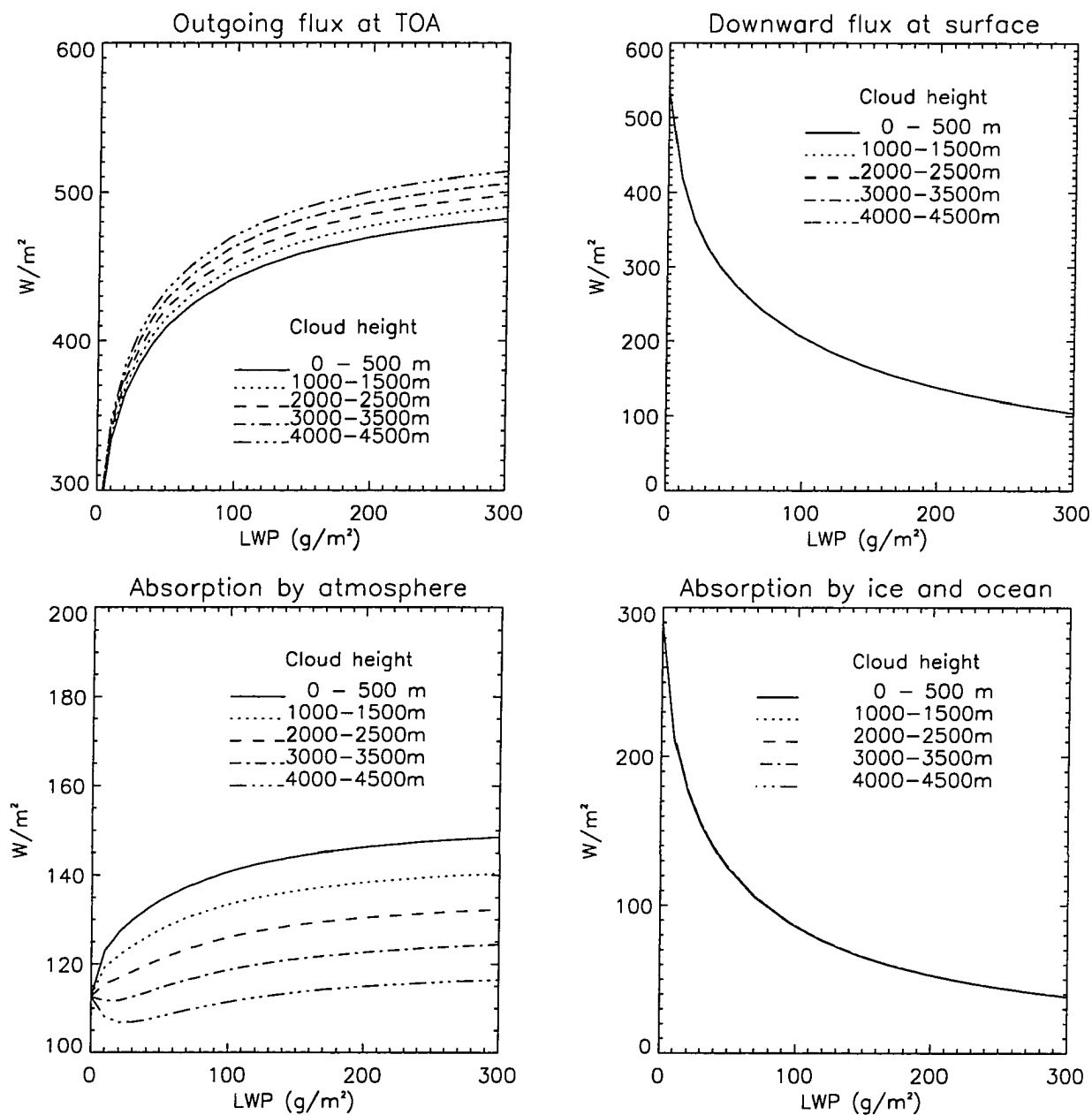
Figure 3.12 The effects of cloud height on the solar energy balance in the atmosphere-sea ice-ocean system .

3.3 Surface Albedo

3.3.1 Model Computation

Because the coupled radiative transfer model considers the ice and ocean just as additional "atmospheric" layers, the surface albedo can easily be calculated by this model. For models of atmosphere, sea ice and ocean identical to those used in Figure 3.9, Figure 3.13 shows the surface albedo as a function of snow thickness (upper panel) for a snow-covered ice surface, and as a function of ice thickness (lower panel) for a snow-free ice surface. Here the parameters for old snow are the same as those used previously for the snow model. New snow, on the other hand, is assumed to have a mean grain radius of 100 μm and a density of 0.2 Mg/m^3. Figure 3.13 indicates that the surface albedo rapidly increases as the ice or the snow thickness increases. This is especially true when the snow or the ice is thin and under cloudy conditions. The albedo approaches a constant value as the thickness of snow or ice continues to increase. Apparently, clouds increase the sensitivity of the surface albedo to variations in the snow and ice thickness. Because of the smaller grain size, new snow more efficiently scatters light back to the atmosphere. Therefore new snow has a higher albedo. Of all the possible cases, it is the combination of new snow and cloudy sky conditions that yields the highest surface albedo.

Figure 3.14 shows the surface albedo as a function of the cloud liquid water path (LWP). Increasing LWP means increasing either cloud optical depth or cloud thickness. The upper panel shows that the surface albedo increases as the cloud thickness increases both for snow-covered and snow-free surfaces. The lower panel presents the cases for different solar elevations. For clear sky conditions (LWP=0) or thin clouds, the surface albedo is sensitive to the solar elevation and this sensitiv-

Surface albedo

Surface albedo (snow−free)
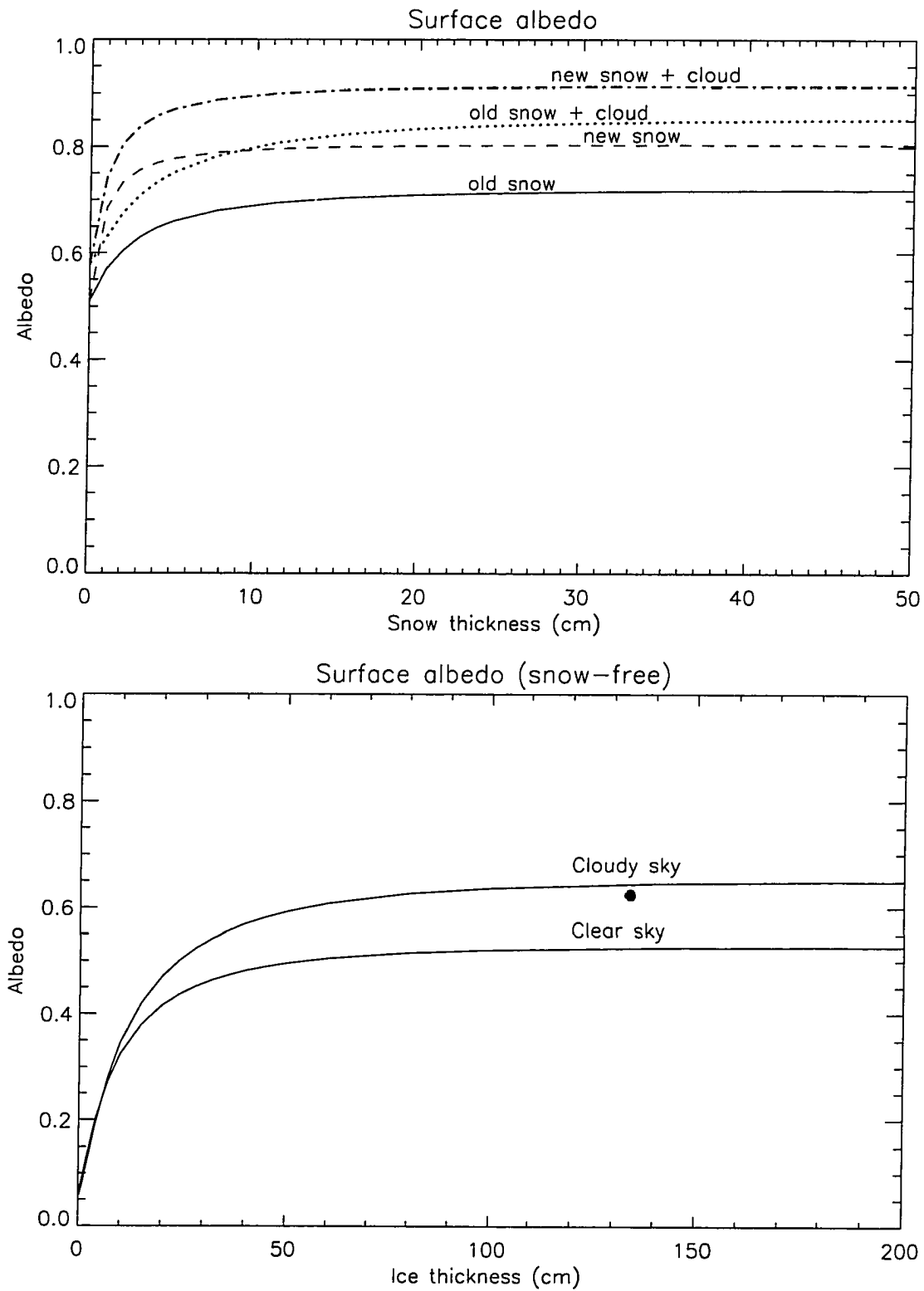
Figure 3.13 The surface albedo as a function of snow thickness and ice thickness .

Surface albedo
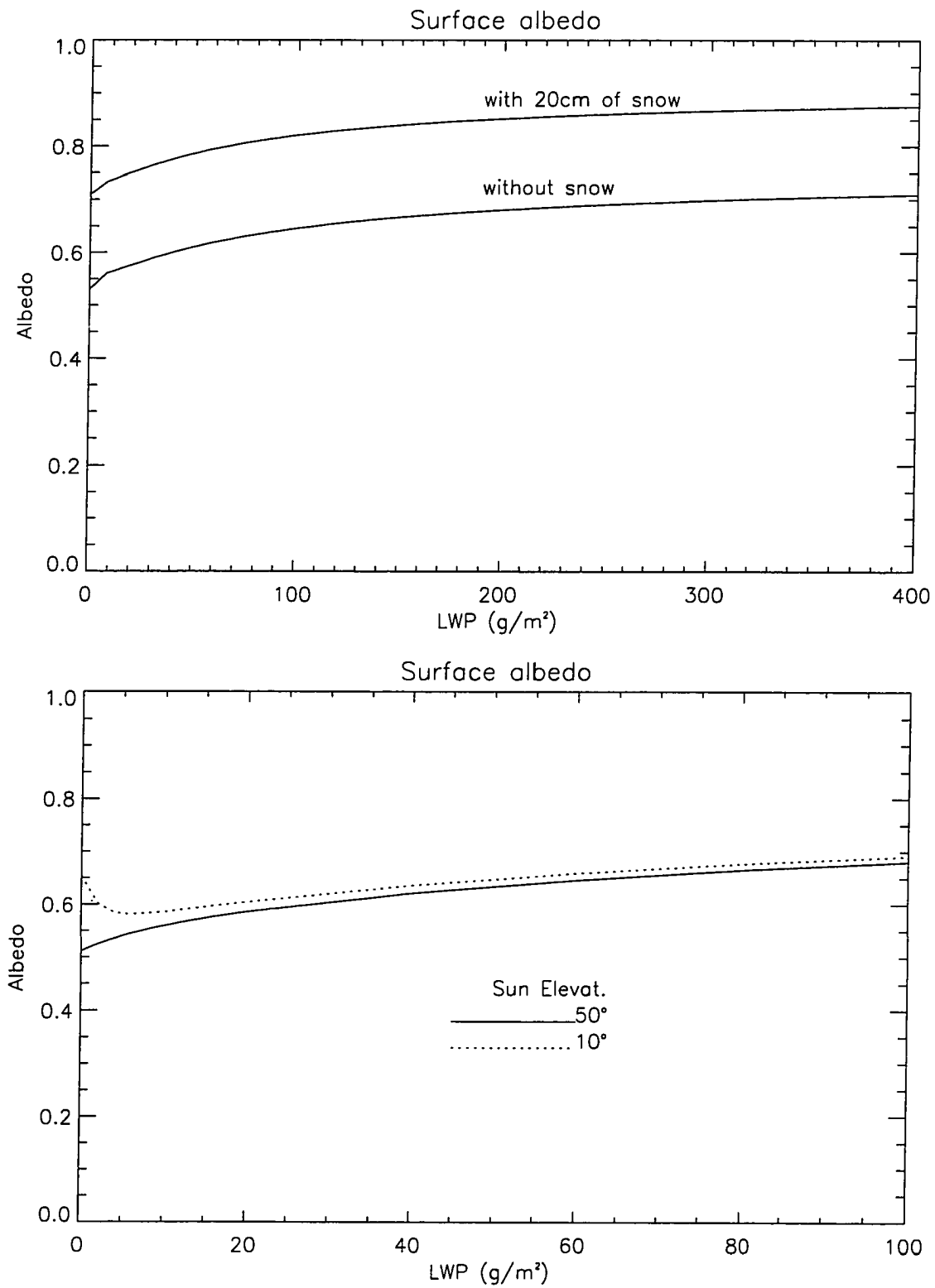
Surface albedo

Figure 3.14 The surface albedo as a function of cloud liquid water path (LWP) .

ity decreases as the cloud thickness increases. For high solar elevation conditions, the surface albedo increases simply as the LWP increases. However, for low solar elevation conditions, the surface albedo will first decrease and then increase as the cloud optical depth increases. All these effects can be explained by the different reflection properties of the ice surface to the direct and diffuse incident radiation. The direct albedo depends on the solar elevation, whereas the ratio of the direct and the diffuse radiation reaching the surface depends on the cloud thickness.

3.3.2   Comparison With Observations

Desirable model-data comparisons require comprehensive optical data sets for the atmosphere, the ice, and the ocean. Unfortunately, such radiation measurements with simultaneous observational data on the environmental parameters have, to date, not been made. This lack of data makes accurate comparisons with coupled radiative transfer models difficult. However, of all the radiation quantities, the spectral albedo of the ice surface is the one parameter on which the atmosphere and ocean have only a minor influence if the sky is overcast (when the radiation incidence on the surface can be considered to be diffuse). In addition, only the properties of the thin top layer of the ice are important for this albedo, and as a result it is presently probably the best quantity available for comparison. Therefore two observational spectral albedos for two relatively simple ice types are chosen for comparison. These are melting multiyear white ice and melting first-year blue ice. The observed spectral albedos are taken from the observations reported by *Grenfell and Maykut* [1977]. Unfortunately, the data needed to specify the model uniquely were not obtained, so the comparison is only approximate. In the computations, because melting ice is being considered, we have specified the average ice temperature as $-2°C$. For the multiyear ice considered in Figure
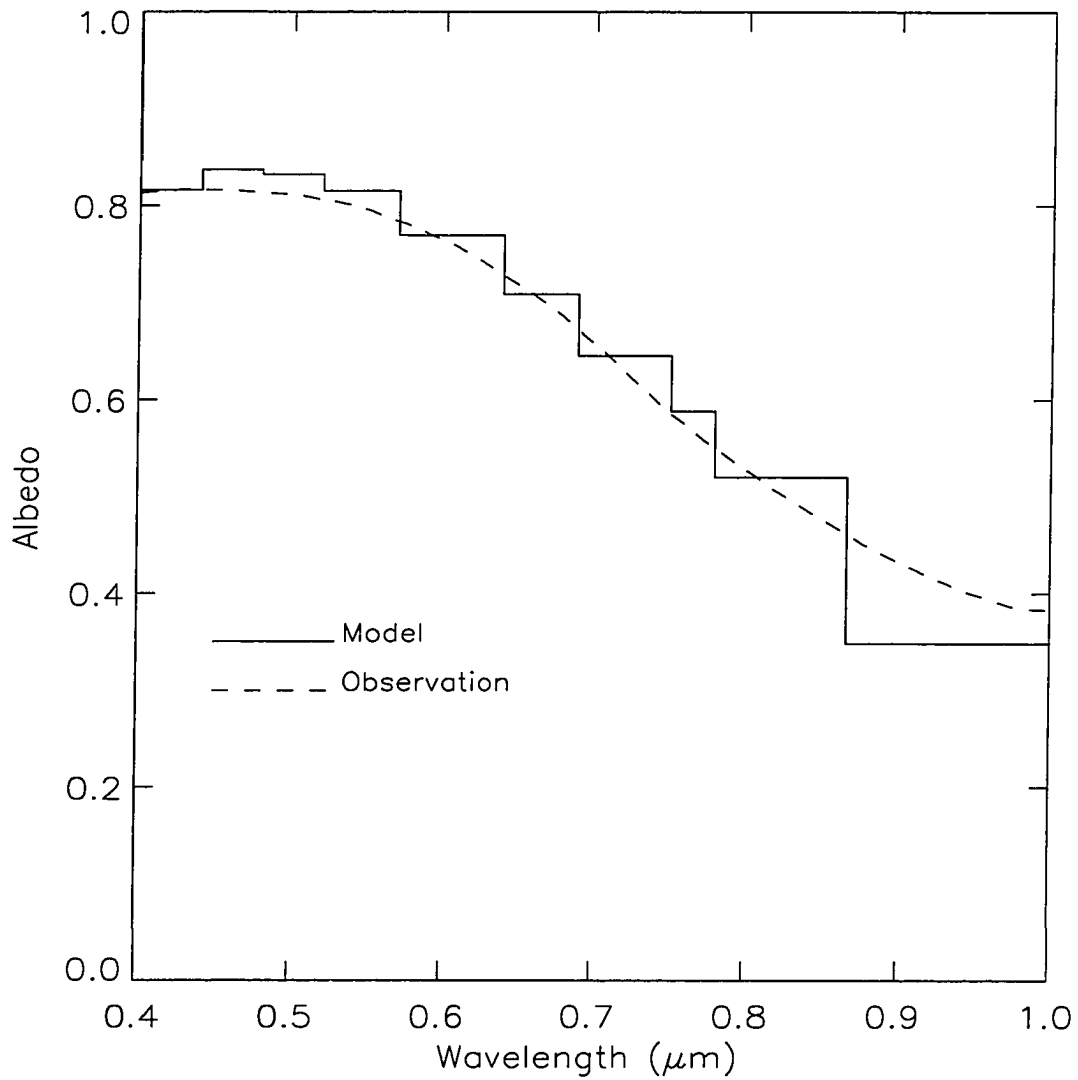
Figure 3.15 A comparison of the observed spectral albedo for melting multiyear white ice with model calculations. Observations are from *Grenfell and Maykut* [1977] .
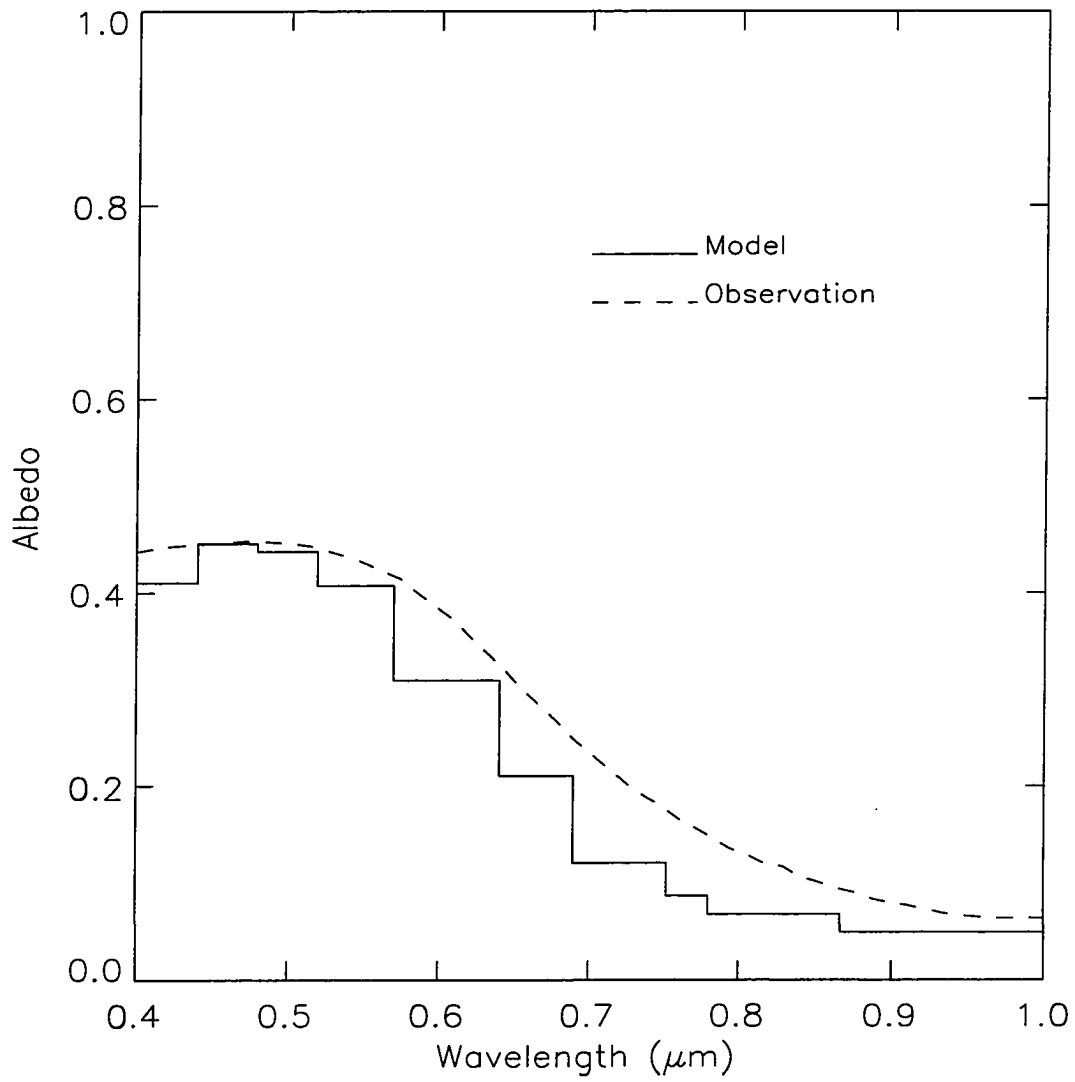
Figure 3.16 As in Figure 3.15, but for melting first-year blue ice .

3.15, recently parameterized profiles of salinity and air volume developed by W. F. Weeks (unpublished field data from ice station Crystal, 1986) are used. The salinity is expressed as

$$S = 2.785Z + 1.984Z^4 \tag{3.7a}$$

$$Z = z/h_i, \qquad 0 < Z \le 1.0 \tag{3.7b}$$

which is based on a total of 769 individual measurements from multiyear floes at which the actual ice thickness varied between 1.99 and 5.45 m. The Z in the formula is the normalized ice thickness, and z and h_i are the actual depth in ice and actual ice thickness, respectively. The air volume for the multiyear ice is parameterized as

$$V_a = 18.55 - 7.6Z + 257.1 \exp(-46.3Z) \tag{3.8}$$

a relation that is also based on field observations in the Arctic ocean. In this simulation, air volume is used directly for model input, while the brine volume is calculated as discussed in section 2. For the first-year blue ice in Figure 3.16 we have used a salinity of 5‰ as in the tables above, a value representative of thick first-year ice, and a density of 0.94 Mg/m^3, which assumes that the air volume is negligible, as it usually is for the first-year blue ice. The comparisons shown in Figures 3.15 and 3.16 are in quite good agreement, particularly with respect to the wavelength dependence. For multiyear ice the model predicts a little higher albedo at shorter wavelengths and a little lower at longer wavelengths than observed. For first-year ice the model predicts a little lower albedo overall. However, the agreement could be improved by adjusting one or more of the input parameters, for example, the salinity profile. At present, it is not possible to determine whether the differences between the model results and observations are the result of inaccurate representations of the ice properties and/or the inappropriately assumed parameters in the Mie calculations of the optical properties of the ice.

3.4 Summary

In this chapter, the radiative transfer model described in Chapter 2 for nonuniformly refracting media has been implemented and applied to the atmosphere-sea ice-ocean system and been used to study the solar energy budget in this coupled system. This model rigorously accounts for the multiple scattering and absorption by atmospheric molecules, clouds, snow and sea water, as well as the inclusions trapped in sea ice such as the brine pockets and air bubbles.

The input parameters required by the model are observable physical properties (e.g., the profiles of temperature, pressure, and gas concentrations in the atmosphere, the water or ice content of clouds, and the equivalent radius of cloud droplets, as well as the profiles of temperature, density, and salinity in the ice).

This model has been applied to study the radiative interactions within the atmosphere, sea ice, and ocean system and to investigate the effects of the ice properties, ice thickness, snow, and cloud on the radiative energy disposition and its distribution within the coupled system. On the basis of the modeling results we can conclude that the sea ice has a significant impact on the absorption and partitioning of solar radiative energy in the atmosphere, sea ice, and ocean system. Because changes in the physical properties of the ice, such as density, salinity, and temperature, lead to changes of the optical properties within the ice, such as scattering and absorption, and because of interactions occurring between the atmosphere, sea ice, and ocean, changes in the physical properties of the ice can alter the radiative transfer and the interaction processes within the entire system. Generally, as the ice density increases, the radiative absorption will increase in the entire coupled system, as well as in the sea ice and in the ocean, while the absorption in the atmosphere exhibits a slight decrease. As the ice salinity increases, the radiative absorption in the entire coupled system, in the ice, and in the ocean

decreases. The absorption profiles in the ice show that most of the radiative energy absorbed by sea ice occurs in a very thin top layer of the ice. This is especially true under clear sky conditions. Just the top 10 cm thick layer of ice can absorb more than 50% of the total solar radiation deposited in the entire system. Also, at depths greater than 50 cm in the ice, only visible radiation is left because of the strong absorption of the ice beyond this wavelength region.

In sea ice it is the scattering by inclusions, especially the air bubbles, in a few centimeters of the uppermost layer that plays the vital role to the solar energy absorption and partitioning in the whole system. Greater scattering in this top layer will not only increase backscattering to the atmosphere, but it also increases the absorption fraction in this top ice layer itself and decreases the radiation penetrating to the deeper layers of the ice and into the ocean. Because air bubbles have much higher scattering effectiveness than brine pockets, the radiative absorption is more sensitive to air volume variations than to brine volume variations. Therefore to estimate the solar energy distribution with confidence, one must have access to realistic estimates of the air volume fraction in the ice. Estimates for the top few centimeters of the ice are particularly important.

Ice thickness also exerts a significant influence on the radiative energy balance in the atmosphere-sea ice-ocean system, especially when the ice is thin. Increasing the ice thickness in the thickness range between 0 and 70 cm results in an increase in the radiative absorption in the ice and a decrease in the ocean, as well as a decrease in the entire system. However, the total absorption in the entire system remains almost constant once the ice thickness exceeds about 70 cm. Nevertheless, the absorption within the atmosphere is not sensitive to ice thickness changes.

Clouds in the atmosphere and snow on the ice reduce the solar energy absorption in the ice and in the ocean, as well as in the entire atmosphere-sea ice-ocean system. The clouds will moderate any variation in the radiative energy budget

caused by changes in ice properties and ice thickness. In other words, clouds reduce the sensitivity of the absorbed solar energy in every layer to changes in ice properties and thickness.

The distribution of solar energy is also affected by the cloud microphysics. In the coupled atmosphere, sea ice and ocean system, the outgoing solar radiation at the TOA will decrease as the equivalent radius of cloud droplets increases, but increase as the liquid water content of clouds increases. Consequently, the downward solar radiation at the ice surface exhibits a dependence on the cloud microphysics that is opposite to that of the outgoing flux. The absorption of solar radiation in the entire system will increase as the equivalent radius of cloud droplets increases. The absorption in sea ice shows a greater sensitivity to the cloud microphysics than the absorption in the atmosphere or in the ocean. The absorption in sea ice and ocean is not sensitive to cloud height, which is different from the case in atmosphere.

Surface albedo can be easily calculated by this coupled model. The results show that the surface albedo is determined by approximately 10 cm of the uppermost layer of snow for a snow covered surface and by about 50 cm of the uppermost layer of ice for a bare ice surface. Generally, surface albedo increases as cloud optical depth increases, unless the solar elevation is low and the cloud is thin. The effect of solar elevation on the surface albedo is small if the cloud is thick. Of all the possible cases, new snow plus thick clouds yields the highest surface albedo. Although comparisons with observation for two selected ice types have shown good agreement, realistic simulations and more meaningful comparisons clearly require accurate and detailed specification of the ice properties, such as profiles of salinity, density and temperature.

Realistic simulations of the radiative energy budget requires in situ data from measurements. This includes the profiles of relevant parameters described above

for the atmosphere, sea ice, and ocean, or else the profiles of optical properties, in particular, the light extinction and absorption, as well as the phase function of scattering. Simultaneous measurements of the radiative quantities, including the spectral upward and downward fluxes, would be very useful in verifying the model simulations.

Chapter 4

Application of the Coupled Radiative Transfer Model to the Study of Light Transport in Sea Ice and in the Ocean

In the polar oceans, light transmission through the atmosphere and sea ice is essential to the growth of plankton and algae [SooHoo et al., 1987; Holm-Hansen et al. 1977; Arrigo et al., 1993]. Understanding the physical conditions that affect the growth of plankton and algae is not only of interest in its own right, but as this material represents primary production upon which the food chains of the polar oceans are based, it is a requisite to understanding the behavior of the complete marine ecosystem in these regions. The atmosphere is almost transparent to photosynthetically active radiation (PAR). Within the spectral region of PAR

---

[0]The first part of this chapter is based on material published as Z. Jin, K. Stamnes and W. Weeks, Transport of photosynthetically active radiation in sea ice and ocean, *Ocean Optics*, Proc. SPIE., Vol.2258, 954-964, 1994.

95

(400 nm–700 nm), ozone is the only absorptive gas of significance present in the atmosphere. Even clouds and sea ice have a relatively weak absorption in this part of the spectrum. In addition, nearly 40% of the extra-terrestrial solar radiation lies within this narrow spectral region and much more than 40% of the total solar radiation incident on the ice surface is within the PAR range, depending on the atmospheric conditions. Therefore, PAR constitutes the main light resource for the primary productivity in the ice-covered oceans. Light availability also experiences much greater seasonal variability and rapid temporal variations at high latitudes. Clouds and snow as well as the amount and distribution of algae within the ice also have a significant impact on light availability under sea ice. In this chapter, the coupled radiative transfer model described in Chapter 2 will be used to study the transport of light, especially the photosynthetically active radiation (PAR), in the whole coupled atmosphere-sea ice-ocean system in order to quantify the effects of clouds, snow and algae as well as of ozone in the atmosphere on the light available for photosynthesis both within the ice and in the ocean below. The comparison of measured spectral irradiance and extinction in an Antarctic sea ice floe with model computation will also be presented.

4.1 Model Computations

As in chapter 3, in the following computations the McClatchey [1972] atmosphere model for the sub-arctic summer will be adopted and the atmosphere will be divided into 25 layers. In the spectral region of PAR, atmospheric absorption is mainly caused by ozone. The ozone profile is also taken from the McClatchey atmosphere as shown in Figure 3.4, while the absorption cross section of ozone and the scattering cross section by air molecules are taken from a compilation by WMO [1985]. For sea ice, we assume a constant salinity of 8‰ and a constant

density of $0.90Mg/m^3$. In a similar manner to chapter 3, we will also assume that there is a linear temperature profile in the ice. In the ocean, we will for simplicity neglect vertical variations in the properties of sea water and consider it as one homogeneous layer. Also, we will apply 16 streams in the atmosphere and 28 streams in the ice and ocean in most of the following computations. This will provide a computational accuracy better than 1%.

4.1.1 Spectral Distribution of Light in Sea Ice and the Underlying Ocean

Using the atmosphere, sea ice and ocean models described above, Figure 4.1 shows the computed spectral distribution of light at different levels in the ice and in the ocean respectively. The ice is assumed to have a thickness of 2.0 m and a surface temperature of $-15^\circ C$. The spectral distribution of PAR incident at the top of the atmosphere is from Nicolet [1989] and the solar elevation is specified to be 30°.

In the right panels of Figure 4.1, a layer of low-level stratiform cloud has been included in the atmosphere, a condition which is known to be persistent and extensive in the Arctic in the summer [*Herman and Curry*, 1984; *Tsay and Jayaweera*, 1984]. The cloud model is same as that used in Figure 3.6 of Chapter 3.

Snow cover is another prevalent feature in the high latitude oceans. Based on field observations, new snow has a smaller grain size and an appreciably lower density than melting old snow. We specify a mean grain radius of 100 μm and density of 0.2 Mg/m^3 as representative of new snow, and a grain radius of 1000 μm and a density of 0.40 Mg/m^3 as representative of melting old snow. The simulated downwelling irradiance at the ice base for different snow thicknesses is shown in Figure 4.2. The same atmosphere, sea ice and ocean models used earlier are used here, but the ice thickness is specified as 1.0 m. Figure 4.2 shows that
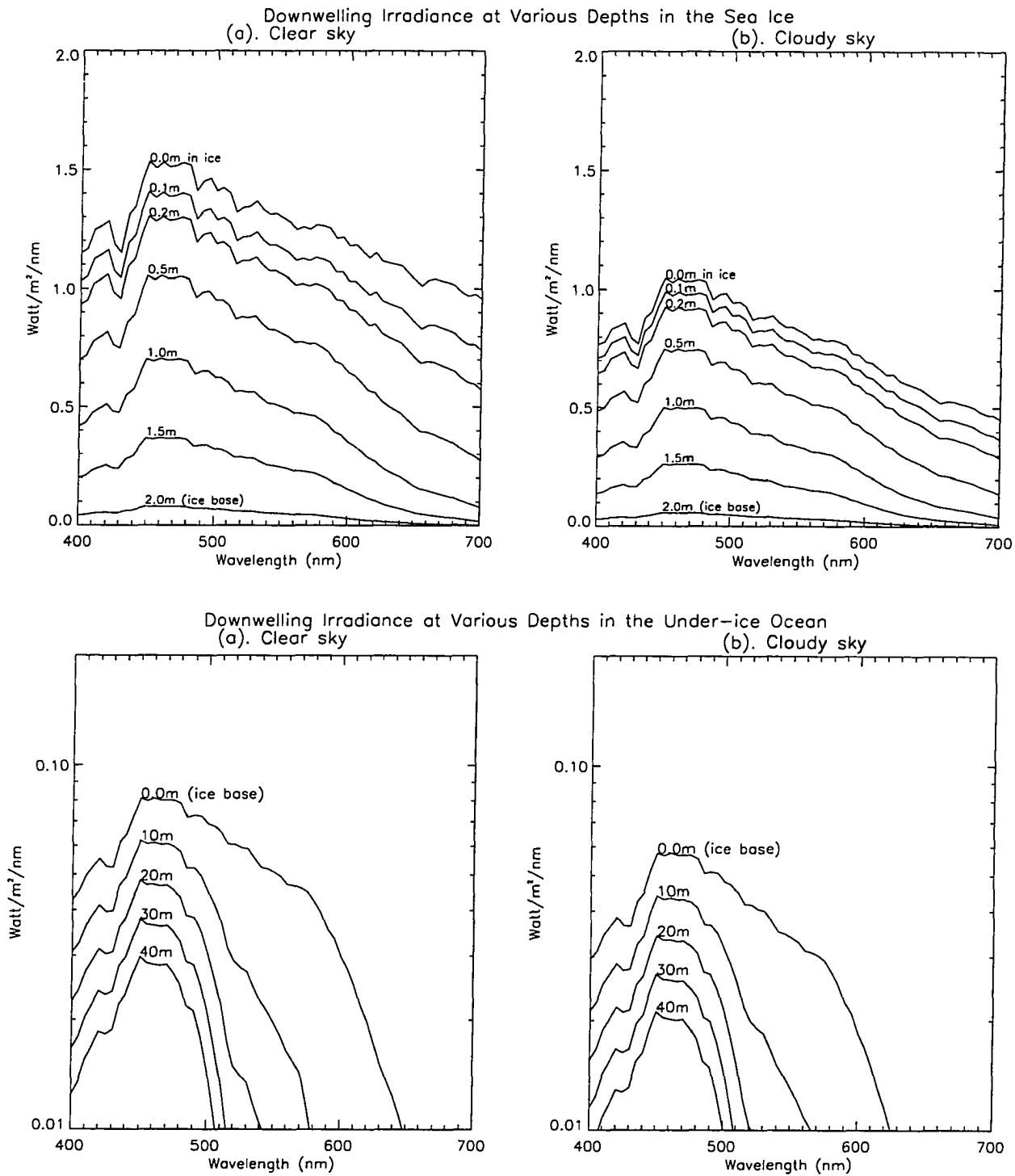
Figure 4.1 The spectral distribution of downwelling irradiance at various depths in the sea ice and ocean for clear skies and cloudy skies respectively. Ice thickness is specified to be 2.0 m, salinity $8\%_0$, density 0.9 Mg/m^3 and solar elevation 30° .

(a). New snow

(b). Old snow
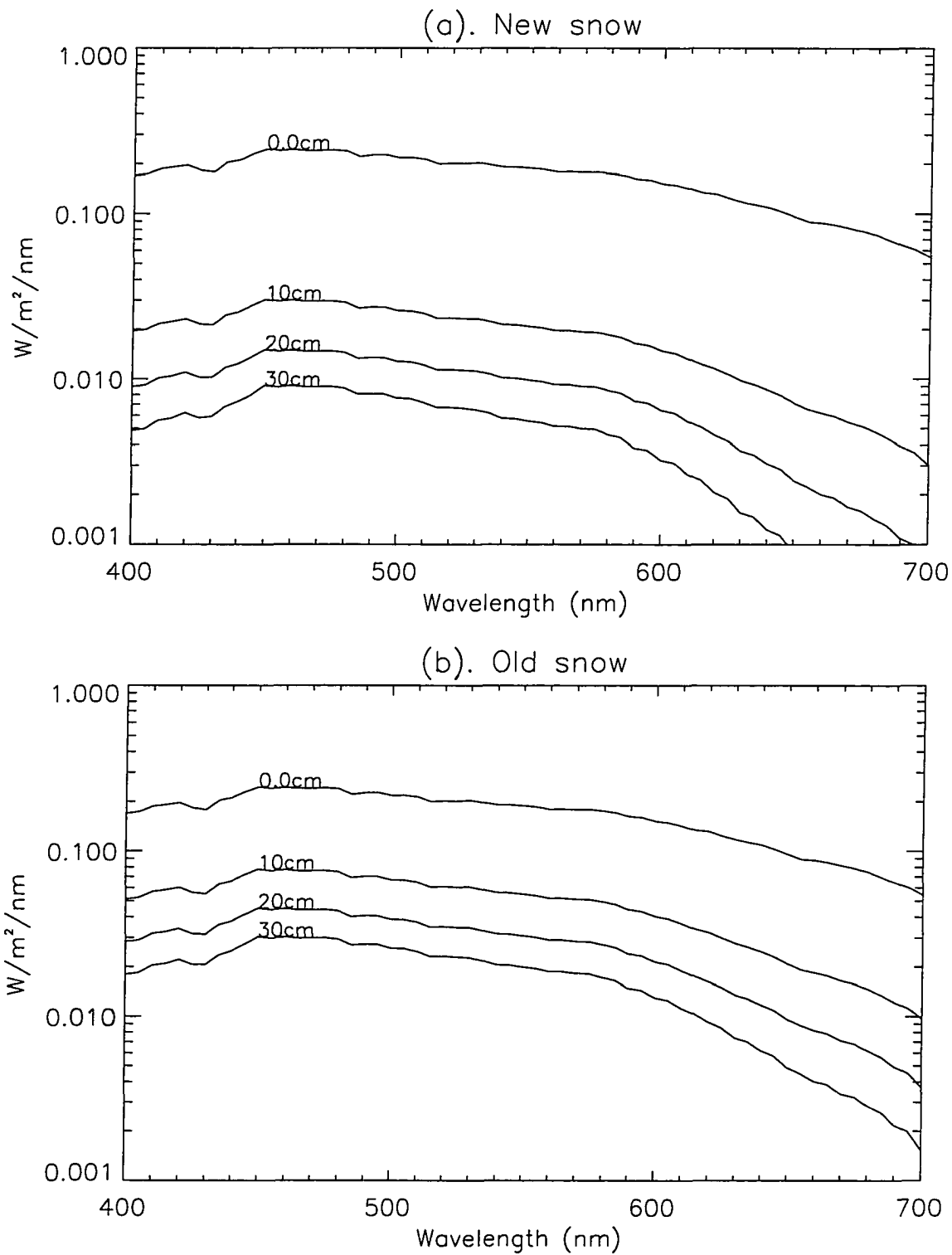
Figure 4.2 The spectral distribution of downwelling irradiance at the ice base as affected by the thickness and type of snow cover on the surface. The ice thickness is taken to be 1.0 m and the skies are assumed to be clear. The values on each line denote the snow thickness .

the snow significantly reduces the light availability under the ice, especially for the new snow. Only 10 cm of new snow can reduce the irradiance at the ice base by a factor of 10. Because of the small grain size, new snow efficiently scatters light back to the atmosphere.

Ice algae has been shown to have a important impact on light transmission into the ocean [SooHoo et al., 1987; Arrigo et al., 1991]. Including a layer of algae in the lowest 40 cm of ice, Figure 4.3 shows the downwelling irradiance at the ice base for four different chlorophyll a concentrations (0, 100, 250 and 500 mg/m^3). The results indicate that the presence of algae not only reduces the light transmission, but it also significantly changes the spectral distribution of light entering the ocean. The spectral alteration of the transmitted light is well anti-correlated with the spectrum of the chl a absorption coefficient for sea ice microalgae (the dotted curve in Figure 4.3), which exhibits two big absorption peaks at 670 nm and 430 nm respectively.

4.1.2 The Effects of Clouds, Snow and Ice Algae on the Seasonal Variation of PAR in Sea Ice and the Ocean

Although the daily solar radiation at high latitudes experiences a greater seasonal variability than at lower latitudes, the pattern of temporal change of daily PAR is similar to the pattern of noon value evolution. Figure 4.4 shows the temporal variation of the total PAR as calculated at $78°N$ at local noon under a clear sky and a cloudy sky respectively. The same atmosphere, cloud, sea ice and ocean models as above have been adopted and the surface is assumed to be snow-free. The right panels demonstrate the corresponding decrease of total PAR relative to the clear sky conditions at three levels due to the presence of the cloud. The results show that a decrease of PAR up to 40% at the ice base can occur as the
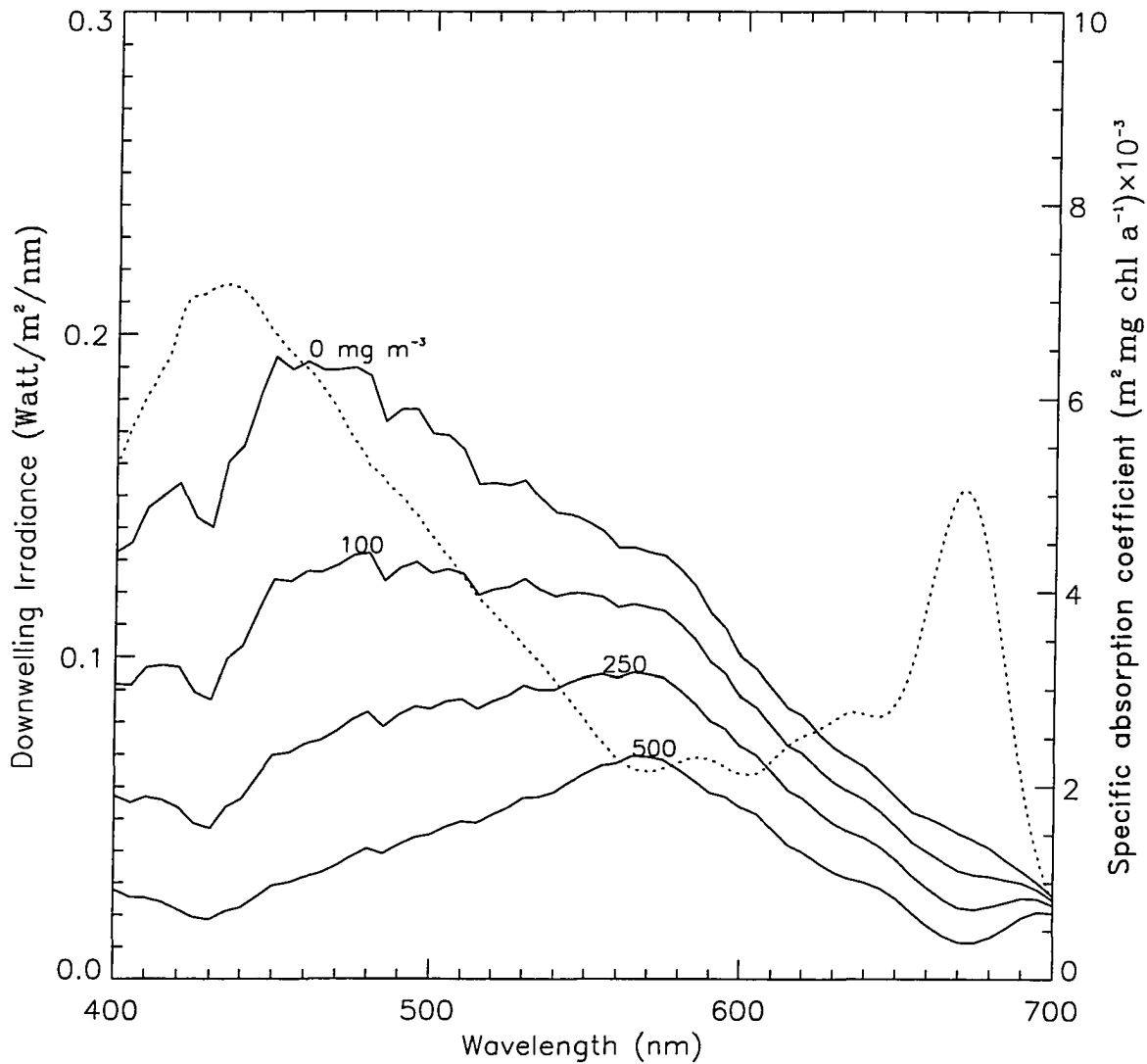
Figure 4.3 The downwelling irradiance entering the ocean under a 1.0 m thick sea ice sheet for various ice algae concentrations. The algae is assumed to occur in the lowest 40 cm of the ice. The values on each line represent the chl a concentration (mg/m^3). The dotted line represents the chl a specific absorption coefficient for sea ice microalgae .

result of the Arctic stratus cloud used here. Although the absolute decreases (the vertical distances between the two curves in the left panels) at every level show a maximum at the summer solstice, the relative changes as shown in the right panels show a minimum at this time. This is caused by different solar elevations at noon on different days.

Similarly, Figure 4.5 shows the downwelling PAR at the base of the same 1.0 m ice at $78°N$ local noon for clear skies and four different snow and ice conditions: (i) without snow on the ice surface or algae in the ice, conditions which represent an upper limit; (ii) snow-free but with a layer of algae with a chl a concentration of 100 mg/m^3 in the lowest 40 cm of ice; (iii) with a 10 cm layer of melting old snow and (iv) with a 10 cm layer of new snow. The algae and snow models are the same as discussed earlier. The results show that 10 cm of new snow can reduce the PAR available at the ice base by 90%. The independence of the relative change caused by algae to the day number or the solar elevation is due to the fact that only the absorption is considered for the ice algae and the direct component of the solar radiation is negligible in the algae layer.

Acting as the only significant absorptive gas affecting the transfer of PAR in the atmosphere, ozone affects the availability of PAR to the marine microbial communities existing under sea ice covers. Here we take the total column ozone abundance of 350 DU as normal. Figure 4.6 shows the seasonal variation of PAR at two different levels and three different ozone depletion scenarios. The right panels show the corresponding increases of PAR for the ozone depletion scenario of 175 DU (50% less than normal). Depending on the solar elevation, a 50% ozone depletion yields an increase in total PAR at the ice base as well as at 10 m depth in the ocean of less than 4%, a minor change compared with the impacts of clouds, snow and algae as shown above.

Figure 4.7 shows the downwelling PAR at the ice base as a function of the ice

Incident PAR on Surface

Relative Decrease of PAR

Downwelling PAR at Ice Base

Downwelling PAR at 10m in Ocean
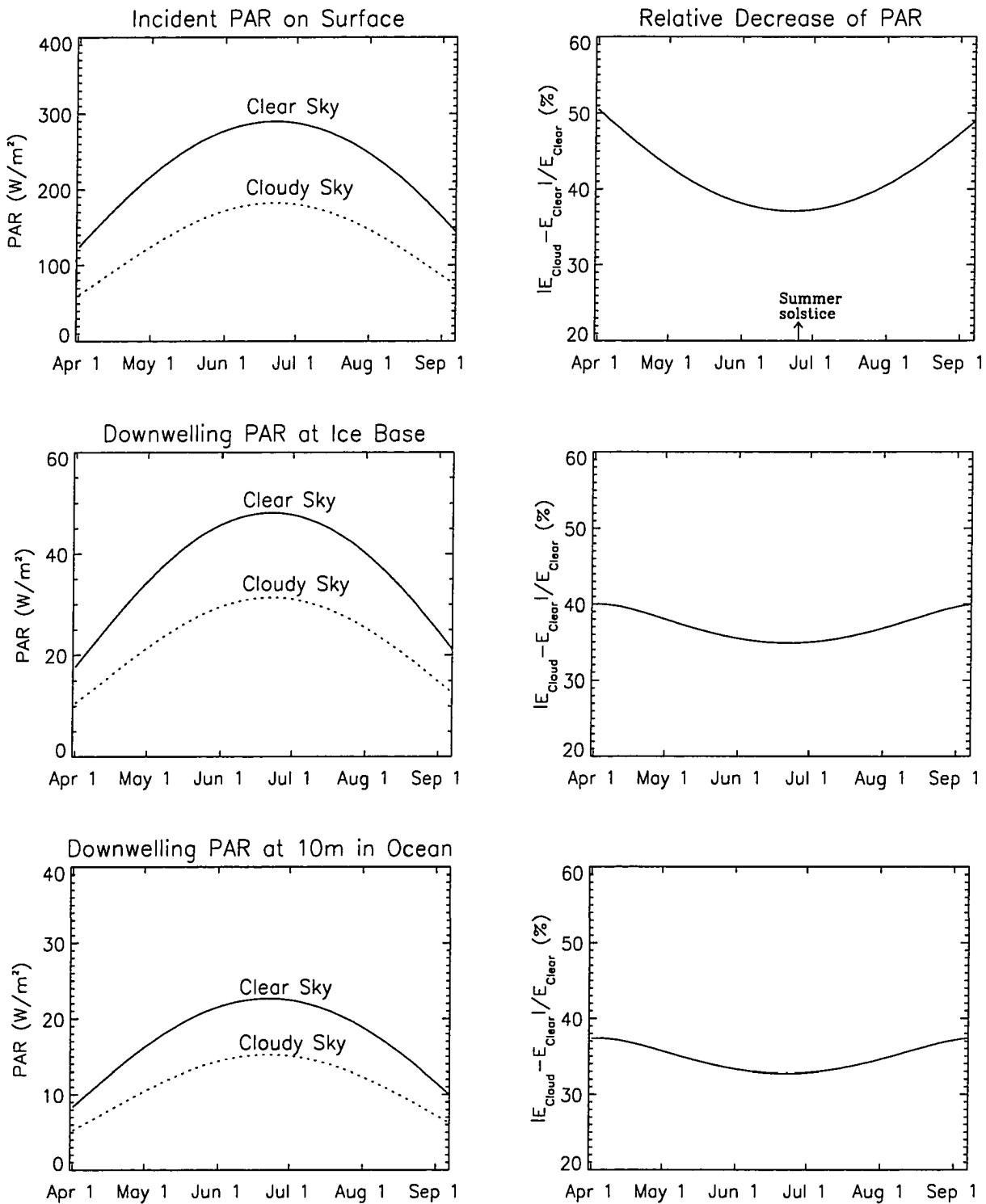
Figure 4.4 Seasonal variation of total PAR at the surface, at the base of a 1.0 m thick ice sheet and at 10 m depth in the ocean under clear skies and cloudy skies respectively. The right panels demonstrate the corresponding relative decrease due to the presence of cloud. Values are derived at latitude $78°N$ at local noon .

Downwelling PAR at Ice Base

78°N
Noon

Clear

With Algae

Old Snow

New Snow

Relative Decrease of PAR

New Snow

Old Snow

With Algae

Summer
solstice
↑
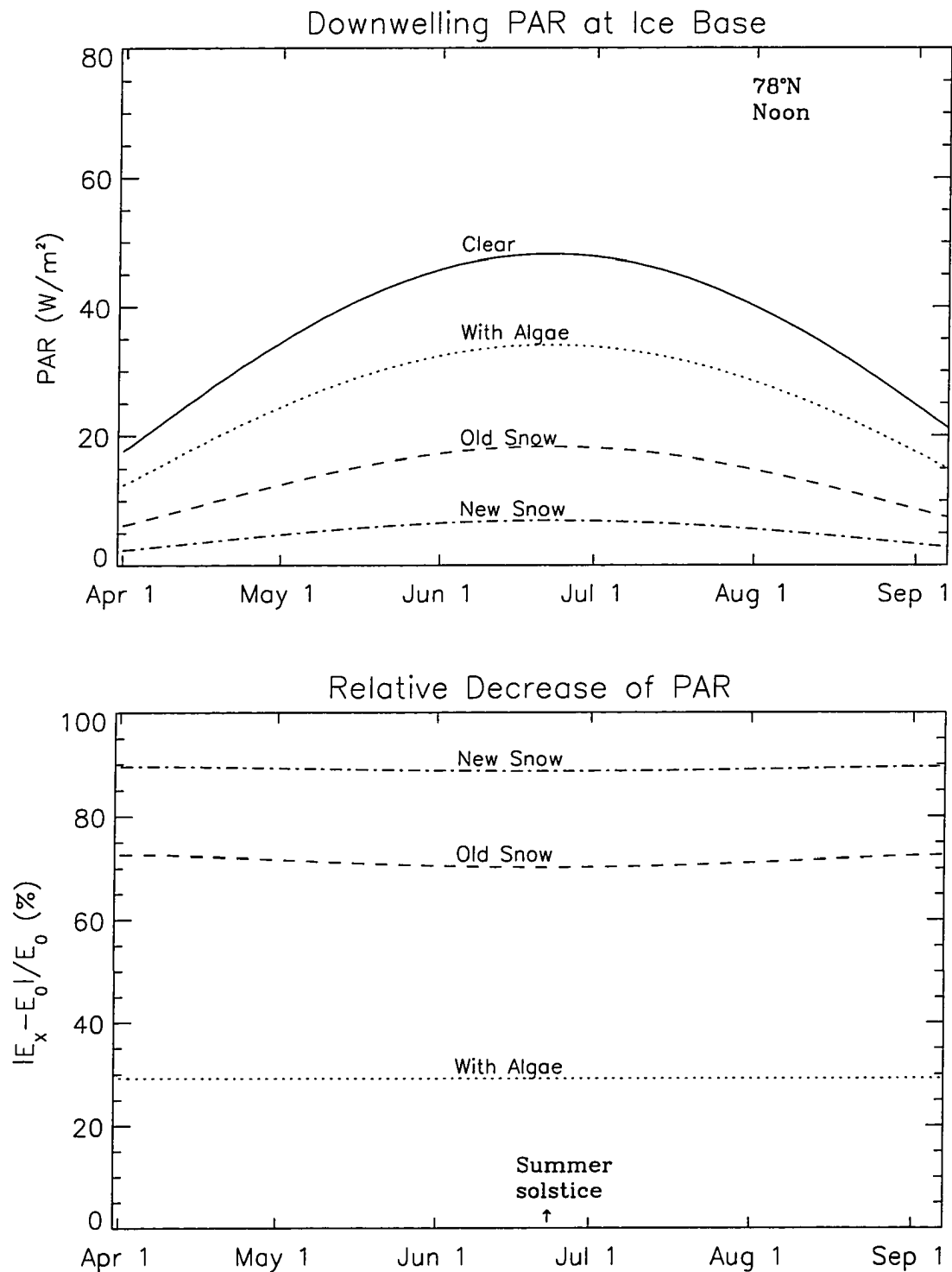
Figure 4.5 Total downwelling PAR entering the ocean under a 1.0 m of ice for four different conditions: (i) clear sky without snow on the ice surface and algae in the ice, hence representing an upper limit; (ii) including a layer of algae with chl a concentration of 100 mg/m^3; (iii) with a 10 cm layer of old snow and (iv) with a 10 cm of new snow. The lower panel shows the corresponding decrease of PAR relative to the "clear" case .
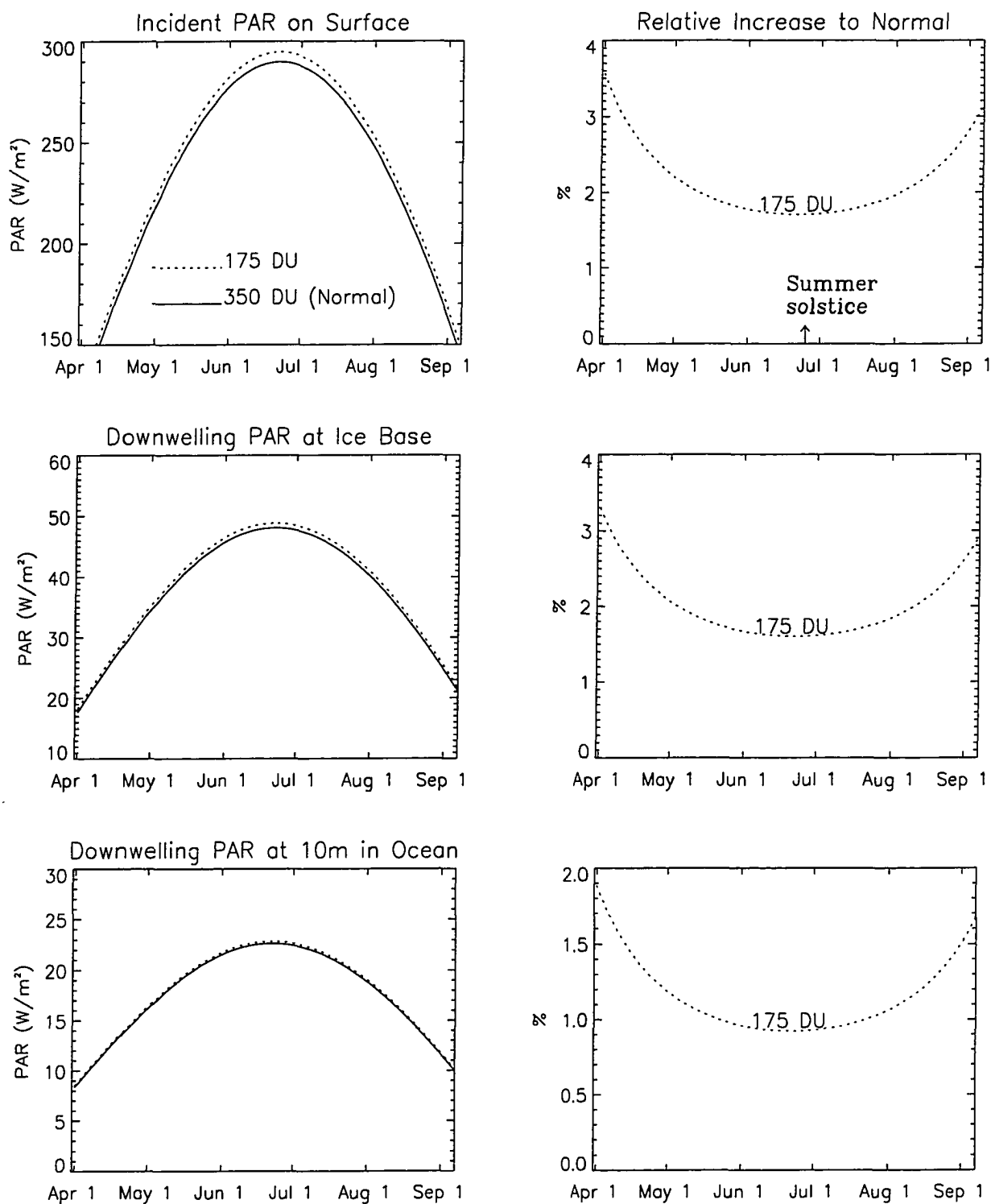
Figure 4.6 Similar to Figure 4.4, but showing the ozone effect under clear skies. The total column ozone abundance of 350 DU is taken as normal. The increases of total PAR relative to normal values are shown in the right figures for a ozone depletion scenario of 175 DU (50% less than normal) .

(a). Clear sky

Solar Elevat.
———— 50°
– – – – 20°

W/m²

Ice Thickness (m)

(b). Cloudy sky

Solar Elevat.
———— 50°
– – – – 20°

W/m²

Ice Thickness (m)

Figure 4.7 Total downwelling PAR entering the ocean as a function of ice thickness for various solar elevations .

thickness for different solar elevations under a clear sky and a cloudy sky respectively. Obviously, ice thickness has a significant effect on the light transmission into the ocean, especially when the ice is thin. Higher solar elevations enhance this ice thickness dependence. Not only do clouds drastically reduce the PAR entering the ocean, but they also reduce the sensitivity of the variation of the under-ice PAR to the ice thickness. This is due to the relative increase in the diffuse irradiance (as compared to the direct component) for cloudy conditions.

4.2   Comparison With Measurements

Using the coupled radiative transfer model, we have simulated a set of irradiance field measurements taken in an Antarctic ice floe [Quakenbush, 1994], which had a thickness of 1.24 m. The irrradiance measurements in the ice were taken at depths of 20, 40, 60, 80, 100, and 120 cm. Sky irradiances were also measured simultaneously to monitor changes in the light source with time and thereby allow for calculation of extinction values. The solid lines in Figure 4.9 represent the measured irradiance at different depths of the ice normalized by the irradiance at the depth of 20 cm. The dotted lines are the modeled results. We use these normalized values for comparison with modeling because (i) the measured data have not been calibrated to the irradiance, so they only represent relative magnitudes; and (ii) the distribution of the incident light on the ice surface has little effect on these no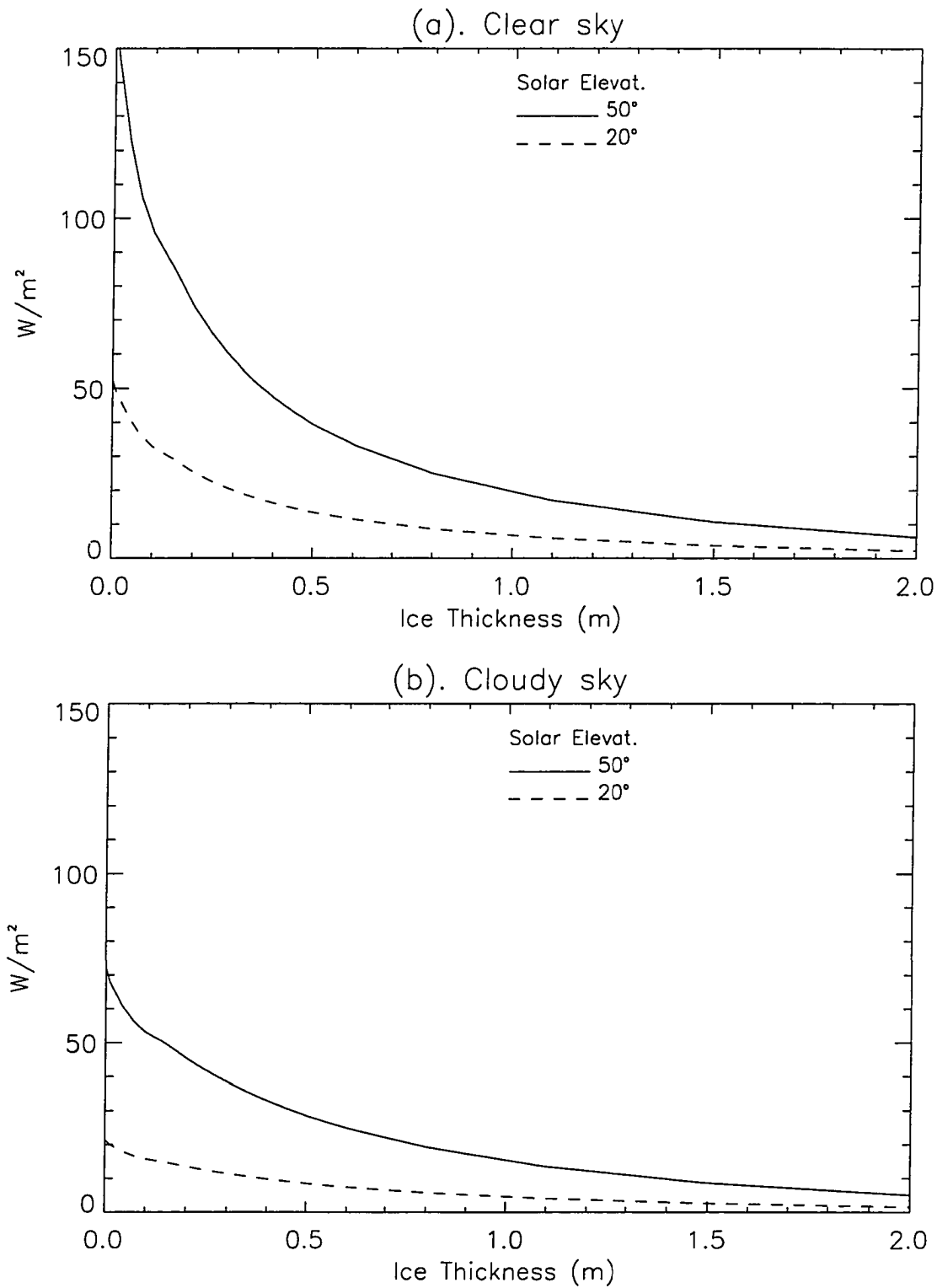rmalized values, because the radiation below a depth of 20 cm in the ice could be considered as diffusive. Therefore, we can assume a diffuse incident light field on the ice surface of arbitrary magnitude to model these normalized values and extinction coefficients. The salinity and temperature profiles utilized in the model for input are shown in Figure 4.8 and are based on in-situ measurements.

The absorption peaks at 670 and 430 nm in the measured spectral irradiances
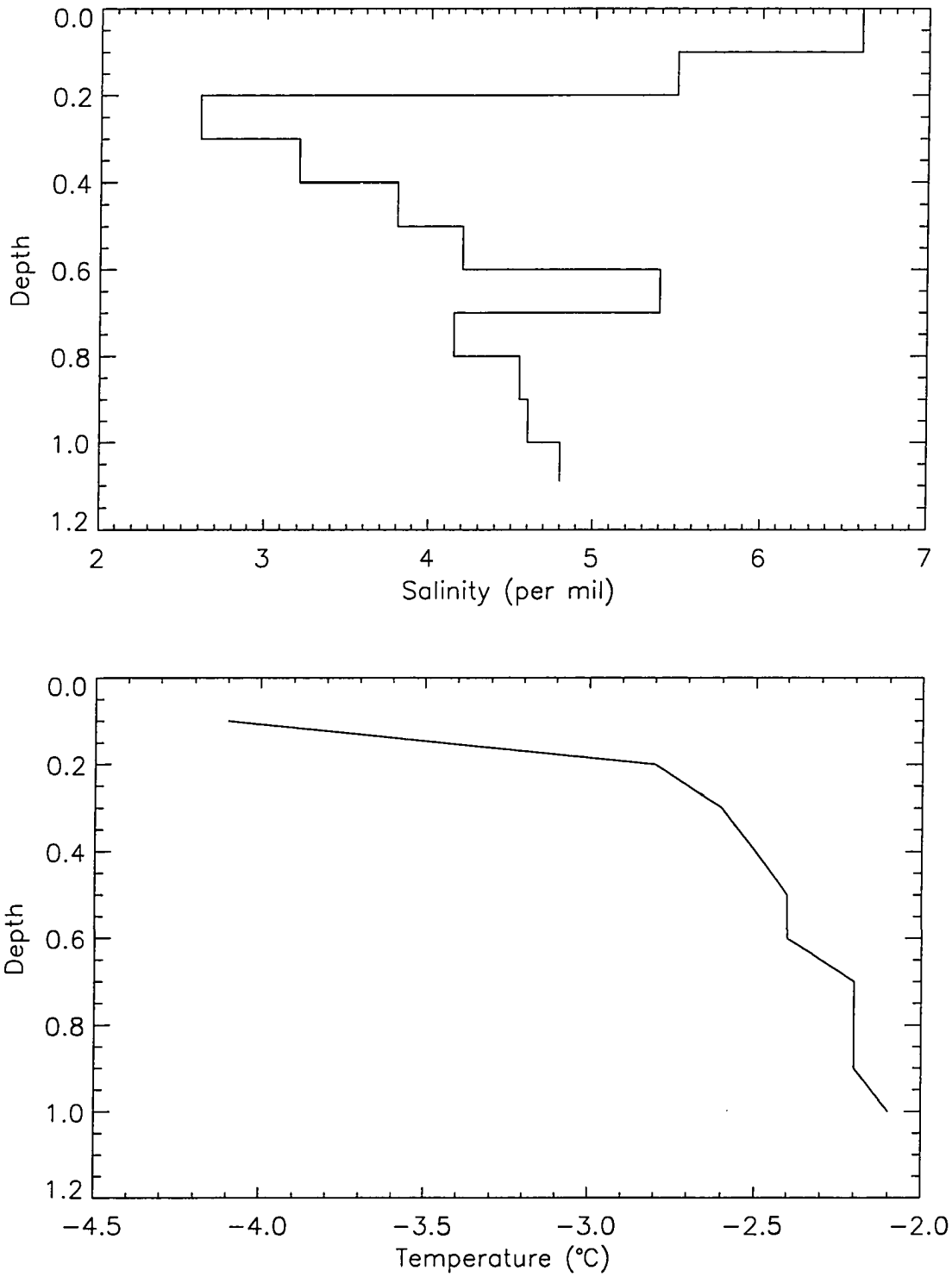
Figure 4.8 Measured profiles of salinity and temperature in the ice floe. This ice sheet has a thickness of 124 cm.
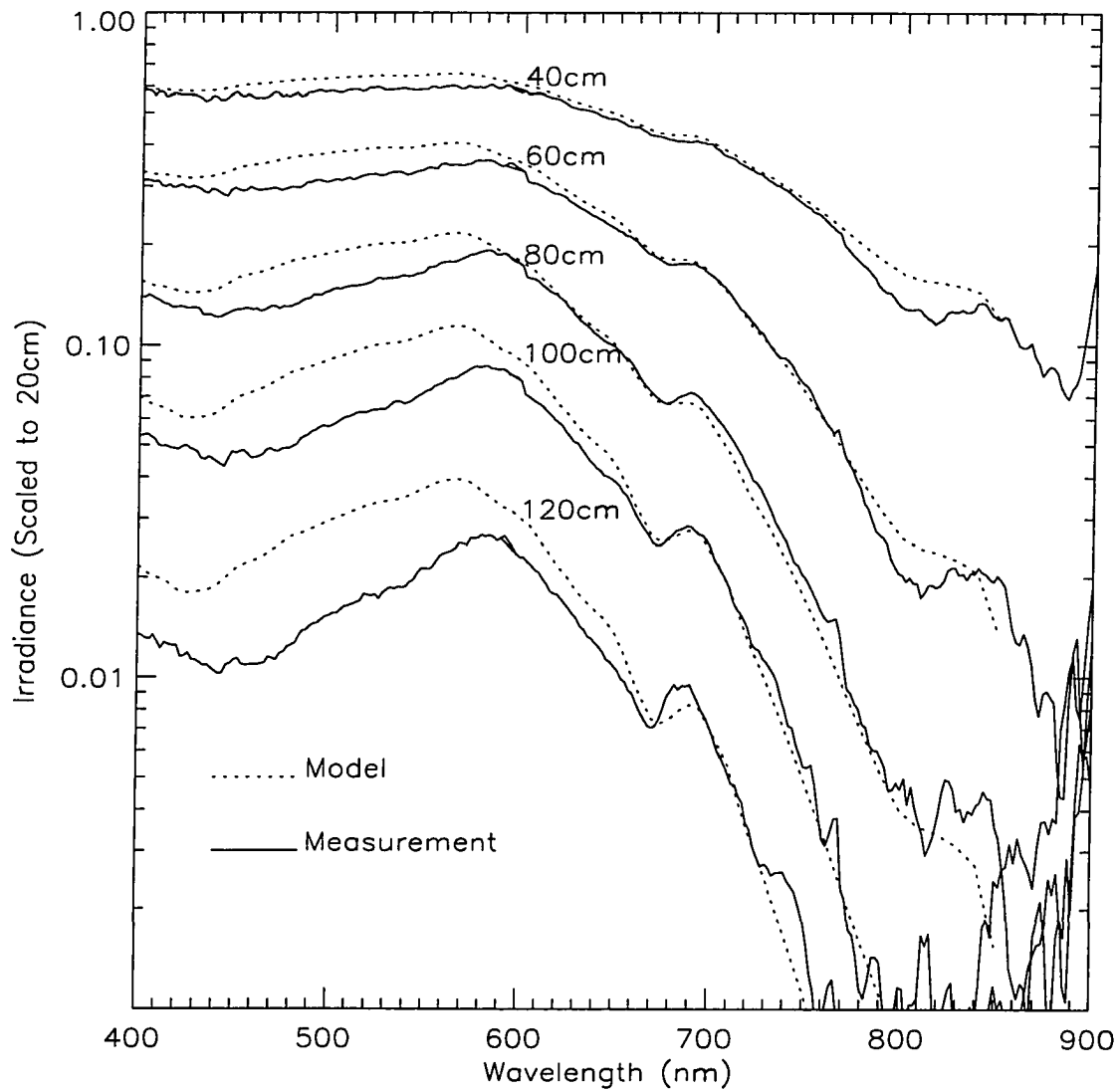
Figure 4.9 Comparison of measured spectral irradiances at various depths (normalized to values at a depth of 20 cm) with model calculations.
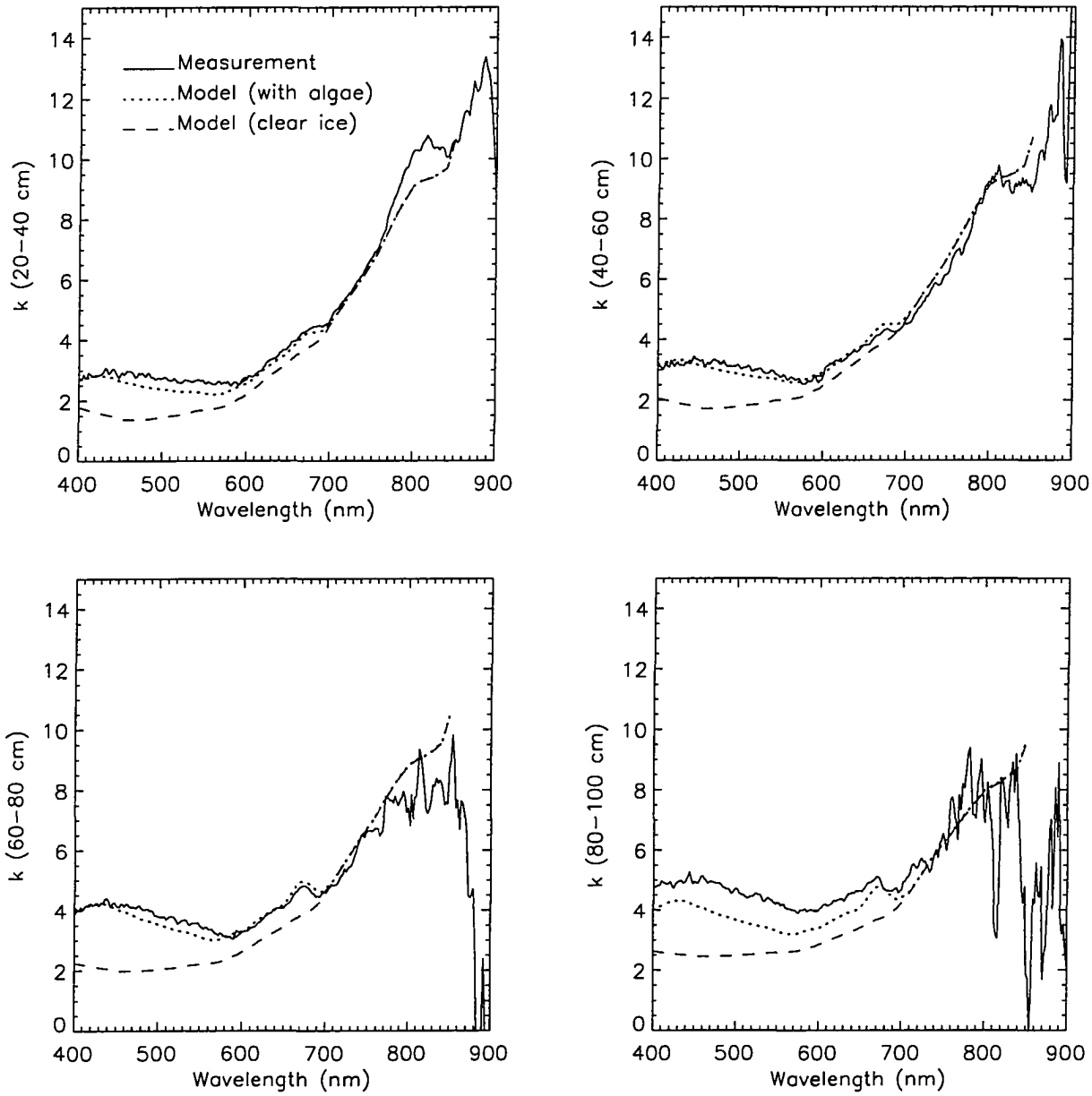
Figure 4.10 Comparison of measured extinction cofficients for various ice layers with model calculations.

indicate that algae exists in the ice. Unfortunately, measurements of the algae concentration were not made. Therefore we have assumed a chlorophyll concentration of 10 mg/m^3 in the upper 80 cm of the ice and of 40 mg/m^3 in the bottom 40 cm of the ice. The extinction values for different layers from measurement and modeling are shown in Figure 4.10. The dashed line represents the extinction in clear ice (no algae included). Results show that if the algae is ignored, good agreement can be achieved only at wavelengths larger than 700 nm, where algae absorption is small. To obtain better agreement, algae absorption has to be taken into account. The differences between the measurement and the modeling in the short wavelengths in the deeper layers (depth > 80 cm) show that there is absorption by material other than ice algae which we have not taken into account. These material might be detritus and mineral-like particulates, which have higher absorption at short wavelengths and lower absorption at red wavelengths.

4.3   Summary

The transport of the photosynthetically active radiation in the atmosphere, snow, ice and ocean column has been studied by the radiative transfer model developed for the coupled atmosphere, ice and ocean system. The modeling results show that clouds, snow and ice algae all have significant effects on the transport of light in the sea ice and ocean. A 10 cm layer of new snow is sufficient to cause a 90% reduction in the total PAR available to the marine biological communities under the ice. The occurrence of ice algae also drastically changes the spectral distribution of light transmitted through the ice. Although it is acting as the main absorptive gas in the spectral region of PAR, ozone in the atmosphere has a negligible effect on the light available to the biosphere under the ice when compared with the effects of clouds, snow and algae. A 50% ozone depletion would increase the total PAR

by less than 4% at any level in the ice and ocean. The total PAR transmitted through the ice is sensitive to ice thickness, especially when the ice is thin and the solar elevation is high. Clouds not only reduce the PAR amount in the ocean, but also reduce the sensitivity of the available PAR under the ice to variations in ice thickness.

Model simulation of the measured irradiance and extinction in the ice shows good agreement at the red wavelengths. To obtain good agreement with observation at shorter wavelengths, especially in the PAR spectral region, the absorption by impurities in sea ice, such as ice algae and non-algae particulates, has to be taken into account.

Chapter 5

Discussion and Conclusion

To study the radiative transfer in the coupled atmosphere-sea ice-ocean system consistently, a comprehensive radiative transfer model for this coupled system has been theoretically formulated and numerically implemented. The first part of this thesis presented the theoretical work, which extends the discrete ordinate method to solve the radiative transfer equation pertinent to a coupled system consisting of strata with different refractive indices, such as the atmosphere-ocean system or the atmosphere-sea ice-ocean system. The refraction and total reflection at the interface of the two strata have been taken into account by assigning different numbers of angular quadrature points (discrete ordinates or "streams") in each stratum. Self-consistency tests show that the solution conserves energy and is both reliable and efficient. The solution was applied to the atmosphere-ocean system and the results are compared with several similar radiative transfer models which solve the radiative transfer equation using different methodologies. A comparison of results shows good agreement and confirms that the solution for the coupled system developed here has correctly incorporated the mathematical representations of the relevant radiative processes (absorption and multiple scattering) and of the effects of the reflection and refraction at the air-water boundary.

113

Future work on the theoretical aspects of the radiative transfer model for the coupled system include: (i) incorporating surface roughness, so that the model can simulate wind-generated waves on the ocean surface; (ii) extending the model to deal with changes in index of refraction between all layers, so that it becomes feasible to study radiative transfer within media in which the index of refraction changes continuously throughout the medium; (iii) including the computation of the inelastic scattering effects to treat phenomena such as Raman scattering; and (iv) considering the effects of polarization.

In the second part of the thesis, the solution of the radiative transfer equation for non-uniformly refracting media has been applied in the atmosphere-sea ice-ocean system and used to study the solar energy balance and light transport in this coupled system. The multiple scattering and absorption by atmospheric molecules, clouds, snow and sea water, as well as the brine pockets and air bubbles trapped in sea ice, has been rigorously taken into account. The model considers the ice and ocean just as additional "atmospheric" layers with different optical properties. Therefore, the surface albedo can be calculated consistently from the calculated upward and downward fluxes at the surface. This coupling also provides a suitable method to investigate the radiative interactions between the atmosphere, clouds, snow, sea ice and ocean self-consistently, as well as to identify the most important physical parameters affecting radiative transfer processes in the whole system. Modeling results have shown different sensitivity to and dependence of the partitioning of solar energy in the coupled system on those parameters, such as salinity and density of the ice, the microphysics and height of clouds, as well as snow conditions. Some important findings from modeling are listed as following:

- Most of the radiative energy absorbed by sea ice occurs in a very thin top layer of the ice. Under clear sky conditions, only 10 cm of the top layer of ice can absorb more than 50% of the total solar radiation deposited in the

entire system.

- In sea ice it is the scattering by inclusions, especially the air bubbles, in a few centimeters of the uppermost layer that plays a vital role to the solar energy absorption and partitioning in the whole system. Enhanced scattering in this top layer will not only increase backscattering to the atmosphere, but it also increases the fraction absorbed in this top ice layer itself and decreases the radiation penetrating to the deeper layers of the ice and into the ocean.

- Because air bubbles scatter light much more efficiently than brine pockets, the radiative absorption is more sensitive to air volume variations than to brine volume variations.

- Increasing the ice thickness would result in not only an increase of solar absorption in the ice and a corresponding decrease in the ocean, but also a decrease of the absorption in the entire system. On the other hand, the absorption in the atmosphere is not sensitive to the ice thickness. However, the total absorption in the entire system remains almost constant once the ice thickness exceeds about 70 cm.

- Both clouds and snow reduce the solar energy absorption in the ice and in the ocean, as well as in the entire atmosphere-sea ice-ocean system.

- The absorption of solar radiation in sea ice shows a greater sensitivity to the cloud microphysics than the absorption in the atmosphere and in the ocean. The absorption in the entire system will increase as the equivalent radius of cloud droplets increases and decrease as the liquid water content increases.

- Different from the case in atmosphere, the absorption in sea ice and ocean is not sensitive to cloud height.

- Clouds not only change the energy disposition in the system, they also reduce the sensitivity of the energy disposition in each layer to the ice and snow

thickness change. However, they increase the sensitivity of the surface albedo to the ice or snow thickness variation.

- Surface albedo is determined by approximately 10 cm of the uppermost layer of snow for a snow covered surface and by about 50 cm of the uppermost layer of ice for a bare ice surface.

- Generally, increasing cloud thickness will increase the surface albedo, unless the solar elevation is low and the cloud is thin. Of all the possible cases, the combination of new snow and thick clouds yields the highest surface albedo.

- Compared with the effects of clouds, snow and algae, the effect of ozone in the atmosphere on the light available to the biosphere under the ice is negligible.

- The occurrence of ice algae has significant effects on the light transport in sea ice and ocean and on the spectral distribution of light transmitted through the ice.

The importance of sea ice properties to the solar energy absorption in the ice and to the energy distribution in the overall system is clearly demonstrated. However, existing observational data on ice properties is not adequate for accurate modeling; for example, the volume fraction of air bubbles and brine pockets as well as their size distribution in various ice types under a variety of conditions is not well known. Therefore, the present treatment of the profile properties of the different thicknesses and ages of sea ice is crude and, in addition, a linear temperature profile for all ice thicknesses has been assumed. It is important that improved parameterizations of sea ice property profiles for different ice types be developed in the future in order to make better predictions of radiative energy deposition.

Observations in the Arctic have shown that significant ice crystal nucleation occurs in the atmosphere at temperatures as high as $-15°$ to $-20°C$ [Curry, 1990].

Therefore, the parameterization of ice cloud properties should be included in future models. To be more realistic, property profiles for the Arctic atmosphere, such as temperature and humidity, have to be compiled based on available data sets from stations in the Arctic region.

The coupling that we have considered is purely radiative and does not allow the radiation to alter the snow/ice/cloud properties resulting in changes which could then affect subsequent radiative transfer. To investigate interactions and feedbacks in the polar environment, the present radiative transfer model should be coupled to models treating the evolution of ice, snow, and clouds. An initial step in accomplishing this requires that the computational efficiency of the present model be improved, so that it can be coupled to long-term models which consider property profile changes and radiative flux balances over longer time scales.

Appendix A

Derivation of the Reflectance and the Transmittance for the Invariant Intensity (I/n^2) at the Interface of two Media with Different Indices of Refraction

When a lightwave encounters the interface of two media with different indices of refraction, specular reflection and refraction occur. The Fresnel equations reveal the amplitude relationship between the incident, the reflected and the refracted waves with plane polarization. Based on the basic Fresnel equations, the reflectance and transmittance of the irradiance for a parallel beam of a plane polarized wave can be derived as [Hecht, 1990]

$$R_\perp = r_\perp^2 \qquad\qquad\qquad\qquad \text{(A.1a)}$$

$$R_\parallel = r_\parallel^2 \qquad\qquad\qquad\qquad \text{(A.1b)}$$

118

$$T_\perp = \left(\frac{n_t \cos \theta_t}{n_i \cos \theta_i} \right) t_\perp^2 \tag{A.1c}$$

$$T_\| = \left(\frac{n_t \cos \theta_t}{n_i \cos \theta_i} \right) t_\|^2 \tag{A.1d}$$

where r denotes the amplitude reflection coefficient, and t is the amplitude transmission coefficient. The subscript '$\|$' represents the decomposed component parallel to the plane of incidence, and '$\perp$' denotes the component perpendicular to it. θ_i and θ_t are the angles of incidence and transmittance respectively, and n_i and n_t denote the indices of refraction for the two media.

If we define an azimuthal angle ϕ as the angle between the plane of vibration and the plane of incidence, then for a parallel beam or plane wave of incident natural light which is unpolarized, the reflectance and the transmittance should be obtained by averaging the results pertaining to polarized light over the 2π azimuthal angle,

$$\begin{aligned} R &= \frac{1}{2\pi} \int_0^{2\pi} R_\| \cos^2 \phi d\phi + \frac{1}{2\pi} \int_0^{2\pi} R_\perp \sin^2 \phi d\phi \\ &= \frac{1}{2}(R_\| + R_\perp) \end{aligned} \tag{A.2a}$$

Similarly, the transmittance for natural light can be expressed as

$$T = \frac{1}{2}(T_\| + T_\perp) \tag{A.2b}$$

Substituting equations (A.1a)-(A.1d) into equations (A.2a) and (A.2b), and making use of the expression for the amplitude coefficients $r_\perp$, $r_\|$, $t_\perp$ and $t_\|$, we may rewrite R and T as

$$R = \frac{1}{2} \left\{ \left(\frac{\mu_i - n\mu_t}{\mu_i + n\mu_t} \right)^2 + \left(\frac{\mu_t - n\mu_i}{\mu_t + n\mu_i} \right)^2 \right\} \tag{A.2c}$$

$$T = 2n\mu_i\mu_t \left\{ \left(\frac{1}{\mu_i + n\mu_t} \right)^2 + \left(\frac{1}{\mu_t + n\mu_i} \right)^2 \right\}. \tag{A.2d}$$
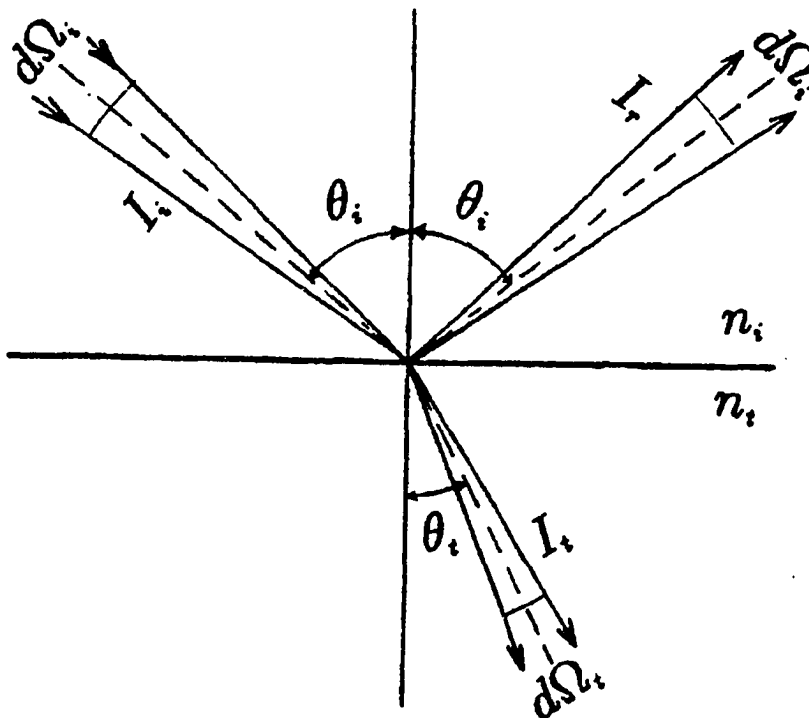
Figure A.1 Reflection and refraction of a cone of light at the interface of two media with different refractive indices..

Here we have used Snell's law, $n = n_t/n_i = \sin\theta_i/\sin\theta_t$, and denoted $\mu_i = \cos\theta_i$ and $\mu_t = \cos\theta_t$.

In order to derive the reflectance and transmittance for the intensity (radiance), we consider a cone of incident lightwaves instead of a parallel beam. As illustrated in Figure A.1, I_i, I_r and I_t are the incident, reflected and transmitted intensities respectively. A cone of incident light within an infinitesimal solid angle $d\Omega_i$ will shrink or expand (depending on the value of the relative index of refraction of the two media) to the solid angle $d\Omega_t$ after passing the interface, and their relationship

can be derived by making use of Snell's law,

$$\frac{d\Omega_t}{d\Omega_i} = \frac{2\pi \sin\theta_t d\theta_t}{2\pi \sin\theta_i d\theta_i}$$

$$= \frac{\mu_i}{n^2\mu_t} \tag{A.3}$$

Applying the definition of R and T for the irradiance to the configuration depicted in Figure A.1 and making use of equation (A.3), we find that

$$T = \frac{I_t \cos\theta_t d\Omega_t}{I_i \cos\theta_i d\Omega_i} = \left(\frac{I_t}{n_t^2}\right) \Big/ \left(\frac{I_i}{n_i^2}\right) \tag{A.4a}$$

$$R = \frac{I_r \cos\theta_i d\Omega_i}{I_i \cos\theta_i d\Omega_i} = \left(\frac{I_r}{n_i^2}\right) \Big/ \left(\frac{I_i}{n_i^2}\right) \tag{A.4b}$$

Equations (A.4a) and (A.4b) show that if we define the transmittance and reflectance with respect to the invariant intensity, I/n_{abs}^2 (n_{abs} is the absolute index of refraction at the location where I is measured), instead of the actual intensity, then the expressions for the reflectance and transmittance will have the same forms as for the parallel light beam. Such a definition has the additional advantage of satisfying reciprocity for the lightwave propagating in the opposite direction and also satisfying the complementarity of the reflectance and transmittance. If we denote the reflectance and transmittance specified by equations (A.2c) and (A.2d) by $R(-\mu_i, n_t/n_i)$ and $T(-\mu_i, n_t/n_i)$ for downwelling incidence, and by $R(\mu_t, n_i/n_t)$ and $T(\mu_t, n_i/n_t)$ for upwelling incidence, then the reciprocity relationship can be expressed as

$$R(\mu_t, n_i/n_t) = R(-\mu_i, n_t/n_i) \tag{A.5a}$$

$$T(\mu_t, n_i/n_t) = T(-\mu_i, n_t/n_i). \tag{A.5b}$$

Also, it is easy to show the complementarity of the reflectance and the transmittance

$$R + T = 1.0. \tag{A.6}$$

Appendix B

Structure of the Coefficient Matrix

The coefficient matrix for Equation (2.17) constitutes a diagonal band matrix, which has numerous elements that are zero in the upper-right and lower-left corners. When the number of layers or streams is large, so will the number of elements that are zero. This feature can be used to obtain an efficient solution of the matrix equation. Linear equation solvers exist, such as LINPAK, that are specifically designed to treat banded matrices. However, the band width or the number of "zero-element" diagonals in the upper-right and lower-left corners of the matrix have to be specified. In the usual case in which there is no change in index of refraction across layer interfaces, so that the number of streams in each layer is the same, the band width is simply $6N - 1$ ($2N$ is the number of streams) [Stamnes and Conklin, 1984] and the number of diagonals containing only zero elements below and above the main diagonal is the same. This symmetry in structure is a consequence of using the same number of streams in every layer which is the

122

obvious choice for a medium with constant index of refraction. However, for the atmosphere-ocean system, additional streams are required to deal with the region of total reflection in the ocean resulting from the change in the refractive index across the atmosphere-ocean interface. In this case, we need to determine the relationship between the number of "zero-element" diagonals in the upper-right as well as lower-left corners and the number of layers and streams in the atmosphere (L_1, N_1) and ocean (L_2, N_2). Let's show some examples first:

1. For a two-layer system (1 layer of atmosphere and 1 layer of ocean) with 4 streams in the atmosphere and 6 streams in the ocean ($L_1 = 1$, $L_2 = 1$, $N_1 = 2$, $N_2 = 3$), the coefficient matrix will have the form

$$\begin{bmatrix} \# & \# & \# & \# & 0 & 0 & 0 & 0 & 0 & 0 \\ \# & \# & \# & \# & 0 & 0 & 0 & 0 & 0 & 0 \\ \# & \# & \# & \# & \# & \# & \# & \# & \# & \# \\ \# & \# & \# & \# & \# & \# & \# & \# & \# & \# \\ \# & \# & \# & \# & \# & \# & \# & \# & \# & \# \\ \# & \# & \# & \# & \# & \# & \# & \# & \# & \# \\ 0 & 0 & 0 & 0 & \# & \# & \# & \# & \# & \# \\ 0 & 0 & 0 & 0 & \# & \# & \# & \# & \# & \# \\ 0 & 0 & 0 & 0 & \# & \# & \# & \# & \# & \# \\ 0 & 0 & 0 & 0 & \# & \# & \# & \# & \# & \# \end{bmatrix}$$

where the label $\#$ represents any non-zero element in the matrix. This matrix has 4 "zero-element" diagonals in the lower-left corner, but only 2 "zero-element" diagonals in the upper-right corner. Obviously, the number

of "zero-element" diagonals above and below the main diagonal is not the same.

2. If we use three atmospheric layers ($L_1 = 3$) with 2 streams ($N_1 = 1$) and one ocean layer ($L_2 = 1$) with 6 streams ($N_2 = 3$), the coefficient matrix becomes

$$
\begin{bmatrix}
\# & \# & 0 & 0 & 0 & 0 & 0 & 0 & 0 & 0 & 0 & 0 \\
\# & \# & \# & \# & 0 & 0 & 0 & 0 & 0 & 0 & 0 & 0 \\
\# & \# & \# & \# & 0 & 0 & 0 & 0 & 0 & 0 & 0 & 0 \\
0 & 0 & \# & \# & \# & \# & 0 & 0 & 0 & 0 & 0 & 0 \\
0 & 0 & \# & \# & \# & \# & 0 & 0 & 0 & 0 & 0 & 0 \\
0 & 0 & 0 & 0 & \# & \# & \# & \# & \# & \# & \# & \# \\
0 & 0 & 0 & 0 & \# & \# & \# & \# & \# & \# & \# & \# \\
0 & 0 & 0 & 0 & 0 & 0 & \# & \# & \# & \# & \# & \# \\
0 & 0 & 0 & 0 & 0 & 0 & \# & \# & \# & \# & \# & \# \\
0 & 0 & 0 & 0 & 0 & 0 & \# & \# & \# & \# & \# & \# \\
0 & 0 & 0 & 0 & 0 & 0 & \# & \# & \# & \# & \# & \# \\
0 & 0 & 0 & 0 & 0 & 0 & \# & \# & \# & \# & \# & \#
\end{bmatrix}
$$

This matrix has 5 "zero-element" diagonals in the upper-right corner and 6 "zero-element" diagonals in the lower-left corner.

3. For two atmospheric layers ($L_1 = 2$) with two streams ($N_1 = 1$), and two ocean layers ($L_2 = 2$) with four streams ($N_2 = 2$), the coefficient matrix becomes

$$\begin{bmatrix}
\# & \# & 0 & 0 & 0 & 0 & 0 & 0 & 0 & 0 & 0 & 0 \\
\# & \# & \# & \# & 0 & 0 & 0 & 0 & 0 & 0 & 0 & 0 \\
\# & \# & \# & \# & 0 & 0 & 0 & 0 & 0 & 0 & 0 & 0 \\
0 & 0 & \# & \# & \# & \# & \# & \# & 0 & 0 & 0 & 0 \\
0 & 0 & \# & \# & \# & \# & \# & \# & 0 & 0 & 0 & 0 \\
0 & 0 & 0 & 0 & \# & \# & \# & \# & 0 & 0 & 0 & 0 \\
0 & 0 & 0 & 0 & \# & \# & \# & \# & \# & \# & \# & \# \\
0 & 0 & 0 & 0 & \# & \# & \# & \# & \# & \# & \# & \# \\
0 & 0 & 0 & 0 & \# & \# & \# & \# & \# & \# & \# & \# \\
0 & 0 & 0 & 0 & \# & \# & \# & \# & \# & \# & \# & \# \\
0 & 0 & 0 & 0 & 0 & 0 & 0 & 0 & \# & \# & \# & \# \\
0 & 0 & 0 & 0 & 0 & 0 & 0 & 0 & \# & \# & \# & \#
\end{bmatrix}$$

This matrix has six "zero-element" diagonals in the upper-right corner and six "zero-element" diagonals in the lower-left corner.

It is, of course, impractical to count these numbers every time. Fortunately, general relations exist between the number of "zero-element" diagonals and the numbers of streams and layers as follows:

$$n_0^u = (2L_1 - 1)N_1 + (2L_2 - 2)N_2, \qquad L_2 = 1 \tag{B.1a}$$

$$n_0^l = MIN[(2L_1 - 3)N_1 + 2L_2N_2,\ 2L_1N_1 + (2L_2 - 2)N_2],$$

$$L_2 = 1 \tag{B.1b}$$

$$n_0^u = n_0^l = 2N_1L_1 + (2L_2 - 3)N_2, \qquad L_2 > 1. \tag{B.1c}$$

Here n_0^u represents the number of "zero-element" diagonals in the upper-right corner and n_0^l represents the number of the "zero-element" diagonals in the lower-

left corner. The number of diagonals, containing one or more non-zero elements, above the main diagonal (n^u) and below the main diagonal (n^l) are

$$n^u = 2N_2 + N_1 - 1, \qquad L_2 = 1 \qquad \text{(B.2a)}$$

$$n^l = MAX[3N_1 - 1, 2N_2 - 1)], \qquad L_2 = 1 \qquad \text{(B.2b)}$$

$$n^u = n^l = 3N_2 - 1, \qquad L_2 > 1. \qquad \text{(B.2c)}$$

These formulas show that the size of the "zero-element" upper-right and lower-left triangles is proportional to the number of layers as well as the number of streams. If we use, say, 10 layers and 8 streams in the atmosphere $(L_1 = 10, N_1 = 4)$ and 10 layers and 12 streams in ocean $(L_2 = 10, N_2 = 6)$, the total number of "zero-element" diagonals in both the upper-right triangle and in the lower-left triangle will be $2 \times 182 = 364$, whereas the total number of diagonals with at least one non-zero element in each is only 35.

References

Assur, A., Composition of sea ice and its tensile strength, in "*Arctic Sea Ice*", National Acad. Sci., National Research Council Pub. 598, pp. 106-138, 1958.

Anderson, D. L., The physical constants of sea ice, *Research*, 13, 310-318, 1958.

Arrigo, K. R., J. N. Kremer and C. W. Sullivan, A simulated Antarctic fast ice ecosystem, *J. Geophys. Res.*, 98, 6929-6946, 1993.

Arrigo, K. R., C. W. Sullivan and J. N. Kremer, A bio-optical model of Antarctic sea ice, *J. Geophys. Res.*, 96, 10,581-10,592, 1991.

Barkstrom, B. R., Some effects of multiple scattering on the distribution of solar radiation in snow and ice, *J. Glaciol.*, 11, 357-368, 1972.

Barkstrom, B. R. and C. W. Querfeld, Concerning the effect of anisotropic scattering and finite depth on the distribution of solar radiation in snow, *J. Glaciol.*, 14, 107-124, 1975.

Bennett, T. J., A coupled atmosphere-sea ice model study of the role of sea ice in climatic predictability, *J. Atmos. Sci.*, 39, 1456-1465, 1982.

Berger, R. H., Snowpack optical properties in the infrared, *CRREL Rep. 79-11*, U. S. Army Cold Reg. Res. and Eng. Lab., Hanover, N. H., 1979.

Bohren, C. F. and B. R. Barkstrom, Theory of the optical properties of snow, *J. Geophys. Res.*, 79, 4527-4535, 1974.

Brandt, R. E., and S. G. Warren, Solar-heating rates and temperature profiles in Antarctic snow and ice, *J. Glaciol.*, 39, 99-110, 1993.

127

Buckley, R. G. and H. J. Trodahl, Scattering and absorption of visible light by sea ice, *Nature*, 326, 867-869, 1987.

Chandrasekhar, S., *Radiative Transfer*, Dover, New York, 1960.

Choudhury, B. J. and A. T. C. Chang, On the angular variation of solar reflectance of snow, *J. Geophys. Res.*, *86*, 456-472, 1981.

Coulson, K. L., *Solar and terrestrial radiation: methods and measurements*. Academic Press, 322 pp, 1975.

Cox, G. F. N. and W. F. Weeks, Equations for determining the gas and brine volumes in sea ice samples, *J. Glaciol.*, 29, 306-316, 1983.

Cox, G. F. N. and W. F. Weeks, Numerical simulations of the profile properties of underformed first-year sea ice during the growth season, *J. Geophys. Res.*, 93, 12,449-12,460, 1988.

Curry, J.A. and E. E. Ebert, Sensitivity of the thickness of arctic sea ice to the optical properties of clouds, *Annals of Glaciology*, 14, 43-46, 1990.

Curry, J.A., F.G. Meyer, L.F. Radke, C.A. Brock and E. E. Ebert, Occurrence and characteristics of lower tropospheric ice crystals in the arctic, *Internat. J. Climatol.*, 10, 10,749-764, 1990.

Dunkle, R. V. and J. T. Bevans, An approximate analysis of the solar reflectance and transmittance of a snow cover, *J. Meteorol.*, 13, 212-216, 1956.

Ebert, E. E. and J. A. Curry, An intermediate one-dimensional thermodynamical sea ice model for investigating ice-atmosphere interactions, *J. Geophys. Res.*, 98, 10,085-10,109, 1993.

Eicken, H., Salinity profiles of antarctic sea ice: field data and model results, *J. Geophys. Res.*, 97, 15,545-15,557, 1992.

Giddings, J. C. and E. R. LaChapelle, Diffusion theory applied to radiant energy distribution and albedo of snow, *J. Geophys. Res.*, *66*, 181-189, 1961.

Goody, R., and Y. L. Yung, *Atmospheric Radiation: Theoretical basis*, Oxford University

Press, Oxford, 1989.

Gordon, H.R., A bio-optical model describing the distribution of irradiance at the sea surface resulting from a point source embedded in the ocean, *Appl. Opt.*, *26*, 4133-4148, 1987.

Grenfell, T. C., and G. A. Maykut, The optical properties of ice and snow in the Arctic basin, *J. Glaciol.*, 18, 445-463, 1977.

Grenfell, T. C., The effects of ice thickness on the exchange of solar radiation over the polar oceans, *J. Glaciol.*, 22, 305-320, 1979.

Grenfell, T. C., D. K. Perovich and J. A. Ogren, Spectral albedos of an alpine snowpack, *Cold Reg. Sci. Technol.*, 4, 121-127, 1981.

Grenfell, T. C. and D. K. Perovich, Radiation absorption coefficients of polycrystalline ice from 400-1400nm, *J. Geophys. Res.*, 86, 7447-7450, 1981.

Grenfell, T. C., A theoretical model of the optical properties of sea ice in the visible and near infrared, *J. Geophys. Res.*, 88, 9723-9735, 1983.

Grenfell, T. C., A radiative transfer model for sea ice with vertical structure variations, *J. Geophys. Res.*, 96, 16991-17002, 1991.

Hecht, E., *Optics*, 2th edition, Addison-Wesley, Reading, Mass., 1990.

Herman, G. F. and J. Curry, Observational and theoretical studies of solar radiation in arctic stratus clouds, *J. Climate Appl. Meteorol.*, 23, 5-24, 1984.

Herman, G. F., and R. M. Goody, Formation and persistence of summertime Arctic stratus clouds, *J. Atmos. Sci.*, 33, 1537-1553, 1976.

Holm-Hansen, O., S. Z. El-Sayed, G. A. Franceschini, and R. L. Cuhel, Primary production and the factors controlling phytoplankton growth in the Southern Ocean, in *Adaptations within Antarctic ecosystems*, G. A. Llano, editor, p. 11-50, Smithsonia Institute, Washington, D. C., 1977.

Hu, Y. and K. Stamnes, An accurate parameterization of the radiative properties of water clouds suitable for use in climate models, *J. Climate*, 6, 728-742, 1993.

Hunt, G. E. and I. P. Grant, Discrete space theory of radiative transfer and its application to problems in planetary atmospheres, *J. Atmos. Sci.*, 26, 963-972, 1969.

Huschke, R. E., Arctic cloud statistics from "air-calibrated" surface weather observations. The Rand Corp., RM-6173-PR, 79 pp., 1969.

Jin, Z. and K. Stamnes, Radiative transfer in nonuniformly refracting layered media: atmosphere-ocean system, *Appl. Opt.*, 33, 431-442, 1994.

Joseph, J. H., W. J. Wiscombe and J. A. Weinman, The delta-Eddington approximation for radiative flux transfer, *J. Atm. Sci.*, *33*, 2452-2459, 1976.

Kattawar, G.W., and N.A. Adams, Stokes vector calculations of the submarine light field in an atmosphere-ocean with scattering according to a Rayleigh phase matrix: effect of interface refractive index on radiance and polarization, *Limnol. Oceanogr.*, 34, 1453-1472, 1989.

Kirk, J., "Monte Carlo procedure for simulating the penetration of light into natural waters," in Div. Plant Industry Tech. Paper 36, (CSIRO, Canberra, Australia, 1981), p.16.

Kuhn, M. and L. Siogas, Spectroscopic studies at McMurdo, South Pole and Siple stations during the austral summer 1977-78, *Antarct. J. U. S.*, 13, 178-179, 1978.

Langleben, M. P., On the factors affecting the rate of ablation of sea ice , *Can. J. Earth Sci.*, 3, 431-439, 1966.

Langleben, M. P., Albedo of melting sea ice in the southern Beaufort Sea, *J. Glaciol.*, 10, 101-104, 1971.

Liou, K.N., A numerical experiment on Chandrasekhar's discrete ordinate method for radiative transfer: Applications to cloudy and hazy atmospheres, *J. Atmos. Sci.*, 30, 1303-1326, 1973.

Liou, K.N., Applications of the discrete ordinate method for radiative transfer to inhomogeneous aerosol atmospheres, *J. Geophys. Res.*, *80*, 3434-3440, 1975.

Maykut, G. A. and N. Untersteiner, Some results from a time dependent thermodynamic

model of sea ice , *J. Geophys. Res.*, 76, 1550-1575, 1971.

Maykut, G. A. and T. C. Grenfell, The spectral distribution of light beneath first-year sea ice in the Arctic ocean, *Limnol. Oceanogr.*, 20, 554-563, 1975.

Maykut, G. A., Energy exchange over young sea ice in the central Arctic, J. Geophys. Res., 83, 3646-3658, 1978.

McClatchey R. A., R. W. Fenn, J. E. A. Selby, F. E. Volz, and J. S. Garing, Optical properties of the atmosphere, *AFCRL report AFCRL-72-0497*, (Air Force Cambridge Research Laboratories, Bedford, MA, 1972).

Mobley, C.D., A numerical model for the computation of radiance distributions in natural waters with wind-roughened surfaces, *Limnol. Oceanogr.*, 34, 1473-1483, 1989.

Mobley, C., B. Gentili, H. Gordon, Z. Jin, G. Kattawar, A. Morel, P. Reinersman, K. Stamnes and R. Stavn, Comparison of numerical models for computing underwater light fields, *Appl. Opt.*, *32*, 7484-7504, 1993.

Morel, A. and R. C. Smith, Terminology and units in optical oceanography, *Mar. Geod.* 5, 335-349, 1982.

Morel, A., and B. Gentili, Diffuse reflectance of oceanic waters: its dependence on sun angle as influenced by the molecular scattering contribution, *Appl. Opt.*, *30*, 4427-4438, 1991.

Nakajima, T., and M. Tanaka, Effect of wind-generated waves on the transfer of solar radiation in the atmosphere-ocean system, *J. Quant. Spectrosc. Transfer*, 29, 521-537, 1983.

Nelson, K. H. and T. G. Thompson, Deposition of salts from sea water by frigid concentration, *J. Marine Research*, 13, 166-182, 1954.

Nicolet, M., Solar spectral irradiances with their diversity between 120 and 900 nm, *Planet Space Sci. 37*, 1249-1289, 1989.

O'Brien, H. W. and R. H. Munis, Red and near-infrared spectral reflectance of snow, *CRREL Res. Rep.*, 332, U. S. Army Cold Reg. Res. and Eng. Lab., Hanover, N. H.,

1975.

Parkinson, C. L. and W. M. Washington, A large-scale numerical model of sea ice, *J. Geophys. Res.*, 84, 311-337, 1979.

Perovich, D. K. and T. C. Grenfell, A theoretical model of radiative transfer in young sea ice, *J. Glaciol.*, 28, 341-357, 1982.

Perovich, D. K. and G. A. Maykut, Solar heating of a stratified ocean in the presence of a static ice cover, *J. Geophys. Res.*, 95, 18,233-245, 1990.

Perovich, D. K., Theoretical estimates of light reflection and transmission by spatially complex and temporally varying sea ice covers, *J. Geophys. Res.*, 95, 9557-9567, 1990.

Perovich, D. K. and J. Gow, A statistical description of the microstructure of young sea ice, *J. Geophys. Res.*, 96, 16,943-16,953, 1991.

Plass, G., T. Humphreys and G. Kattawar, Ocean-atmosphere interface: its influence on radiation, *Appl. Opt.*, 20, 917-931, 1981.

Quakenbush, T., *Extinction of ultraviolet-A, visible and near infrared wavelength light in snow and antarctic sea ice*, Ph.D. Thesis, Univ. of Alaska, 1994.

Richardson, C. and E. F. Keller, The brine content of sea ice measured with a nuclear magnetic resonance spectrometer, *J. Glaciol.*, 6, 89-100, 1966.

Rothman, L. S., R. R. Gamache, A. Goldman, L. R. Brown, R. A. Toth, H. M. Pickett, R. L. Poynter, J.-M. Flaud, C. Camy-Peyret, A. Barbe, N. Husson, C. P. Rinsland, and M. A. H. Smith, The HITRAN database: 1986 edition, *Appl. Opt.*, 26, 4058-4097, 1987.

Schwerdtfeger, P. and G. E. Weller, Radiative heat transfer processes in snow and ice, in *Meteorological Studies at Plateau Station, Antarctica, Antarct. Res. Ser.*, Vol. 25, Ed. J. A. Businger, pp. 35-39, AGU, Washington, D. C., 1977.

Semtner, A. J., A model for the thermodynamic growth of sea ice in numerical investigations of climate. *J. Phys. Oceanogr.*, 6, 379-389, 1976.

Shaw, G. E. and K. Stamnes, Arctic haze: perturbation of the polar radiation budget,

Ann. N. Y. Acad. Sci., 338, 533-539, 1980.

Shaw, G. E., K. Stamnes and Y. X. Hu, Perturbation to the radiation field, *Meteorol. Atmos. Phys.*, 51, 227-235, 1993.

Shine, K. P. and R. G. Crane, The sensitivity of a one-dimensional thermodynamic sea ice model to changes in cloudiness, *J. Geophys. Res.*, 89, 10,615-10,622, 1984.

Shine, K. P. and A. Henderson-Sellers, The sensitivity of a thermodynamic sea ice model to changes in surface albedo parameterization, *J. Geophys. Res.*, 90, 2743-2250, 1985.

Slingo, A. and H. M. Schrecker, On the shortwave radiative properties of stratiform water clouds, *Quart. J. Roy. Meteor. Soc.*, 108, 427-426, 1982.

Slingo, A., A GCM parameterization for the shortwave radiative properties of water clouds, *J. Atmos. Sci.*, 46, 1419-1427, 1989.

Smith, R. C. and Baker, K. S., Optical properties of the clearest natural waters, Appl. Opt., 20, 177-184, 1981.

Soo Hoo, J. B., A. C. Palmisano, S. T. Kottmeier, M. P. Lizotte, S. L. Soo Hoo, and C. W. Sullivan, Spectral light absorption and quantum yield of photosynthesis in sea ice microalgae and bloom of *Phaeocystis Pouchetii* from McMurdo Sound, Antarctic, *Mar. Ecol. Prog. Ser.*, 39, 175-189, 1987.

Stamnes, K., The theory of multiple scattering of radiation in plane parallel atmospheres, *Rev. Geophys.*, 24, 299-310, 1986.

Stamnes, K. and P. Conklin, A new multi-layer discrete ordinate approach to radiative transfer in vertically inhomogeneous atmospheres, *J. Quant. Spectrosc. Radiat. Transfer*, 31, 273-282, 1984.

Stamnes, K., and R. A. Swanson, A new look at the discrete ordinate method for radiative transfer calculations in anisotropically scattering atmospheres, *J. Atmos. Sci.*, **38**, 387-399, 1981.

Stamnes, K., S. C. Tsay, W. J. Wiscombe and K. Jayaweera, Numerically stable algorithm for discrete-ordinate-method radiative transfer in multiple scattering and emit-

ting layered media. *Appl. Opt.*, 27, 2502-2509, 1988.

Stavn, R., R. Schiebe and C. Gallegos, Optical controls on the radiant energy dynamics of the air/water interface: the average cosine and the absorption coefficient," Ocean Optics VII, M. Blizard, Ed., Proc. SPIE 489, 62-67, 1984.

Tanaka, M. and T. Nakajima, Effects of oceanic turbidity and index of refraction of hydrosols on the flux of solar radiation in the atmosphere-ocean system, *J. Quant. Spectrosc. Radiat. Transfer* 18, 93-111, 1977.

Tsay S. C.,and K. Jayaweera, Physical Characteristics of Arctic stratus clouds. *J. Climate Appl. Meteor.*, 23, 584-596, 1984.

Tsay, S. C., K. Stamnes and K. Jayaweera, Radiative energy budget in the cloudy and hazy Arctic, *J. Atmos. Sci.*, 46, 1002-1018, 1989.

Untersteiner, N., On the mass and heat budget of arctic sea ice, *Arch. Meteorol. Geophys. Bioklimatol., Ser. A*, 12, 151-182, 1961.

Van Ypersele, J.-P., Modeling sea ice for climate studies, in *Climate-Ocean Interaction*, M. E. Schlesinger (Ed.), pp. 97-123, 1990.

Valero, F. P. J., T. P. Ackerman and W. J. Y. Gore, Radiative effects of the Arctic haze, *Geophys. Res. Lett.*, 10, 1184-1187, 1983.

Valero, F. P. J., T. P. Ackerman and W. J. Y. Gore, The absorption of solar radiation by the Arctic atmosphere during the haze season and its effects on the radiation balance, *Geophys. Res. Lett.*, 11, 465-468, 1984.

Valero, F. P. J., T. P. Ackerman, W. J. Y. Gore and M. L. Weil, Radiation studies in the Arctic, In *Aerosols and Their Climate Effects*, Eds., P. V. Hobbs and M. P. McCormick, A. Deepak Publishing, 271-276, 1988.

Warren S. G. and W. J. Wiscombe, A model for the spectral albedos of snow, 2, snow containing atmospheric aerosols, *J. Atmos. Sci.*, 37, 2734-2745, 1980.

Warren, S. G., Optical constants of ice from the ultraviolet to the microwave, *Appl. Opt.*, 23, 1206-1225, 1984.

Weller, G. E., Radiation diffusion in Antarctic ice media, *Nature*, 221, 355-356, 1969.

Wiscombe, W.J., The delta-M method: Rapid yet accurate radiative flux calculations for strongly asymmetric phase functions, *J. Atm. Sci.*, *34*, 1408-1422, 1977.

Wiscombe, W. J., Solar radiation calculations for Arctic summer stratus conditions, in 'Climate of the Arctic', (Eds. G. Weller and S. Bowling), 1975.

Wiscombe, W. J. and J. W. Evans, Exponential-sum fitting of radiative transmission functions, *J. Comp. Phys.*, 24, 416-444, 1977.

Wiscombe, W. J. and S. G. Warren, A model for the spectral albedos of snow, 1, Pure snow, *J. Atmos. Sci.*, 37, 2712-2733, 1980.

World Meteorological Organization, Global ozone research and monitoring project: Atmospheric ozone 1985, *World Meteorological Organization Rep. No. 16*, Volume 1, 1985.